Coexistence of Wireless Systems for Spectrum Sharing

Seungmo Kim

Dissertation submitted to the Faculty of the
Virginia Polytechnic Institute and State University
in partial fulfillment of the requirements for the degree of

Doctor of Philosophy
in
Electrical Engineering

Carl B. Dietrich, Chair
Alan T. Asbeck
Richard M. Buehrer
Jeffrey H. Reed
Yaling Yang

June 7, 2017
Blacksburg, Virginia

Keywords: Coexistence, Spectrum Sharing, mmW, 28 GHz, 70 GHz, 5G, Fixed Satellite Service, Fixed Service, 3.5 GHz, Pulsed Radar, OFDM, LTE, Wi-Fi, 5.9 GHz, DSRC, IEEE 802.11ac

Coexistence of Wireless Systems for Spectrum Sharing

Seungmo Kim

(ABSTRACT)

Sharing radio frequency (RF) spectrum among multiple wireless systems has emerged as a viable solution for alleviating the severe capacity crunch in next-generation wireless mobile networks such as 5th generation mobile networks (5G). Spectrum sharing can be achieved by enabling multiple wireless systems to coexist in a single spectrum band, via various means including signal processing, Medium Access Control (MAC), spatial multiple access techniques, etc. If successfully delivered, spectrum sharing therefore has the potential to significantly leverage spectral efficiency. In this dissertation, we discuss coexistence problems in spectrum bands that have recently been raising notable research interest, namely 27.5-28.35 GHz (28 GHz), 71-76 GHz (70 GHz), 5.85-5.925 GHz (5.9 GHz), and 3.55-3.7 GHz (3.5 GHz) bands. We furnish a solution for coexistence at each of the spectrum bands after identifying unique characteristics of the spectrum sharing problem in each band.

First, we characterize coexistence of 5G in the millimeter wave (mmW) bands–28 and 70 GHz. The incumbent systems with which 5G is to share the bands are Fixed Satellite Service and Fixed Service have been operating at 28 and 70 GHz, respectively. In the 28 GHz band, the uplink–Earth Station (ES) to space station (SS)–of Fixed Satellite Service (FSS) operates, wherein two directions of interference should be analyzed: ES-to-5G interference and 5G-to-SS interference. In 70 GHz band, the most popular application of FS is wireless backhaul (WB) that connects cell towers in cellular communications systems. Coexistence with 5G is more sophisticated in this band due to bi-directional operation of WB, contrast to only upward transmission of FSS at 28 GHz. For each of the bands, we (i) model interferences between 5G and the incumbent systems, and (ii) propose methods for mitigating inter-system interference for each of the spectrum sharing scenarios.

Second, coexistence of wireless communications system and pulsed radar at 3.5 GHz is discussed. In April 2015, the United States Federal Communications Commission (FCC) decided to open the band, which has mainly been utilized by military and meteorological radar, for shared usage with mobile broadband communications services. This dissertation answers the following questions regarding the coexisting systems:

1. How can a wireless communications system achieve acceptable performances under interference from coexisting radars?

2. How can a wireless communications system achieve maximum performances without causing harmful interference into coexisting radars?

An answer to the first question is provided by suggesting an Orthogonal Frequency Division

Multiplexing (OFDM) scheme that is robust against pulsed interference generated by coexisting radars. The second question is addressed by (i) proposing a scheme for suppressing interference into a radar and (ii) measuring the level of performance degradation that a communications system experiences with application of the proposed scheme.

Third, we study spectrum sharing between Dedicated Short-Range Communications (DSRC) and Wi-Fi in the 5.9 GHz band. The band has been reserved for intelligent transportation systems (ITS) since the FCC allocated the 75-MHz spectrum in October 1999. However, a bill called the Wi-Fi Innovation Act is introduced in the United States House of Representatives in February 2015, to urge the FCC to explore the feasibility of opening up spectrum for unlicensed Wi-Fi use. One serious concern is that DSRC is applied for safety-critical applications such as collision warning that are designed to improve road safety. This raises higher necessity of thorough characterization of DSRC functions for safety-critical applications in order to ensure that potential coexistence with Wi-Fi does not harm safety. To this end, a new performance metric that can better capture safety-critical operations of a DSRC network is proposed. Further, the new metric is then applied to characterize DSRC-Wi-Fi coexistence and to suggest proper operation parameters.

The results presented in each of the aforementioned parts show comprehensively that the coexistence methods help achieve spectrum sharing in each of the bands, and therefore potentially contribute to increase of bandwidth efficiency. As spectrum sharing is proposed and implemented in more bands in the future, the techniques proposed and studied in this dissertation will provide examples of ways to achieve a viable solution for the ever evolving capacity demands in the wireless communications landscape.

Coexistence of Wireless Systems for Spectrum Sharing

Seungmo Kim

(GENERAL AUDIENCE ABSTRACT)

Sharing a band of frequencies in the radio spectrum among multiple wireless systems has emerged as a viable solution for alleviating the severe capacity crunch in next-generation wireless mobile networks such as 5th generation mobile networks (5G). Spectrum sharing can be achieved by enabling multiple wireless systems to coexist in a single spectrum band. In this dissertation, we discuss the following coexistence problems in spectrum bands that have recently been raising notable research interest: 5G and Fixed Satellite Service (FSS) at 27.5-28.35 GHz (28 GHz); 5G and Fixed Service (FS) at 71-76 GHz (70 GHz); vehicular communications and Wi-Fi at 5.85-5.925 GHz (5.9 GHz); and mobile broadband communications and radar at 3.55-3.7 GHz (3.5 GHz). The results presented in each of the aforementioned parts show comprehensively that the coexistence methods help achieve spectrum sharing in each of the bands, and therefore contribute to achieve appreciable increase of bandwidth efficiency. The proposed techniques can contribute to making spectrum sharing a viable solution for the ever evolving capacity demands in the wireless communications landscape.

Dedication

To my family...
parents, sister, fiancee,
for their unconditional support and love.

Acknowledgments

I would like to begin this dissertation by thanking my dear family–my parents, sister Sohee Kim, and fiancee Jiwon Kim. Without their unconditional love and support, any of what I have got now would not have been possible. This achievement is as much their contribution as is mine for the very reason that they have always heartedly supported every decision I have made in my whole life. This bliss is for you all.

Throughout my Ph.D. study, I have had one great fortune to work with a great advisor, Dr. Carl Dietrich. I appreciate your advice not only in my Ph.D. study but in many other aspects of life. I am privileged to have been one of his first doctoral students and thus am grateful for the passionate guidance. The time spent with him has better prepared me for the new chapter of my life at Georgia Southern University after this graduation. I hope that I can pay back to him via further academic collaborations.

I also want to express a huge appreciation to the professors who served in my dissertation committee. I thank Dr. Jeff Reed for his interest in my work and for compassionate invitations to his Thanksgiving parties when we were the only souls left in town for the holidays every year. An as large appreciation must go to Dr. Michael Buehrer for his thorough review on my research. The advices and questions that he made in my Preliminary and Final Exams aided improve the quality and balance the perpective of this dissertation. To Dr. Yaling Yang, I appreciate her kind advice and conversations. Dr. Alan Asbeck well deserves a gratitude for bringing his solid understanding and creative perspectives into my research.

Dr. Jung-min Park helped me start my Ph.D. work. I appreciate his advice and support in first three years. Many parts of enthusiasm toward research have been learned from him.

I would like to thank Bob Lineberry and Jason Thweatt for the valuable pieces of advice that they have given to me. The time working with them as a graduate teaching assistant proved my eligibility in communicating with young students and brought me an opportunity to start my career as an educator, which I am grateful. I appreciate you two for such a great occasion and your favorable witness on what I have done with you in the reference letters to the university that hired me.

The most fruitful and rewarding time that I remember looking back the entire Ph.D. period is the one with Nokia Bell Labs in the summer of 2016. I wish please Eugene Visotsky

accepts my deepest appreciation for his passionate mentoring. To Prakash Moorut, I thank his endeavor of bringing out the results that we produced to the FCC and thus making them more visible. I thank Amitava Ghosh for granting me such a great opportunity to work with you smart (and handsome) researchers and keeping me motivated throughout. To Mark Cudak, I do not know if you would know that you were the person that I met on my first and last moments in the office. To Kamil Bechta, let me remember him for his hard work and co-authorship in our paper.

I can never doubt that the earlier learnings formed a basis for my starting a Ph.D. study. There were great educators who inspired me about what a researcher should do. Here I am honored to have a moment to thank them at Korea Advanced Institute of Science and Technology. I first thank Dr. Youngnam Han for his guidance and trust on me during my masters study. To Dr. Wan Choi, I hope you know that I still remember and appreciate the time working with you. I thank Dr. Joonhyuk Kang who joined the institution with myself and the friends in the same class for afterwards always giving us friendly advice that relieved our hard lives there. To Dr. Minho Kang, I can never forget your saying when I met you for asking a recommendatioion letter for the Ph.D. applications, "I might look like Bill Gates to you, but you look like an engineer working in a garage who has the great potential but has only not seen it yet." The great professors who woke me up, I thank all of you.

To you guys who started Blacksburg lives with me in 2012, Hyungil Kim, Gunji Jung, Dongseok Shin, Seungbeum Suh, Seunghwan Kim, Jaeeung Kim, and Heonwoo Lee (in the order of age–the very absolute Korean way), I love the moments we shared. To Kwanghae Noh, congratulations on your admission to a Ph.D. study, and I wish all my best luck. To Hyojoon Bae, I appreciate your guruing all the Fourier transform difficulties and spending great times with me. My loved friends, Yuhyun Song, Hyunchul Kim, Chungha Sung, Yoonchang Sung, Minjae Suh, Byungjun Kim, Minchul Sung, Hyunwoo Kang, Heonjoong Lee, Hyeon Lee, Gilsoo Lee, I heartily appreciate your friendship. (I hope all of you to forgive me for not being able to spend more lines; answer it when your phone rings). Thank you to my colleagues at Wireless@VT and Dr. Jung-Min Park's group. To Kevin McDermott and Jaber Kakar, the Durham clocks are still hanging for our ECE 4624 DSP memory. To Raghavendra Manjegowda, Pablo Quevedo, Dennis Obge, Ryan Keating, Kiran Venugopal, and Sijia Deng, I appreciate our fun times during the internships.

It has been quite a long journey with so many events to finally arrive at the point I had waited for–to leave the names that I would like to thank to. The most exciting part of the journey was to get to know so many people over the years. Yes, in this very town, Blacksburg, Virginia, you cannot even help becoming friends with whomever you meet on the street or on campus. Why? This town is too small for such many nice people to pass by without rubbing each other's shoulders. The time I spent here has been some of the best years of my life and I am thankful to the town and its occupants for making it a memorable. To every corner of Blacksburg and my friends who shared the beautiful pieces of memory, y'all will be missed so much.

Contents

List of Figures

List of Tables

Abbreviations

3GPP	The 3rd Generation Partnership Project
4G	4th generation mobile networks or 4th generation wireless systems
5G	5th generation mobile networks or 5th generation wireless systems
AP	Access Point
AWGN	Additive White Gaussian Noise
BPSK	Binary Phase Shift Keying
BSS	Broadcasting-satellite service
CBRS	Citizen's Broadband Radio Service
CCH	Control CHannel
CDF	Cumulative Distribution Function
CP	Cyclic Prefix
CQI	Channel Quality Indicator
CSMA/CA	Carrier Sense Multiple Access/Collision Avoidance
CW	Contention Window
dB	Decibel
DCF	Distributed Coordination Function
DFS	Dynamic Frequency Selection
DMRS	Demodulation Reference Signal
DLVY	A successful packet delivery
DSRC	Dedicated Short-Range Communications
EbNo	Energy per bit to noise power spectral density ratio
EIRP	Effective Isotropically Radiated Power
ES	Earth Station
ESC	Environmental Sensing Capability
EDCA	Enhanced Distributed Channel Access
EXP	EXPired packet transmission
F/B	Front-to-Back Ratio
FCC	Federal Communications Commission
FFT	Fast Fourier Transform
FS	Fixed Service
FSPL	Free Space Path Loss
FSS	Fixed Satellite Service

GHz	gigahertz
HCF	Hybrid Coordination Function
HN	Hidden Node collision
IBI	Inter-Broadcast Time
ICI	Inter-Carrier Interference
I/N, INR	Interference-to-Noise Ratio
IRT	Inter-Reception Time
ISC	Interference Self-Cancellation
ISD	Inter-Site Distance
ITS	Intelligent Transport System
ITU	International Telecommunication Union
LoS	Line of Sight
LTE	Long-Term Evolution
MAC	Medium Access Control
MCS	Modulation and Coding Scheme
MIMO	Multiple Input Multiple Output
MMAI	Mean Maximum Aggregate Interference
MSS	Mobile-satellite service
mmW	Millimeter Wave
NGMN	Next Generation Mobile Networks
NLoS	Non Line of Sight
NPPI	Normalized Priority-based Performance Indicator
NPRM	Notice of Proposed Rule Making
ns-2	Network Simulator 2
NTIA	National Telecommunications and Information Administration
OBU	On-Board Unit
OFDM	Orthogonal Frequency Division Multiplexing
PB	Pulse Blanking
PCF	Point Coordination Function
PDR	Packet Delivery Rate
PL	Path Loss
PN	Pseudo Noise
PPP	Poisson Point Process
PRT	Pulse Repetition Time
PSUN	Precoded SUbcarrier Nulling
QAM	Quadrature Amplitude Modulation
QPSK	Quadrature Phase Shift Keying
RF	Radio Frequency
ROC	Receiver Operating Characteristic
rpm	Rotations Per Minute
RSRP	Reference Signal Received Power
RSU	Roadside Unit

RtW	Radar-to-Wi-Fi interference
RX	Receiver
SAS	Spectrum Access System
SCH	Service CHannel
SINR	Signal-to-Noise-plus-Interference Ratio
SNR	Signal-to-Noise Ratio
SRS	Space Radiocommunication Stations
SS	Space Station
SYNC	SYNChronized transmission
TCP	Transmission Control Protocol
TDD	Time-Division Duplex
TX	Transmitter
UDP	User Datagram Protocol
UE	User Equipment
UMa	Urban Macro-Cell
UMi	Urban Micro-Cell
U-NII	Unlicensed National Information Infrastructure
V2I	Vehicle to Infrastructure
V2V	Vehicle to Vehicle
VANET	Vehicular Ad-hoc NETwork
WAVE	Wireless Access in Vehicular Environments
WB	Wireless Backhaul
WBSS	WAVE Basic Service Set
Wi-Fi	Wireless Fidelity
WLAN	Wireless Local Area Network
WRC	World Radiocommunication Conference
WtR	Wi-Fi-to-Radar interference

Chapter 1

Introduction

Spectrum is a scarce resource because demand has ever been growing. The reason for the growing demand for spectrum is growing demand for access to the Internet, which consume vastly more bandwidth.

The problem is that not much spectrum that is useful for communications is available recently. For example, now there is almost no spectrum available below 2 gigahertz (GHz) range [1]. But the more significant problem is that *much of the spectrum is not used efficiently*. For example, in the United States, the government possesses almost 60% of radio spectrum and possesses approximately 1500 megahertz (MHz) of the chunk of 300 MHz to 3 GHz spectrum that is regarded to be most useful for terrestrial wireless and mobile communications [1]. Much of that spectrum is lightly used or even not used.

In that regard, spectrum sharing has been attracting research interest. The key idea is to guarantee the current radio spectrum users–"primary" users–continue to have their legacy communications activities while allowing additional users–"secondary" users–to create other types of communications in the same band. Another advantage of developing spectrum sharing is that it can bring spectrum abundance without necessity of rearranging the current spectrum usages. For instance, a report released by the National Telecommunications and Information Administration (NTIA) in 2012 was cited by [1] to indicate that moving Federal users completely out of the 1755-1850 MHz band would cost approximately 18 billion dollars and take 10 years. Spectrum sharing is a more efficient way to maximize use of scarce resources, at less cost and delay than required to clear spectrum to make room for new users.

Spectrum sharing is an attractive solution for cellular operators in particular, in order to meet the growing bandwidth requirements and ease the spectrum crunch problem. There have been several coexistence problems recently that are invoked by either the Federal Communications Commission (FCC) or industry stakeholders such as wireless service operators or wireless product manufacturers. In this regard, this research studies three of the coexistence

problems that invoked recent research interest.

This dissertation provides three different scenarios of spectrum sharing. It provides different types of methodology according to characteristics of the wireless systems that participate in spectrum sharing. Spectrum sharing at 28 and 70 GHz and a part of that in the 3.5 GHz band are analyzed by means of stochastic geometry. The 3.5 GHz spectrum sharing takes another angle of view–a signal processing approach. For 5.9 GHz spectrum sharing, this dissertation presents MAC-layer suggestions.

1.1 5G-FSS and FS Coexistence at 28 and 70 GHz

Wireless data traffic will grow 10,000 fold within the next 20 years due to ultra-high resolution video streaming, cloud-based work, entertainment and increased use of a variety of wireless devices. These will include smartphones, tablets and other new devices, including machine type communications for the programmable world.

To meet demand, in addition to the more traditional cellular access bands below 6 GHz, 5th generation mobile networks (5G) are expected to exploit the large amount of spectrum between 6 GHz and 100 GHz. One or more new radio access technologies will be needed to address this regime of frequency bands due to different channel characteristics. Extending the air-interface of the 3rd Generation Partnership Project (3GPP) Long Term Evolution (LTE) to frequencies above 6 GHz may be considered, but it is likely that a simpler and more efficient air interface can be designed to address specific challenges.

The frequencies allocated or under discussion for additional bandwidth for cellular use have so far all been below 6 GHz, mostly due to the favorable wide area coverage properties of the lower frequencies. While more spectrum below 6 GHz is needed and there are promising techniques to increase the use of already allocated frequencies, there will be an increasing need to also unlock new spectrum bands. These bands, from 6 to 100 GHz will help to meet the high capacity and data rate requirements of the 5G era. The 6 to 100 GHz range can be broadly split in two parts, centimeter wave and millimeter wave (mmW), based on different radio propagation characteristics and the carrier bandwidth possible in the different frequency ranges.

At the other end of the spectrum range are the mmW frequencies which start at 30 GHz. At mmW, the radio propagation and radio frequency (RF) engineering is different from the sub-6 GHz spectrum range in some respects, such as higher diffraction and higher foliage and structure penetration losses. However, recent measurements have shown that mmW frequencies are also similar to those below 6 GHz in some other respects such as reflections and path loss exponents. There is still more experimentation required in these bands to understand the practical performance of the mmW bands but the reward will be achievable carrier bandwidths of for example 1-2 GHz. Even though there is a well defined border of 30 GHz between centimeter wave and mmW bands (1 cm wavelength), the radio propagation

changes more smoothly and there is no sharp transition point in the radio propagation characteristics.

In 2003, the Commission established service rules to promote non-Federal fixed development and use of spectrum in the 71-76 GHz, 81-86 GHz, and 92-95 GHz bands. Based on its determination that systems in these bands can readily be engineered to produce highly directional, very narrow-beam signals that can coexist in close vicinity without causing interference to one another, the Commission adopted a flexible and innovative regulatory framework for the bands. Specifically, the framework permits the issuance of an unlimited number of non-exclusive, nationwide licenses to non- Federal government entities for all of these bands. Under this licensing scheme, a license serves as a prerequisite for registering individual point-to-point links; licensees may operate a link only after the link is registered with a third-party database.

Based upon information available from the third-party database managers that are responsible for registering links in those bands, as of September 22, 2015 there were approximately 12,687 registered fixed links in the 71-76 GHz and 81-86 GHz bands.

The 71-74 GHz band segment also has co-primary allocations for Federal and non-Federal Fixed, Fixed Satellite Service (FSS), Mobile, and Mobile Satellite Service (MSS) operations. The 74-76 GHz band segment has co-primary allocations for Federal and non-Federal government Fixed, FSS (space-to-Earth), Mobile, and Space Radiocommunication Stations (SRS) operations. In addition, there are non-Federal allocations in that band segment for broadcasting and Broadcasting Satellite Service (BSS) operations.

Nokia identifies these bands as appropriate candidates for mobile use. Nokia believes these bands would be particularly appropriate because the wide amount of bandwidth available would support 10 Gbps peak rate with relatively simple equipment.

The Notice of Proposed Rulemaking (NPRM) [2] does not offer a specific proposal at this time to amend our rules relating to the 70 GHz and 80 GHz bands. Based on the current record, it is not clear how mobile units would be controlled to avoid interference to fixed links. None of the proponents of unlicensed use in these bands has made a detailed demonstration that unlicensed devices would be compatible with the fixed equipment being deployed in these bands.

Here are more details on the current regulatory endeavors with particular focus in the United States. In particular, the FCC Spectrum Frontiers initiative [2] and a 600 MHz Auction Plan [5], a response to a FCC NPRM [6], are good examples of the relevant regulatory efforts. According to [4], the cellular industry is indicating special interests in obtaining spectrum resource below 6 GHz. Approximately 2.27 GHz of potential new spectrum was identified by NTIA and the National Broadband Plan [3] where approximately 550 MHz is expected to be made available to the cellular industry in the next few years. The reference points that however, the enormous 94 GHz of spectrum from 6 to 100 GHz has been mostly neglected. The spectrum chunk should not be underestimated because even if only a third of that

spectrum were to be made available to the cellular industry, that would amount to around 31 GHz of new spectrum, which is significantly higher than the spectrum available below 6 GHz. By providing more spectra for future mmW cellular systems, the future capacity demands are expected to be met, while simultaneously incentivizing investments and technological developments that would ensure engineering competitiveness.

The reference [4] provides a very useful summary of the current focuses in the regulatory activities. This dissertation refers to the summary as below.

- **28 GHz band (27.5-29.5 GHz range):** The 27.5-28.35 GHz (850 MHz) and 29.1-29.25 GHz (150 MHz) portions of this band operate under FCC Part 101 rules for Fixed Microwave Services. These two sub-bands are called the Local Multipoint Distribution Service (LMDS) band in the USA. Other services in this band include Fixed Satellite Service (FSS), Geostationary Orbit (GSO) satellites, Non-Local Television Transmission Service (NON-LTTS), Mobile Satellite Service (MSS), and Non-Geostationary Orbit (NGSO) satellites.
- **38 GHz band (36-40 GHz):** The 38.6-40 GHz portion of this band operates under FCC Part 101 rules for Fixed Microwave Services and is used for fixed point-to-point microwave operations that provide backhaul links.
- **57-64 GHz band (V-band or 60 GHz band):** Currently this band is provisioned for unlicensed operation as per FCC Part 15.255 regulations. This band does have a large amount of oxygen absorption (see the next section) but it does not significantly hamper communications especially for small cells (e.g., distances of less than around 200 m). These frequencies may not be the first choice for a cellular mmW system since IEEE 802.11ad is designed to be used in this band and also due to the unlicensed nature of this band.
- **71-76 GHz and 81-86 GHz (E-band or the 70 GHz and 80 GHz bands, respectively):** This band operates under a lightly licensed paradigm as per FCC Part 101 and there are no limits in aggregating this band up to a total of 2×5 GHz. At this band the oxygen absorption is much less of an issue than at 60 GHz. Rain attenuation can be severe with longer distances but will not be a problem for small distances such as less than around 200 m.
- **92-95 GHz band (W-band or 90 GHz band):** This band is provisioned for unlicensed operation but only for indoor applications, as per FCC Part 15.257. Except for an excluded radio-astronomy band at 94-94.1 GHz, this band can be used for outdoor point-to-point licensed-light operation per FCC Part 101 regulations.

Based on the information listed above, the reference claims that the 28 GHz, 38 GHz, 71-76 GHz and 81-86 GHz bands are excellent candidates for deploying 5G communications

networks mainly due to its large abundance of bandwidth. Among them, significant 10 GHz is available in the 71-76 and 81-86 GHz bands with up to 5 GHz of contiguous bandwidth available making these bands appear more particularly attractive for a mmW system. Note, however, that any 5G system operating in the 71-76 GHz bands must coexist with fixed satellite service, automotive radar (77-81 GHz), and radio astronomy. This dissertation addresses coexistence problem for the 71-76 GHz band.

The reference [4] also states that although we used the US FCC regulations as examples, these bands are also available in many other countries. All of the bands have a mobile allocation in the ITU-R Radio Regulations. Note also that other countries have similar spectrum allocations in the 28 and 38 GHz bands, and the 60 GHz band is a global unlicensed band with different subsets of 57-66 GHz available in Europe, USA, Canada, Japan, Korea, Australia, and China. The 70 GHz and 80 GHz E-bands are available in Europe under a license-light regime similar to the USA.

1.2 Communications-Radar Coexistence at 3.5 GHz

In October 2010, an NTIA's Fast Track Report [7] identified the 3.5 GHz Band (3.550-3.700 GHz) as potentially suitable for commercial broadband use. The 3.5 GHz Band is one of the candidate bands identified by the NTIA in response to the President's initiative to identify 500 megahertz of spectrum for commercial wireless broadband, which was outlined in a June 2010 Presidential Memorandum. The NTIA believes that the 3.5 GHz Band is well suited to exploring the next generation of shared spectrum technologies and to drive greater productivity and efficiency in spectrum use.

The FCC initiated a rulemaking proceeding to address sharing issues associated with the establishment of a new Citizen's Broadband Radio Service (CBRS) in the 3.5 GHz Band.

In the Fast Track Report, the NTIA concluded that geographic separation and frequency offsets could be used to minimize interference between a deployment of commercial high-power macro-cell networks and federal radar systems that operate or are planned to operate in and adjacent to the 3.5 GHz Band. Based on the analysis in the Fast Track Report, the NTIA recommended large exclusion zones along the coastlines (east, west, and gulf) and exclusion zones around selected ground-based radar sites. In the 3.5 GHz Further Notice of Proposed Rulemaking, the FCC said it would work with the NTIA to reassess the exclusion zone distances using lower-powered small cell technology. The NTIA engineers spearheaded groundbreaking analysis and modeling techniques and collaborated closely with Department of Defense and FCC staff. This team effort resulted in significantly reduced exclusion zones, maximizing the commercial market potential for new broadband services, while still protecting essential incumbent federal operations and satellite services.

On April 17, 2015, the FCC voted to approve rules for the new CBRS service, incorporating smaller exclusion zones and setting the stage for commercial deployment in the 3.5 GHz

band.

1.3 DSRC-Wi-Fi Coexistence at 5.9 GHz

Vehicular ad-hoc networks (VANET) can save lives by warning drivers of impending dangerous conditions or events in time to take preventive actions [8]. VANETs allow both vehicle-to-vehicle (V2V) communications and vehicle-to-infrastructure (V2I) communications. In a DSRC network, each vehicle is equipped with an on-board unit (OBU), and infrastructures are equipped with roadside units (RSUs). A vehicle can communicate with other vehicles or infrastructures via OBUs and RSUs.

In 1999, the FCC allocated 75 megahertz of spectrum for intelligent transportation services to improve highway safety and efficiency as part of the U.S. Department of Transportation's "Intelligent Transportation Systems" (ITS) national program. In a Report and Order [9], the FCC decided to use the 5.850-5.925 GHz band for Dedicated Short Range Communications (DSRC) uses, such as traffic light control, traffic monitoring, travelers' alerts, automatic toll collection, traffic congestion detection, emergency vehicle signal preemption of traffic lights, and electronic inspection of moving trucks through data transmissions with roadside inspection facilities.

DSRC systems are designed to provide a short range, wireless link to transfer information between vehicles and roadside systems. These links will be essential to many ITS services that are expected to improve traveler safety, decrease traffic congestion, and facilitate the reduction of air pollution and conservation of fossil fuels. The FCC said providing additional spectrum for ITS services would further the goals of Congress, the Department of Transportation and the ITS industry to improve the efficiency of the U.S. transportation infrastructure and to facilitate the growth of the ITS industry.

However, the FCC has recently been considering to allow Unlicensed National Information Infrastructure (U-NII) devices, in particular IEEE 802.11ac devices, to operate in the U-NII 3 and U-NII 4 bands, 5,350-5,470 MHz and 5,950-5,925 MHz, respectively, [9], the latter of which is the DSRC band. Therefore, in this coexistence problem, DSRC users become primary users while 802.11ac users become unlicensed secondary users. The main objective of this plan is to guarantee 802.11ac more spectrum, in order to provide sufficient spectrum for the system to support its very high data rate [10]. This movement is recently being reinforced by reintroduction of S.424 the Wi-Fi Innovation Act in the U.S. Congress led by several bipartisan legislators including Senators Booker (D-NJ) and Rubio (R-FL). The current status is that the FCC accepted the submission of testing equipments until July 30, 2016 and commits to complete testing by Jan. 15, 2017.

1.4 Main Contributions

This dissertation presents different analysis methods for each of the spectrum sharing scenarios. Contributions for each scenario that this dissertation provides are described as below.

1.4.1 5G-FSS and FS Coexistence at 28 and 70 GHz

This spectrum sharing study is given in Chapter 2. With respect to methodology, this study adopts a geometric approach to characterize coexistence of 5G and the incumbents at 28 and 70 GHz.

A promising way of realizing 5G wireless systems is to operate 5G deployments in higher frequency bands, specifically in the millimeter wave spectrum (30-300 GHz), due to the multitude of underutilized spectrum bands available at those frequencies. Access to such spectrum bands will enable future 5G wireless systems to meet the 5G requirements of peak rate greater than 10 Gbps, and cell edge rate of up to 1 Gbps. However, the emerging 5G systems will need to coexist with a number of incumbent systems in these bands. Chapter 2 provides an extensive coexistence study of two critical mmW bands, 27.5-28.35 GHz (28 GHz) and 71-76 GHz (70 GHz) bands, where Fixed Satellite Service (FSS) and Fixed Service (FS) such as Wireless Backhaul (WB) are the predominant incumbent users. In the 28 GHz study, we show that interference from 5G into the FSS Space Stations (SSs) can be kept below the FSS interference protection criterion. We also characterize the minimum separation distance between the FSS Earth Stations (ESs) and 5G in order to protect the 5G system from interference due to the ESs transmissions. In the 70 GHz study, we show that the 5G-to-FS interference could be a potential issue in certain scenarios, but we introduce techniques to significantly suppress this interference, while maintaining acceptable performance of the 5G systems.

1.4.2 Communications-Radar Coexistence at 3.5 GHz

This study corresponds to Chapters 3 and 4. The two chapters represent different methodologies toward radar-communications coexistence problem. Chapter 3 provides a geometric approach to characterize coexistence of Wi-Fi and radar at 3.5 GHz. Chapter 4 discusses a novel signal processing method that makes an OFDM-based communications system robust against pulsed interference from a radar.

Chapter 3 investigates coexistence between radar and outdoor Wireless Fidelity (Wi-Fi), which needs thorough study since the IEEE 802.11 Working Group (WG) opposed the latest rules in 3550-3700 MHz (the 3.5 GHz band) that require "exclusion zones." This chapter proposes a method that suppresses Wi-Fi-to-radar (WtR) interference, in which a Wi-Fi transmitter (TX) is selected to avoid beam angles toward the victim radar. It is distinguished

from prior schemes since it ensures that the Wi-Fi remains operable while suppressing the WtR interference.

Chapter 4 proposes Precoded SUbcarrier Nulling (PSUN), an orthogonal frequency-division multiplexing (OFDM) transmission strategy for a wireless communications system that needs to coexist with federal military radars generating pulsed signals in the 3.5 GHz Band. This chapter considers existence of Environmental Sensing Capability (ESC), a sensing functionality of the 3.5 GHz Band coexistence architecture, which is one of the latest suggestions among stakeholders discussing the 3.5 GHz Band. Hence, the chapter considers impacts of imperfect sensing for a precise analysis. An imperfect sensing occurs due to either a sensing error by an ESC or a parameter change by a radar. The chapter provides a framework that analyzes performance of an OFDM system applying PSUN with imperfect sensing. Our results show that PSUN is still effective in suppressing inter-carrier interference (ICI) caused by radar interference even with imperfect pulse prediction. As an example application, PSUN enables LTE downlink to support various use cases of 5G in the 3.5 GHz Band.

1.4.3 DSRC-Wi-Fi Coexistence at 5.9 GHz

This spectrum sharing scenario is discussed in Chapter 5. We take a MAC-layer point of view to characterize in consideration of this particular coexistence problem since the performances of the two coexisting systems are dominated by a certain set of MAC parameters.

Chapter 5 discusses co-channel coexistence between Dedicated Short-Range Communications (DSRC) and Wi-Fi, which needs thorough study. The reason is that although the 5.850-5.925 GHz (5.9 GHz) band has been reserved for DSRC so far, the U.S. government is moving swiftly on opening the band to be shared with Wi-Fi. However, most prior work lacks sufficient scientific rigor by relying on performance metrics such as packet delivery rate (PDR) and packet delay that cannot accurately measure performance of a vehicular network that primarily uses broadcast in dissemination of packets. Precise analysis of such broadcast operation is essential for rigorous investigation of DSRC-Wi-Fi coexistence because most safety-critical applications of DSRC operate based on broadcast. This chapter proposes a new performance metric that can more accurately characterize the performance of a broadcast-based DSRC network. Based on the new metric, it characterizes coexistence of DSRC with IEEE 802.11ac-based Wi-Fi and suggests selection of key Medium Access Control (MAC) parameters for DSRC: inter-broadcast interval (IBI) and contention window (CW).

1.5 List of Relevant Publications

The work presented in this dissertation is based on the following publications in peer-reviewed journals and conference proceedings, and US patents.

Journals

1. **S. Kim**, C. Dietrich, "Coexistence of outdoor Wi-Fi and radar at 3.5 GHz," *IEEE Wireless Commun. Lett.*, accepted
2. **S. Kim**, E. Visotsky, P. Moorut, A. Ghosh, C. Dietrich, "Coexistence of 5G with the incumbents in the 28 and 70 GHz bands," *IEEE J. Sel. Areas Commun.*, vol. 35, iss. 6, Jun. 2017.
3. **S. Kim**, J. Choi, C. Dietrich, "PSUN: an OFDM - pulsed radar coexistence technique with application to 3.5 GHz LTE," *Hindawi Mobile Information Systems Journal*, Jul., 2016.
4. **S. Kim**, C. Dietrich, "A geometric analysis method for evaluation of coexistence between DSRC and Wi-Fi at 5.9 GHz," submitted to *IEEE Trans. Veh. Technol.*
5. **S. Kim**, C. Dietrich, "Spectrum sharing between DSRC and IEEE 802.11ac at 5.9 GHz," to be submitted to *IEEE Trans. Wireless Commun.*

Conferences

1. **S. Kim**, J. Park, K. Bian, "PSUN: an OFDM transmission strategy for coexistence with pulsed radar," in *Proc. IEEE ICNC*, 2015.
2. **S. Kim**, J. Choi, C. Dietrich, "Coexistence between OFDM and pulsed radars in the 3.5 GHz band with imperfect sensing," in *Proc. IEEE WCNC*, 2016.

Patents

1. USPTO 62402690, "A mitigation technique for 5G UE-into-mmW backhaul interference," filed Oct. 2016.
2. USPTO 62412466, "Beam management for interference mitigation for wireless networks," filed Oct. 2016.

1.6 Organization of Dissertation

This dissertation provides in-depth analyses and results for each of the aformentioned coexistence scenarios. The rest of the dissertation is organized as follows:

- In Chapter 2, we present a geometric approach for analysis of coexistence of 5G with the incumbent systems at 28 and 70 GHz: FSS and FS, respectively. The analysis includes (i) characterization of coexistence between 5G and incumbent, and (ii) proposition of interference mitigation techniques.

- In Chapter 3, we discuss a geometric approach for coexistence of Wi-Fi with radar at 3.5 GHz. This study is extended from the one provided in Chapter 3 in the following two aspects.

  First, characterization of Wi-Fi is different. Wi-Fi adopts carrier-sense multiple access (CSMA) wherein either an access point (AP) or a normal station (STA) can be elected as a T for a time slot, which complicates characterization compared to a system where transmissions of a base station (BS) and a mobile station are duplexed.

  Second, characterization of incumbent is unique. Radars operating in this spectrum band are mainly pulsed radars that usually rotates a very sharp beam periodically, which increases complexity of analysis. In addition to the beam rotation, this chapter takes into account sidelobe gains in both cases when a radar becomes an interferer and a victim.

- In Chapter 4, we take a different method, a PHY-layer approach, for analysis of coexistence of an OFDM-based communications system with radar at 3.5 GHz. We suggest an OFDM system that is composed of a pair of TX adopting Precoded Subcarrier Nulling (PSUN) and RX with interference self-cancellation (ISC). Our results show that this proposed scheme makes an OFDM system robust against pulse interference from a coexisting radar, which is enough for supporting several applications of 5G.

- In Chapter 5, we propose a performance evaluation scheme that potentially contributes to enhancement of MAC-layer approaches for coexistence of DSRC and Wi-Fi at 5.9 GHz. Most typical performance metrics cannot accurately capture the performance of a broadcast-based DSRC network, since they measure based on a binary success/failure decision of a packet broadcast. We take a "softer" approach wherein the result of a packet broadcast is "partially" evaluated; even a corrupted packet can still be received by some RX vehicles depending on geometry. Based on the new method, we evaluate the performance of a DSRC network under coexistence with Wi-Fi.

- In Chapter 6, we conclude the dissertation.

Chapter 2

5G-FSS and FS Coexistence at 28 and 70 GHz

This chapter analyzes coexistence of 5th generation mobile networks (5G) with the incumbent systems in two millimeter wave (mmW) spectrum bands: 28 and 70 GHz bands. The incumbent systems in the bands are the uplink (ES to SS) of FS at 28 GHz and both the downlink and uplink of FSS at 70 GHz.

Operation of 5G in higher frequency bands has sheer benefits, especially in mmW spectrum (30-300 GHz) in order to obtain large bandwidth, thus higher data rates. However, in many of the mmW bands, there already have been the "incumbent" systems. Therefore, spectrum sharing problems must be addressed for successful service of 5G in the mmW bands. This chapter provides an extensive study in two spectrum bands that have recently been invoking extremely much of research interest recently: the 27.5-28.35 GHz (28 GHz) and 71-76 GHz (70 GHz) bands, where the FS has been the primary system. The chapter provides an analysis framework that can be generally used in future coexistence problems between the 5G and the FS in mmW bands. In the 28 GHz study, we show that interference from the 5G into the FSS SSs can be kept below the FSS interference protection criterion while guaranteeing several thousands of 5G cells to operate. Also, we calculated separation distances to address interference from existing transmit ESs into the 5G. In the 70 GHz study, we show that 5G-to-WB interference is significant. Motivated from the 70 GHz results, we proposed interference mitigation techniques between the 5G and the FS operating on the ground. Our results show that the proposed techniques significantly suppress 5G-to-FS interference, while keeping performance of the 5G operable.

2.1 Related Work

Recently there has been a growing interest in cellular systems operating in mmW bands. There are two main advantages to be gained in the mmW bands: (i) the availability of large amount of under-utilized spectrum [11] and (ii) the capability to integrate a very large numbers of antennas into future 5G User Equipments (UEs) and Access Points (APs) due to very small mmW wavelengths [18]. Thus, disadvantages in propagation due to high frequency in mmW bands can be mitigated by using large antenna arrays at both transmitter and receiver ends of 5G wireless links, creating a massive Multiple Input-Multiple Output (MIMO) communication system. The ideas of deploying massive MIMO arrays in mmW bands have been well-covered in recent work such as [12][13].

There is high international interest (including USA, Japan and South Korea) in making the 27.5-28.35 GHz (28 GHz) band available for mobile use [15]. In addition, the 71-76 GHz (70 GHz) band was identified at the International Telecommunication Union (ITU)'s World Radiocommunication Conference (WRC) 2015 [16] as a possible band for future 5G wireless system deployments. In the 28 GHz band, Fixed Satellite Service (FSS) uplink–i.e., the communication links from Earth Stations (ESs) to Space Stations (SSs)–is in wide use, whereas in the 70 GHz band, the Fixed Service (FS) Wireless Backhaul (WB) for other cellular systems–e.g., the 4th generation (4G)–is the predominant incumbent.

2.1.1 Coexistence Models

There is related work that discusses various models of coexistence. In [19], for coexistence between MIMO radar and Long-Term Evolution (LTE) systems, projection of the radar waveform onto the null space of the interference channel is proposed, using a concept originally introduced in [20]. In [21], the aggregate interference from multiple secondary users to a single primary user is modeled by a probability distribution. In [22], an aggregate interference from heterogeneous sources is modeled. In [23], a system-level analysis of the interference from the shipborne radar into LTE systems is discussed. In [24], experimental results of interference from the military radar into the Time-Division (TD) LTE are presented. In [25], coexistence of the meteorological radar and the Wireless Local Access Network (WLAN) is discussed. In [26], interference between radar and WLAN systems is studied.

Additional prior art in modeling interference among between different wireless systems is provided in [27]. The reference provides a very informative literature survey on heterogeneous networking, which also helps the readers of this dissertation understand the state-of-the-art in inter-system interference modeling. The following two paragraphs refer to the reference to provide the recent interference models.

Due to the limited coverage area that a mmW communications system provides, it likely

needs to coexist with other systems of other bands, such as LTE and Wi-Fi. This makes mmW networks inherently heterogeneous in many practical scenarios [28], [29], [31]-[34]. More specifically, short-range systems–e.g., pico-cells–operating in a mmW band will likely coexist with macro-cells and micro-cells in other bands [30]. This will entail that cells in the microwave bands have larger coverage areas, while smaller cells such as the ones in the mmW band have higher capacity. In [35], a novel mmW heterogeneous network (HetNet) system is introduced, which exploits the large bandwidth and unpropitious propagation characteristics in mmW bands that can reduce the impact of interference in HetNets. Therefore, in HetNets, coordination between different types of networks becomes a key to address the inherent problems such as mobility management, vertical handover, mobile data offloading from macro-cells to micro-cells [36], inter-cell interference management, etc. In [37], a HetNet structure between a mmW and a 4G system with TDMA-based MAC scheme is suggested as a candidate for 5G cellular networks, where the control functions are operated in the 4G system. The high capacity of mmW communications can share the traffic from the macro-cells and provide better services for traffic with high throughput requirements. In comparison, handovers between BSs of macro-cells and APs in the mmW band are able to address problems such as blockage, mobility management, load balancing, etc.

For mmW networks, there are also studies discussing distribution of the control messages for channel access and coordination both on mmW and lower spectrum bands [38]-[40]. Thus, a part of important control signals such as synchronization or channel access requests can be transmitted in the lower bands adopting their typical PHY and MAC manners. Therefore, the integration between different networks becomes a significant factor that determines the system performance [39]. It incurs a tradeoff where tight integration is beneficial to achieve better performance while loose integration has low complexity. In other words, the tradeoff occurs between complexity and performance in heterogeneous networking. Considering the tradeoff, a software defined architecture with flexible programmability, such as OpenRadio [40], can be regarded as a promising candidate to achieve tight integration between networks while achieving the required complexity in a more flexible manner.

2.1.2 Interference Mitigation Schemes

There is also a body of prior work that discusses the techniques of interference reduction. In [41], regulatory policies that improve sharing conditions/opportunities in areas with large data traffic demand are proposed. In [42], a geometric technique for suppressing interference from Wi-Fi to radar systems is proposed. In [43], a precoding technique that makes Orthogonal Frequency-Division Multiplexing (OFDM) transmissions robust to radar interference is proposed. In [44], an interference mitigation technique for coexistence of LTE with radar is proposed.

To the best of our knowledge, very little work has been performed in the area of spectrum sharing in mmW bands so far. The most relevant research can be found in [45], where

co-channel interference between 5G small cells and FSS at 28 GHz is studied. There is literature that discusses measurement results in mmW bands. In [46], the authors claim that their results measured at 73 GHz support the use of directional steerable antennas at mmW bands to achieve comparable channel statistics to current cellular systems. In [18], results of measurement at 28 and 73 GHz bands are discussed to derive detailed spatial statistical models of the channels. There are several studies on interference mitigation techniques for 5G. In [47], a framework of spectrum sharing is proposed for a heterogeneous 5G network based on existence of geolocation database. In [48], an inter-cell interference mitigation technique is proposed for 5G small-cell networks. In [49], an interference mitigation framework is proposed for 5G heterogeneous networks where a massive MIMO macro-cell base station is overlaid with self-backhauled small cells. In [50], an interference mitigation technique is proposed for 5G sharing spectrum at 60 GHz.

2.2 Main Contributions

In this chapter, we discuss coexistence between 5G and two incumbents at 28 GHz and 70 GHz, the FSS and FS systems, respectively. Showing that 5G can coexist with these incumbent systems is critical to the introduction of 5G in mmW bands. Our work is more extensive than [45] because we (i) discuss more detailed methods of enabling coexistence between 5G and FSS at 28 GHz, and (ii) additionally study coexistence of 5G at 70 GHz. Moreover, motivated by our results from the study of 70 GHz, we propose techniques that mitigate interference from 5G APs and UEs to the incumbent system. While the prior schemes [47]-[49] focus on inter-cell interference in 5G systems, we address coexistence of 5G with incumbent systems, which is more critical in deployment of 5G in mmW bands. Further, the interference mitigation techniques proposed in this chapter are well distinguished from the prior work [41]-[44] in the following aspects. Firstly, we suggest detailed procedures that make the proposed techniques standalone, and thus they do not require assistance from infrastructure such as Spectrum Access System (SAS) that is adopted as a solution for coexistence at 3.5 GHz [14]. Secondly, our proposed methods are straightforward to implement under practical deployment constraints, as they solely rely on the native beam management protocols defined as part of the 5G air interface.

More specifically, the contributions that this chapter describes are as follows:

- We provide detailed analysis and supporting simulation results of the co-channel coexistence between 5G and uplink FSS systems in the 28 GHz band. With respect to the 5G system modeling, we concentrate on APs, as interference generated and observed at the APs is much more significant than that at the UEs. Hence, we analyze the AP-to-SS and ES-to-AP interference. Based on our results, we conclude that (i) potentially on the order of hundreds to thousands of APs can simultaneously transmit in a given 5G service area without harming an SS receiver and (ii) a separation distance on the

order of a few kilometers is required between an ES and the 5G system for acceptable operation of 5G.

We also provide an initial set of results on the UE-to-SS interference assessment. In general, characterization of the UE-to-SS interference is heavily dependent on the deployment scenario and such system parameters as the percentage of UEs indoors or below clutter, as well as the particulars of the UE antenna array design. Hence, a detailed study of the UE-to-SS interference is outside the scope of this paper. Nevertheless, we provide a number of preliminary results on UE-to-SS interference, indicating that under reasonable UE deployment assumptions, the number of active UEs supported can far exceed the number of active APs in a 5G service area.

- We analyze the co-channel coexistence between 5G and FS at 70 GHz. We assume the FS system to be a point-to-point WB for another cellular system such as 4G. Unlike the coexistence at 28 GHz, all of the four directions of interference are possible in this band: AP to FS, FS to AP, UE to FS, and FS to UE. It is because (i) both directions of an FS link operate at 70 GHz, and (ii) UE has higher probabilities of Line-of-Sight (LoS) in a 5G-FS coexistence topology since the beam of an FS's antenna is placed terrestrially and pointed closer toward the ground. We find that compared to the FS-to-5G interference, the one from 5G to FS (both AP to FS and UE to FS) is more significant since an interference is aggregated among multiple cells.

- Motivated from the finding, we propose techniques that mitigate AP-to-FS and UE-to-FS interference. The main idea for mitigation of the AP-to-FS interference is to establish exclusion zones at each region of AP, in order to ensure that the transmit beam gain toward the FS is attenuated sufficiently. Mitigation of the UE-to-FS interference is to force a UE to generate an uplink beam that is away enough from the direction toward FS. The proposed techniques can be applied to other coexistence situations, as long as the incumbent system operates terrestrially.

2.3 Coexistence of 5G with Fixed Satellite Service at 28 GHz

At 28 GHz, the FSS operates in the uplink only (from ES to SS). Therefore, for coexistence with 5G, the possible scenarios of interference are 5G to SS and ES to 5G. Note that we consider the case of co-channel interference only.

In general, we expect APs to be the dominant source of interference from 5G. The reason is that in comparison to AP-to-SS interference, the UE-to-SS interference has much smaller impact since the Effective Isotropically Radiated Power (EIRP) of a UE is likely far lower than that of an AP. In addition, a UE is far more likely than an AP not to have a line-of-sight (LoS) propagation path toward an SS, which further reduces the potential for the UE-to-SS

Table 2.1: Parameters for 5G

Parameter	**AP**	**UE**
Carrier frequency	28 GHz	
System layout	UMi [62]	
Inter-site distance (ISD)	200 m	
Cell density	29 cells/km^2	
Cell sectorization	3 sectors/site	
Duplexing	Time-division duplexing (TDD)	
Transmission scheme	Singler-user (SU)-MIMO	
Bandwidth	850 MHz	
Temperature	290 K	
Max antenna gain	5 dBi per element	
Max antenna gain	5 dBi per element	
Number of antennas ($\lambda/2$ array)	8×8 and 16×16	4×4
Noise figure	7 dB	9 dB
Antenna height	10 m	1.5 m

interference. These observations are confirmed by our results on the UE-to-SS interference, indicating that the number of active UEs permitted in a 5G service area far exceeds that of active APs.

For the FSS-into-5G direction, only ES-to-AP interference is considered as interference observed at the APs is expected to be the bottleneck for 5G system deployments. The UEs likely to have smaller antenna gains and experience much higher propagation losses from the ES transmitters than APs. Hence, the directions of interference that we consider in this study are AP-to-SS, UE-to-SS and ES-to-AP.

Finally, we note that the distribution of UEs in the system plays an important role in both directions of the interference. The reason is that the position of a UE determines the UEs and the serving AP's beamforming directions, which in turn affects both the AP-to-SS, UE-to-SS and ES-to-AP interference. As in Table 2.1, the cell site of an AP is divided into three sectors, each of which spans 120 degrees (°). The distribution of UEs follows Poisson Point Process (PPP) [51] in a sector region.

Table 2.2: Parameters for FSS SS

Parameter	**Class 1**	**Class 2**	**Class 3**
Elevation angle (degrees)	15-55	15-55	5-50
Orbit distance (km)	36,000	36,000	9,000
Max antenna gain (dBi)	58	58	27
Temperature (K)	1000	650	570
Thermal noise (dBm/Hz)	-168.6	-170.5	-171.0
Path loss models between 5G and FSS SS (dB)	LoS: FSPL + 4 NLoS: FSPL + 24		
Interference protection criterion (I/N, dB)	$TH_{fss} = \{-12.2, -6, 0\}$		

2.3.1 Interference from 5G AP and UE to FSS SS

System Model

Tables 2.1 and 2.2 provide parameters for the 5G AP/UE and FSS SS, respectively. For the SS, the interference protection criterion is defined as the threshold of interference-to-noise ratio (I/N), which is denoted by TH_{fss}. Regarding the path loss between an AP/UE and an SS, various combinations of LoS and Non-Line-of-Sight (NLoS) channel conditions are considered. Note that a large percentage of LoS sites appears to be unrealistic given real-world vegetation/foliage losses and practical deployment cases of 5G. Moreover, we note that LoS channel conditions will occur with very low probabilities at 28 GHz, where propagation of a microwave signal is adversely affected not only by blockage due to buildings and other structures but also by vegetation. Therefore, only realistic subsets of LoS/NLoS combinations are reported in our final results given in Tables 2.3 and 2.4.

The path loss models are elaborated as follows. In LoS conditions, we assume a free space path loss (FSPL) model [52] plus additional atmospheric and polarization losses of 4 dB In the NLoS channel conditions, an FSPL model is again used, with additional 20 dB of clutter loss in addition to the 4 dB of atmospheric and polarization losses [54]. Thus, the total additional loss assumed in the NLoS model is 24 dB. Recall that *clutter loss* is the loss due to various conditions on the terrain (such as buildings) over a wide area, and hence it also accounts for the *diffraction loss* [53], which is the loss due to propagation bending around an object such as a building or a wall. Note that our assumption of a 20 dB of clutter loss is worst case with respect to interference modeling, as diffraction losses can be significantly higher depending on the ray angles of incidence and departure toward the satellite. This potentially higher clutter loss may result in an even lower AP/UE-to-SS interference in practice.

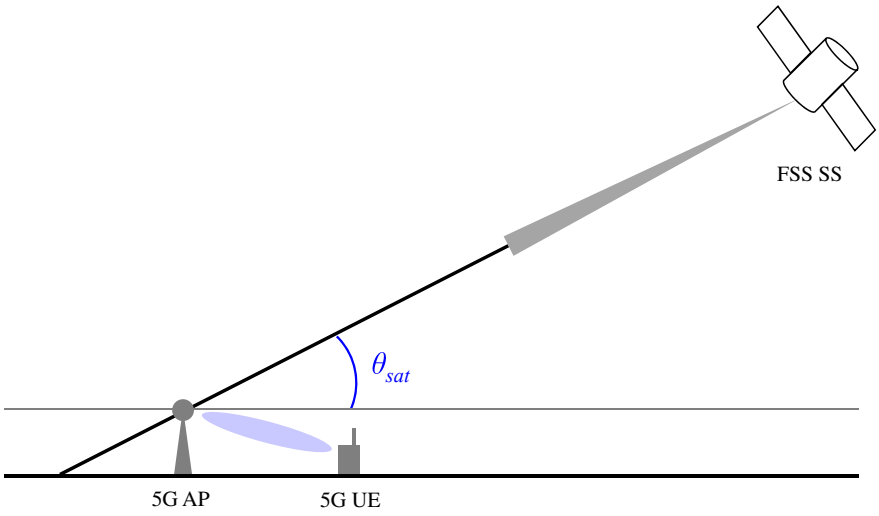

Figure 2.1: Topology of coexistence between a 5G system and an FSS SS on elevation plane

The threshold TH_{fss} of -12.2 dB in Tables 2.3 and 2.4 is derived from [55]. There is, however, general recognition in the satellite community that this interference level was developed when satellite networks were considered to be power limited, whereas today satellite networks tend to be interference limited and, as such, this protection level is very conservative [16]. Therefore more realistic and less stringent protection criteria of TH_{fss} of -6 dB and 0 dB are used in this paper. It is to be noted that TH_{fss} of -6 dB and 0 dB corresponding to 1dB and 3 dB desensitization (desense) interference thresholds, which represent the increase in the noise floor of the system due to interference, are also typically used for mobile terrestrial systems [56][57]. We use the same -6 dB and 0 dB I/N as the protection criteria for satellite systems in addition to -12.2 dB, since without the knowledge of the receiver characteristics of the satellite systems, it is difficult to derive a more precise value of the I/N protection criteria for the FSS SS and ES receivers. For 5G, TH_{5g} of -12.2 dB was also used in addition to -6 dB and 0 dB to be consistent with the FSS interference results.

Analysis of Interference

As a metric that measures AP/UE-to-SS interference, we calculate the number of simultaneously transmitting APs/UEs such that TH_{fss} at the FSS SS is not violated.

Here we provide an analysis framework for the AP-to-SS interference. With straightforward modifications, this framework can be also applied to the UE-to-SS interference. To compute such an aggregate interference, an interference from the downlink transmission of a single sector is computed by averaging over all possible downlink directions according to position

of the UE, which is given by

$$I_{5g} = \frac{1}{|\mathcal{R}_k^2|} \int_{\mathtt{x}_{ue}^{(k)} \in \mathcal{R}_k^2} \frac{P_{T,ap} G_{ap,a}\left(\mathtt{x}_{ue}\right) G_{ap,e}\left(\mathtt{x}_{ue}\right) G_{ss,3db}}{PL_{ap \to ss}} d\mathtt{x}_{ue} \tag{2.1}$$

where $\mathcal{R}_k^2$ is region of a sector and thus $|\mathcal{R}_k^2|$ is the area of a sector; $\mathtt{x}_{ue}$ is position of a UE in an $\mathcal{R}_k^2$; $P_{T,ap}$ is transmit power of an AP; $G_{ap,a}$ and $G_{ap,e}$ are the azimuth and elevation beamforming gains of a downlink transmission to a UE in the direction toward the SS; $G_{ss,3db}$ is the beamforming gain of the SS receiver antenna within its 3dB-contour; $PL_{ap \to ss}$ is the path loss between the AP and the SS.

For a 5G AP, the attenuation patterns of an antenna element on the elevation and azimuth plane are given by [62]

$$\begin{aligned} A_a\left(\phi\right) &= \min\left\{12\left(\frac{\phi}{\phi_{3db}}\right)^2, A_m\right\}, \\ A_e\left(\theta\right) &= \min\left\{12\left(\frac{\theta - 90^\circ}{\theta_{3db}}\right)^2, A_m\right\} \ [\text{dB}] \end{aligned} \tag{2.2}$$

where ϕ and θ are angles of a beam on the azimuth and elevation plane, respectively; $(\cdot)_{3db}$ denotes an angle at which a 3-dB loss occurs. Then the antenna element pattern that is combined in the two planes is given by

$$A\left(\theta, \phi\right) = \min\left(A_a\left(\phi\right) + A_e\left(\theta\right), A_m\right) \ [\text{dB}] \tag{2.3}$$

where A_m is a maximum attenuation (front-to-back ratio). It is defined $A_m = 30$ dB in [62], but it can be higher in practice. Finally, an antenna gain that is formulated as

$$G\left(\phi, \theta\right) = G_{max} - A\left(\phi, \theta\right) \ [\text{dB}] \tag{2.4}$$

where G_{max} is a maximum antenna gain.

Note that $G_{ap,a}$ and $G_{ap,e}$ are lower than the maximum azimuth and elevation beamforming gains. The reason is depicted in Fig. 2.1. Generally, a beam of an AP is pointed away from an SS since transmitting to a UE that is placed at a lower elevation than the AP. The elevation angles that are shown in Table 2.2 for each class of SS [54] are obtained in this manner.

Based on (2.1), we calculate an *aggregate* interference, which is given by

$$I_{aggr}\left(\mathbb{N}\left[\mathcal{S}_{5s}\right]\right) = I_{5g} \times \mathbb{N}\left[\mathcal{S}_{5s}\right] \tag{2.5}$$

where $\mathcal{S}_{5s}$ is a set of 5G sectors; $\mathbb{N}\left[\cdot\right]$ is the number of elements in a set. Now, we can obtain the number of simultaneously transmitting APs, $\mathbb{N}\left[\mathcal{S}_{5s}\right]$, such that I_{aggr} does not exceed TH_{fss}, which is given by

$$\text{argmax}_{\mathbb{N}[\mathcal{S}_{5s}]} I_{aggr}\left(\mathbb{N}\left[\mathcal{S}_{5s}\right]\right) < 10^{0.1\left(TH_{fss} + N_0\right)} \tag{2.6}$$

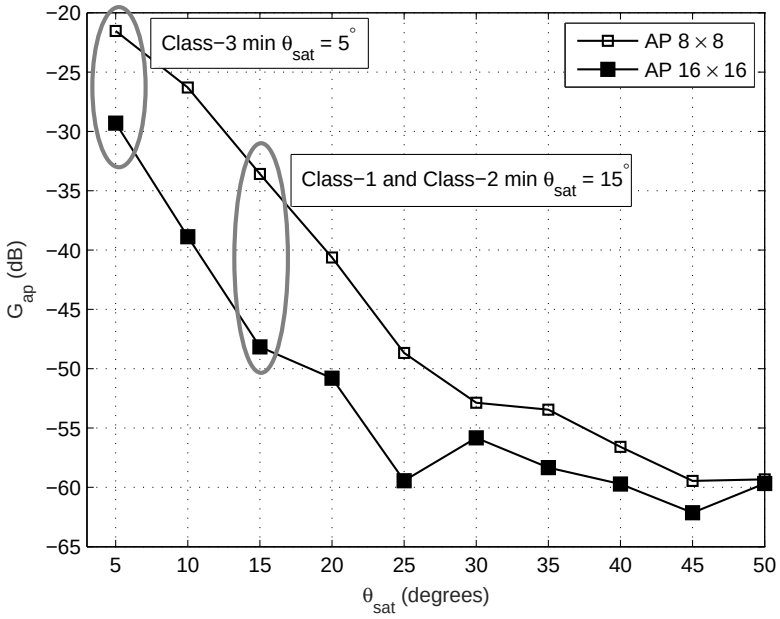

Figure 2.2: Normalized mean AP antenna gain into FSS SS vs. the elevation angle θ_{sat}

within an area that a satellite beam forms on the Earth surface. The receive antenna on board an SS forms a spot where a solid angle formed by the receive beam subtends the surface of the Earth; and this is typically known as a *spot beam*. It is assumed that the entire 5G system deployment falls within the 3dB-contour of an SS receiver spot beam.

Now we wish to know if such an "average-based" approach can represent an analysis of aggregate interference in the 5G-to-SS interference environment. First, it is widely accepted that the standard deviation decreases as the sample size is increased [59]. Since we deal with very large numbers of 5G transmitters as the interference source, the reliance on an average-based analysis achieves relevance. Second, a recent work [60] suggests a statistic method that models aggregate interference more accurately than a uniform distribution. The reference claims that for transmitters sufficiently far away from the point at which interference is to be estimated this is usually a very good approximation, provided that the overall density of interferers is properly chosen. It is noteworthy that the suggestion advocates the average-based approach of this dissertation in the given interference environment. The 5G-to-SS interference fits very well with the environment where the interfering TXs are positioned sufficiently far away from the interference is received.

Table 2.3: Results of 5G AP-to-FSS SS interference

SS class, Los/NLoS mix		**Result**			
		Mean individual-sector interference (dBm/Hz)	Maximum number of simultaneously transmitting sectors		
			TH_{fss} = -12.2 dB	-6 dB	0 dB
		AP EIRP = 62 dBm/100 MHz (8 × 8 array)			
Class 1	50% LoS / 50% NLoS	-213	2,000	8,000	32,000
	25% LoS / 75% NLoS	-216	3,800	15,200	60,800
	10% LoS / 90% NLoS	-220	9,000	36,000	144,000
Class 2	50% LoS / 50% NLoS	-213	1,200	4,800	19,200
	25% LoS / 75% NLoS	-216	2,300	9,200	36,800
	10% LoS / 90% NLoS	-220	5,400	21,600	86,400
Class 3	50% LoS / 50% NLoS	-217	2,200	8,800	35,200
	25% LoS / 75% NLoS	-219	4,400	17,600	70,400
	10% LoS / 90% NLoS	-223	10,000	40,000	160,000
		AP EIRP = 74 dBm/100 MHz (16 × 16 array)			
Class 1	50% LoS / 50% NLoS	-213	2,000	8,000	32,000
	25% LoS / 75% NLoS	-216	3,800	15,200	60,800
	10% LoS / 90% NLoS	-220	9,000	36,000	144,000
Class 2	50% LoS / 50% NLoS	-213	1,200	4,800	19,200
	25% LoS / 75% NLoS	-216	2,300	9,200	36,800
	10% LoS / 90% NLoS	-220	5,400	21,600	86,400
Class 3	50% LoS / 50% NLoS	-211	600	2,400	9,600
	25% LoS / 75% NLoS	-214	1,300	5,200	20,800
	10% LoS / 90% NLoS	-218	3,000	12,000	48,000

Evaluation of Interference

Tables 2.3 and 2.4 record our final results of (i) a mean individual-sector/UE interference power received at an SS receiver, I_{5g}/W from (2.1) where W is bandwidth of 5G, and (ii) the maximum number of simultaneous 5G sectors/UEs that can transmit under a TH_{fss}, $\arg\max_{\mathbb{N}[\mathcal{S}_{5s}]} I_{aggr}\left(\mathbb{N}\left[\mathcal{S}_{5s}\right]\right)$ from (2.6). To control interference from the APs towards an SS receiver, a Chebyshev sidelobe suppression technique of 30 dB is applied to the downlink transmit beams, and a mechanical downtilt of 6° is assumed for the AP antenna arrays. No specific interference control techniques were assumed at the UEs.

AP-to-SS Interference: Table 2.3 shows that potentially very large numbers of simultaneously transmitting sectors can be supported. For example, even using a very conservative -12.2 dB of TH_{fss}, Table 2.3 shows that with increased EIRP of an AP from 62 to 74 dBm/100 MHz, the number of active AP sectors that can simultaneously transmit is kept

Table 2.4: Results of 5G UE-to-FSS SS interference

SS class, Los/NLoS mix		**Result**			
		Mean individual-UE interference (dBm/Hz)	Maximum number of simultaneously transmitting UEs		
			TH_{fss} = -12.2 dB	- 6 dB	0 dB
Class 1	25% LoS / 75% NLoS	-225	283,000	1,132,000	4,528,000
	10% LoS / 90% NLoS	-228	566,000	2,264,000	9,056,000
	100% NLoS	-238	6,226,000	24,904,000	99,616,000
Class 2	25% LoS / 75% NLoS	-217	28,000	112,000	448,000
	10% LoS / 90% NLoS	-220	57,000	228,000	912,000
	100% NLoS	-230	627,000	2,508,000	10,032,000
Class 3	25% LoS / 75% NLoS	-223	64,400	257,800	1,031,200
	10% LoS / 90% NLoS	-227	162,000	648,000	2,591,800
	100% NLoS	-237	1,781,900	7,127,500	28,510,100

the same for both Class 1 and Class 2 FSS systems, although the number drops for Class 3 FSS systems. This result has certain implications on the deployment of 5G systems. Specifically, an environment with higher NLoS yields lower interference into an SS receiver, due to higher attenuation of the interfering signal power. In other words, a higher density of 5G sectors can be deployed in urban areas than in suburban areas.

Fig. 2.2 provides a justification for this drop. It depicts the *normalized* (assuming maximum antenna gain is normalized to 0 dBi) transmit antenna gain of a sector toward an SS, which is given by $G_{ap} = -A(\phi, \theta)$ from (2.4) with $G_{max} = 0$. In general, an AP has a lower antenna gain toward an SS with a larger antenna array, since the beamwidth is reduced with increasing number of transmit antennas. Conversely, the antenna gain toward an SS is increased with higher number of transmit antennas if an SS falls within the main beam of an AP. The main difference between Class 3 and the other two classes is the elevation angle θ_{sat}, as depicted in Fig. 2.1. According to Table 2.2, Class 3 SSs operate at a lower elevation angle than the other two classes, thus they experience higher interference due to increased transmit antenna count at the APs.

Due to several reasons, the numbers given in Table 2.3 likely underestimate the actual number of APs that could be deployed without violating TH_{fss}. Firstly, in real-world networks, it is unlikely that all 5G sectors simultaneously transmit. In fact, in current deployments, network loading rarely exceeds 30% [54], thus allowing a roughly three-fold increase in the number of sectors given in Table 2.3 without adversely impacting FSS links. Secondly, the results only consider *outdoor* deployments. Indoor APs will not contribute to aggregate interference levels observed at the SS receivers due to very high penetration losses that occur

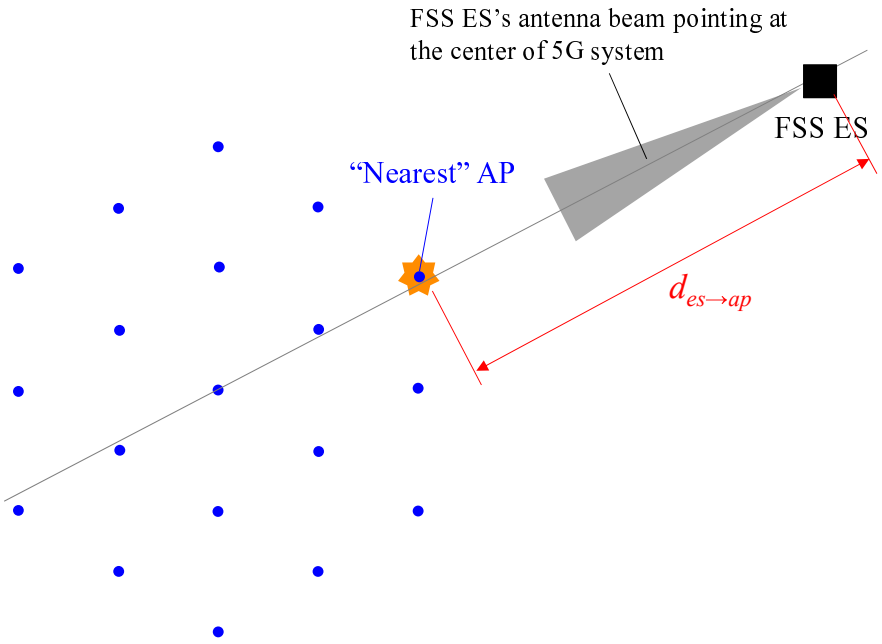

Figure 2.3: Azimuth plane of a 5G-FSS ES coexistence topology

in mmW bands. Finally, this study assumes that all APs are synchronized and analyzes interference during a downlink period when all APs are in transmit mode. If geographically-adjacent network deployments of several operators are not synchronized, then their respective downlink periods will not occur simultaneously. Thus, even a smaller percentage of APs will be in transmit mode simultaneously, whereas the remainder of active APs will be receiving uplink transmissions from UEs. As transmission of a UE is expected to have much smaller impact on an SS, the overall interference from a 5G deployment area will be further reduced. In summary, fractional network loading, indoor deployments, and unsynchronized network deployments result in a more favorable scenario than what was modeled to obtain the results in Table 2.3.

UE-to-SS Interference: Here we provide an initial set of results on the UE-to-SS interference. The interference calculation steps mirror those for the AP-to-SS interference given in (2.1)-(2.6), but with the UE parameters given in Table 2.1. Namely, based on the statistics of the UE antenna array gains into an SS receiver, a per-UE average interference value is computed in Table 2.4. From that, the number of *simultaneously transmitting* UEs is derived, given a certain interference threshold at the SS. Note that unlike on the downlink where under heavily loaded APs continuously transmit, UE transmissions on the uplink are scheduled periodically, as all available uplink slots are shared between the active UEs in a 5G cell. Assuming a typical *heavy-load* approximation of 10 active UEs per sector, the number of *active* UEs per sector becomes roughly 10 times that of the simultaneously transmitting

UEs. The final numbers of supported active UEs in a 5G deployment area under various LoS/NLoS channel conditions are given in Table 2.4. Note that the highest probability of LoS for the UE-to-SS links was assumed to be 25%.

We make two key observations on the UE-to-SS results: i) the number of active UEs supportable in a 5G system far exceeds the number of simultaneously transmitting APs given in Table 2.3. This is mainly due to the increased probability of NLoS for the UEs and the intermittent nature of the UE uplink transmissions, where we have assumed a per UE transmission duty cycle of 10% to convert the number of simultaneously transmitting UEs into the number active UEs.; (ii) these results may still significantly underestimate the total number of active 5G UEs that can be supported in a 5G system, as a significant fraction the UEs may be situated indoors or inside vehicles and have very high path loss towards the SS receivers.

2.3.2 Interference from FSS ES to 5G AP

System Model

The analysis is based on a link-level protection criterion that is defined as an I/N observed at a 5G AP receiver. Specifically for our results, the link-level protection thresholds, denoted by TH_{5g}, are set to -12.2, -6, and 0 dB of I/N. Based on the link-level protection criterion, we define a system-level interference protection criterion as the minimum distance between an FSS ES and the *edge* of the 5G system deployment, such that 95% of the 5G uplink connections in the cell nearest to the ES transmitter are protected under TH_{5g}. The distance to the edge of the system deployment is defined as the minimum distance between the ES and the 5G AP that is nearest to it. Fig. 2.3 illustrates an example of the 5G system layout and the definition of the minimum protection distance. The parameters used for this study refer to Table 2.1. For the terrestrial propagation between an ES transmitter and APs, the following three models are assumed: FSPL [52], Urban Macro (UMa), and Rural Macro (RMa) [62].

Each AP activates an elevation and azimuth beam to receive the intended uplink transmission based on the preferred azimuth and elevation beam index feedback from the UE. Each UE selects its preferred elevation and azimuth beam from the elevation and azimuth codebook based on the long-term received power measurements obtained for all beams in the codebooks. For the results reported here, a codebook with 16 entries was used for beam selection in the azimuth and elevation dimensions. The beam patterns are symmetric in elevation and azimuth planes.

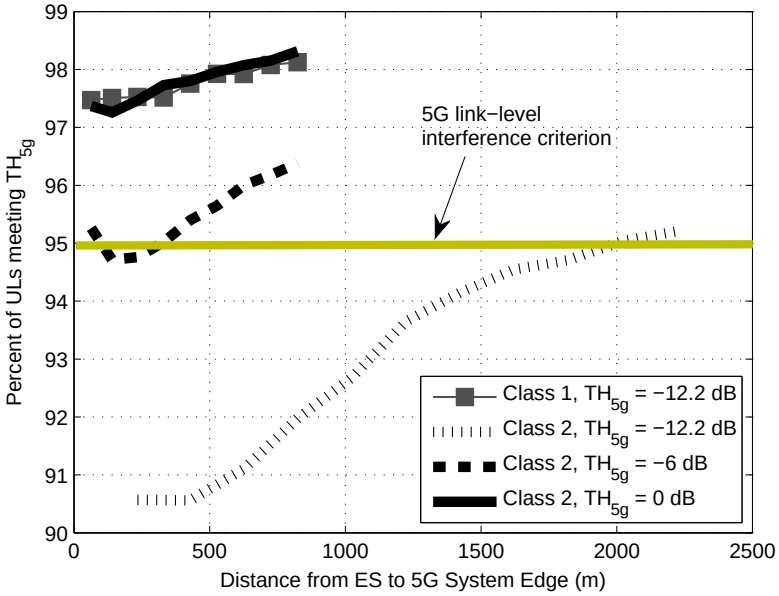

Figure 2.4: 5G uplinks with Classes 1 and 2 ES under FSPL

Analysis of Interference

Given the preferred azimuth and elevation beam, an interference received from an ES at a 5G AP is computed as

$$I_{es} = \frac{P_{T,es} G_{es,a} G_{ap,a}\left(\mathtt{x}_{ue}\right) G_{ap,e}\left(\mathtt{x}_{ue}\right)}{PL_{es\rightarrow ap}\left(d_{es\rightarrow ap}\right)} \tag{2.7}$$

where the parameters are defined in the same manner as in (2.1). The transmit power of the ES node is denoted by $P_{T,es}$. The azimuth pattern of an ES, $G_{es,a}$, is defined in [58]. For the interference analysis, the value of $EIRP_{es} = P_{T,es} + G_{max,es}$ (where $G_{max,es}$ is the maximum transmit antenna gain for the ES node) is specified according to the three classes of ES transmitters [54] given by: 12.2, 24.1, and 48 dBm/MHz for Class 1, 2, and 3, respectively.

Given a certain level of $EIRP_{es}$ and position of the ES relative to the 5G system layout, an ES-to-5G interference is calculated for every UE attached to the *nearest* AP. Each calculation is performed with randomized positions of the UEs in the system and randomized positions of the ES around the 5G system layout, with variation of $d_{es\rightarrow ap}$. It is assumed that the ES antenna azimuth is always directed toward the center of the 5G system layout.

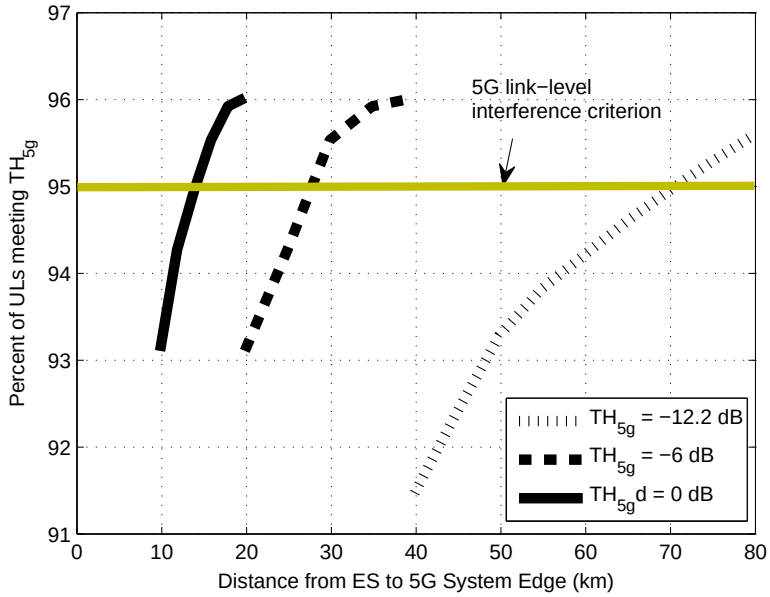

Figure 2.5: 5G uplinks with Class 3 ES under FSPL

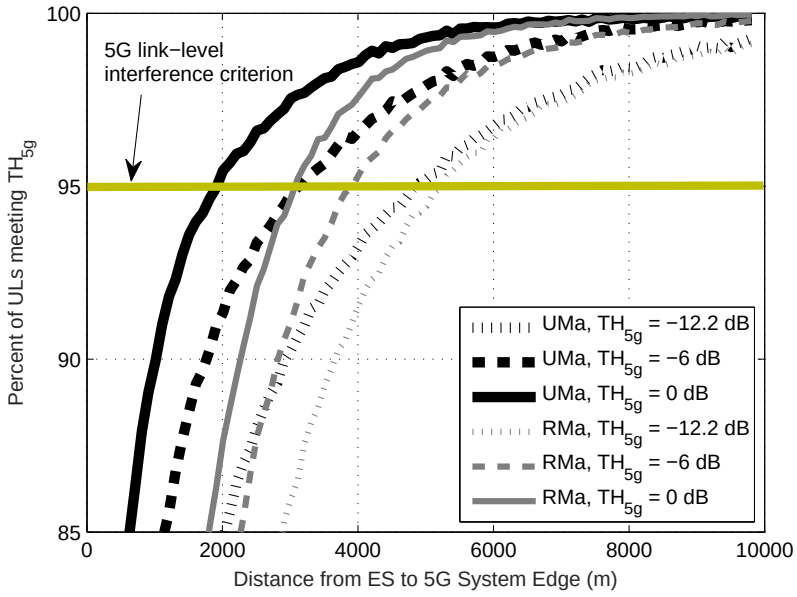

Figure 2.6: 5G uplinks with Class 3 ES under UMa and RMa

Table 2.5: Required separation distance under UMa and RMa

	UMa			RMa		
TH_{5g} (dB)	-12.2	-6	0	-12.2	-6	0
Required $d_{es\rightarrow ap}$ (m)	4,900	3,000	2,000	5,100	4,000	3,000

Evaluation of Interference

Figs. 2.4 and 2.5 demonstrate cumulative distribution functions (CDFs) of the uplink connections computed over all UE positions in the nearest cell as a function of $d_{es\rightarrow ap}$ for Classes 1 and 2, and for Class 3, respectively. Given the 95% protection target, the minimum $d_{es\rightarrow ap}$ can be determined from Figs. 2.4 and 2.5. As evident in the figures, the required $d_{es\rightarrow ap}$ is highly dependent on TH_{5g} as well as $EIRP_{es}$ toward the 5G system.

Based on the above results, we observe that the required values of $d_{es\rightarrow ap}$ are reasonable in most cases of interest and will not place an overly restrictive set of constraints on future 5G system deployments. With a protection margin of -6 dB I/N, the distance where less than 5% of links fall below the protection threshold TH_{5g} is less than 400 m for Class 2 ESs and less than 50 m for Class 1 ESs. While our calculations show that Class 3 ESs nominally could interfere with 5G systems at a distance of 28 km with a -6 dB of I/N threshold, we believe that this distance could be significantly smaller in practice due to additional clutter loss between 5G APs and ES transmitters not accounted in the FSPL model.

To more accurately model the terrestrial propagation effect, such as the clutter loss, we also generated results using the 3GPP UMa and RMa models [62] for Class 3 ES transmitters. The 3GPP UMa and RMa path loss models exhibit much higher path loss exponents than the FSPL and are more appropriate for terrestrial propagation modeling. Fig. 2.6 exhibits the percent of 5G uplinks below TH_{5g} in presence of interference from an FSS ES based on Class 3. Compared to Fig. 2.5, $d_{es\rightarrow ap}$ is dramatically reduced. This implies that a 5G system experiences lower interference from an ES when deployed in an environment with higher attenuation–mainly due to higher probability of NLoS propagation conditions.

Table 2.5 shows the results with both 3GPP path loss models for Class 3 ES transmitters for various I/N thresholds. As expected, the RMa model requires a larger distance for interference protection, since in general it predicts higher LoS probability as a function of distance and has a lower path loss exponent than UMa. Specifically, the table indicates that the worst case of protection distance of 5,100 m occurs with RMa and the most restrictive threshold of TH_{5g} (-12.2 dB).

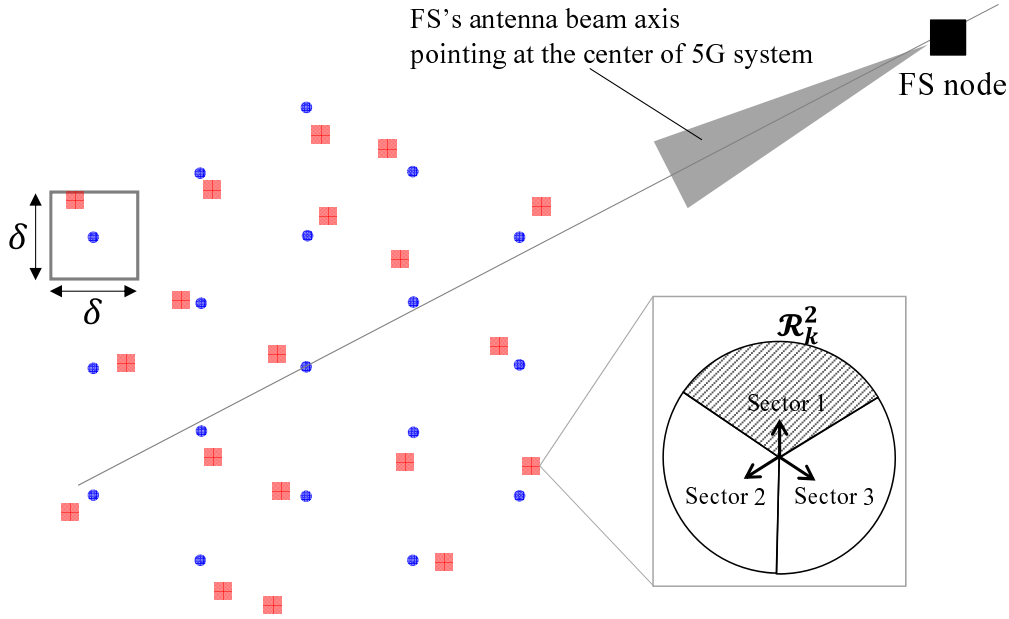

Figure 2.7: Topology of a 5G-FS coexistence

2.4 Coexistence of 5G with Fixed Service at 70 GHz

In this section, we discuss co-channel coexistence of 5G at 70 GHz where the Fixed Service (FS) is the incumbent system. We consider a point-to-point Wireless Backhaul (WB) system that adopts highly directional antennas to connect distant radio towers. Note that the FS system provides backhaul for another cellular system, thus it is uncoordinated with the 5G.

Unlike the 28-GHz coexistence problem, there are four possible interference scenarios: FS to AP, AP to FS, FS to UE, and UE to FS. The reasons are as follows: (i) both directions of an FS system's wireless link transmit in the 70 GHz band; (ii) a UE has higher probability of LoS than in the coexistence at 28 GHz since the beam of an FS's antenna is placed terrestrially and pointed closer toward the ground.

Note that this analysis framework is sufficiently general in that it can be readily applied to coexistence scenarios between 5G and other terrestrial incumbent system.

2.4.1 System Model

The parameters for 5G and FS are summarized in Table 2.6. Note that the parameters of 5G are different from the ones used in the 28 GHz coexistence of Section 2.3. Since the rules are still under discussion by the FCC for the 70 GHz band, the parameters are obtained from a

standard 3GPP evaluation model [17]. We assume 19 cell sites–equivalently 19 APs–where in total $\mathbb{N}[\mathcal{S}_{5s}] = 57$ sectors exist.

Fig. 2.7 describes a *drop*–or an instance–of topology for coexistence. There are two important assumptions: (i) the FS node is regarded as a transmitter in an FS-to-5G interference scenario while it is a receiver in a 5G-to-FS interference situation; (ii) the FS node points its beam at the center of the 5G system. The interference between the 5G and the FS nodes is a function of at least four variables corresponding to the positions of transmitters and receivers in the interferer and victim systems. Since the FS node is always assumed to point its beam at the center of the 5G system, position of the FS receiver in the FS-to-5G scenario and position of FS transmitter in the 5G-to-FS scenario can be excluded from consideration. In Fig. 2.7, the FS node is placed outside of the 5G system, at 176 different positions on an r-θ coordinate: $r = [0 : 500 : 10,500]$ and $\theta = [0 : \frac{\pi}{4} : \frac{7\pi}{4}]$ in reference to the center of the 5G system.

The blue circles in Fig. 2.7 correspond to positions of the APs in a classical hexagonal cell layout with Inter-Site Distance (ISD) of 200 m. The actual positions of APs (red squares) are *dithered* within δ m relative to the locations of the hexagonal cells, to achieve a more realistic system layout. Furthermore, we uniformly and randomly distribute 10 UEs in the kth sector region, denoted by $\mathcal{R}_k^2$. The distribution of UEs can be modeled as a homogeneous PPP [51] whose density is kept constant to be $\lambda_{ue} = 10$ over $\mathcal{R}_k^2, k = 1, 2, \cdots, \mathbb{N}[\mathcal{S}_{5s}] = 57$.

For the path loss model, we use the 3GPP UMa and UMi [62]. The models are used both for the 5G-FS and AP-UE links. Again, although 3GPP defines path loss models for outdoor and indoor scenarios, this paper discusses the 5G placed outdoor only since the FS devices are likely placed outdoors and penetration losses at 70 GHz are very high.

The antenna element pattern for the 5G system refers to (2.2) through (2.4) in Section 2.3.1. The antenna beam pattern for an FS device is provided in [63] as

$$G_{fs}(\theta) = \begin{cases} G_{max} - 2.5 \times 10^{-3} \left(\frac{D}{\lambda}\theta\right)^2, & 0^\circ < \theta < \theta_m \\ G_1, & \theta_m \le \theta < \theta_r \\ 32 - 25 \log \theta, & \theta_r \le \theta < 48^\circ \\ -10, \ [\text{dB}] & 48^\circ \le \theta \le 180^\circ \end{cases} \tag{2.8}$$

where G_{max} is a maximum gain; D is antenna diameter; λ is a wavelength; $G_1 = 2 + 15 \log \frac{D}{\lambda}$: gain of the first sidelobe; $\theta_m = \frac{20\lambda}{D}\sqrt{G_{max} - G_1}$ in degrees; $\theta_r = 15.85 \left(\frac{D}{\lambda}\right)^{-0.6}$ in degrees.

2.4.2 Analysis of Interference

Coexistence Topology

We now discuss a general framework for interference analysis that is applicable to all the four scenarios of interference, where the key is to analyze how antenna gains are determined for

Table 2.6: Parameters for 70-GHz coexistence

Parameter	**5G**		**FS**
Carrier frequency	73.5 GHz		
Path loss model [62]	UMa and UMi		
Bandwidth	1 GHz		
System	AP	UE	WB
Transmit power	15 dBm per element	14 dBm per element	19 dBm
Max antenna gain	8 dBi per element	5 dBi per element	50 dBi
Temperature	290 K	290 K	290 K
Noise figure	7 dB	9 dB	5 dB
Antenna height	10 m	1.5 m	25 m
Number of antennas	8×8 and 16×16 ($\lambda/2$ array)	Omni and 4×4 ($\lambda/2$ array)	

(i) the interferer system's transmitters and (ii) the victim system's receivers. Let $\mathtt{x} = (x, y)$ denote position of a node on a two-dimensional Cartesian coordinate plane. Subscripts "i" and "v" indicate the "interferer" and "victim", respectively, and "t" and "r" denote "transmitter" and "receiver", respectively. Without loss of generality, we consider the AP-to-FS interference where $\mathtt{x}_{i,t}$, $\mathtt{x}_{i,r}$, and $\mathtt{x}_{v,r}$ denote the positions of an AP, a UE, and the FS receiver respectively. The method can be extended to the other scenarios (i.e., FS to AP, UE to FS, and FS to UE).

Fig. 2.8 illustrates the azimuth plane of an AP-to-FS interference scenario. There are two angles that determine the interference level between a 5G AP and the FS node: the off-axis angle, ϕ_{off}, and the steering angle, ϕ_{str}. A ϕ_{str} is an angle between the direction of a beamforming and the antenna's physical orientation. Such an electrical steering is only assumed for the 5G (i.e., APs and UEs), whereas the FS assumed to be equipped with fixed beam antennas. Also, we define an *interference axis* to be a line connecting the interfering transmitter (the AP) and the victim receiver (the FS receiver). A ϕ_{off} is an angle between the direction of a beamforming and the interference axis. These angles will be used in the analysis to represent discrimination of antenna gain from (i) electrical steering and (ii) pointing away from the FS receiver, respectively.

For defining the angles, we put an azimuth-plane geometry on a quadrant and set $\mathtt{x}_{i,t}$ at the origin of the quadrant. The angle formed by the interference axis with respect to the X-axis is denoted by ϕ_1. The angle of a sector's physical orientation is denoted by and set as $\phi_2 = 90°$. The beamforming angle with respect to the X-axis of the quadrant is denoted

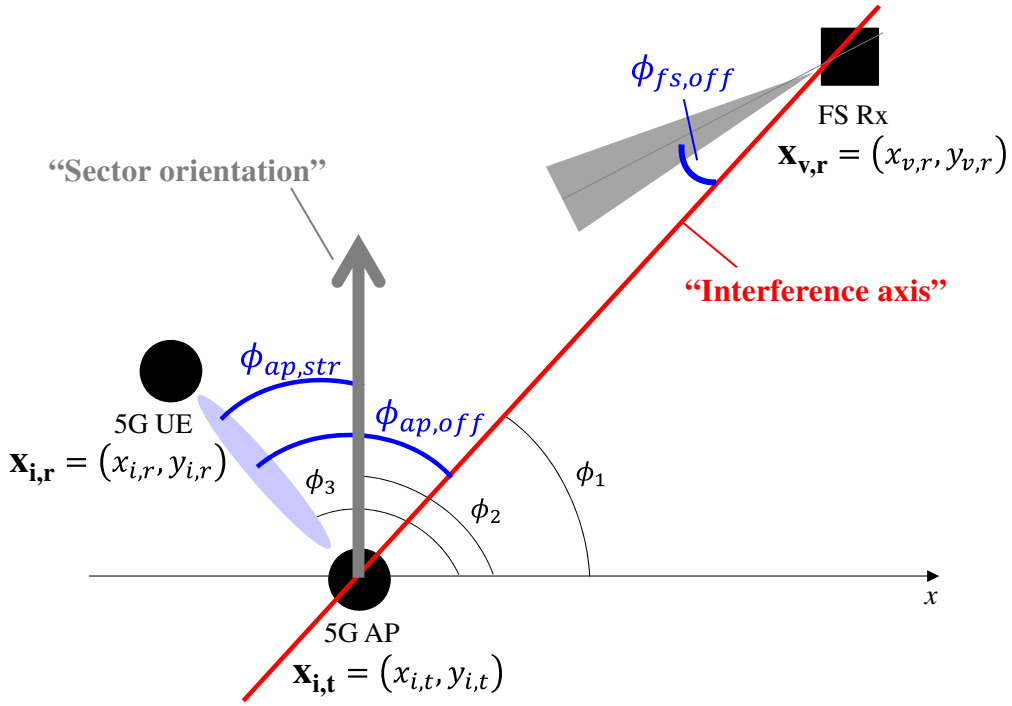

Figure 2.8: 5G AP as interferer on the azimuth plane (Cell orientation of 90°)

as ϕ_3. Now we can define ϕ_{off} and ϕ_{str} for the 5G AP and FS receiver as

$$\phi_{ap,off}\left(\mathbf{x}_{i,t}, \mathbf{x}_{i,r}, \mathbf{x}_{v,r}\right) = \phi_3 - \phi_1 \tag{2.9}$$

$$\phi_{ap,str}\left(\mathbf{x}_{i,t}, \mathbf{x}_{i,r}\right) = \phi_3 - \phi_2 \tag{2.10}$$

$$\phi_{fs,off}\left(\mathbf{x}_{i,t}, \mathbf{x}_{v,t}, \mathbf{x}_{v,r}\right) = \arccos\left(\frac{\left(\mathbf{x}_{v,t} - \mathbf{x}_{v,r}\right) \cdot \left(\mathbf{x}_{i,t} - \mathbf{x}_{v,r}\right)}{\|\mathbf{x}_{v,t} - \mathbf{x}_{v,r}\| \|\mathbf{x}_{i,t} - \mathbf{x}_{v,r}\|}\right) \tag{2.11}$$

where $(\cdot)$ in (2.11) indicates a dot product between two vectors, and

$$\phi_1 = \arctan\left(\mathbf{x}_{v,r}, \mathbf{x}_{i,t}\right) = \arctan\left(\frac{y_{v,r} - y_{i,t}}{x_{v,r} - x_{i,t}}\right) \tag{2.12}$$

$$\phi_3 = \arctan\left(\mathbf{x}_{i,r}, \mathbf{x}_{i,t}\right) = \arctan\left(\frac{y_{i,r} - y_{i,t}}{x_{i,r} - x_{i,t}}\right). \tag{2.13}$$

Now, denote azimuth and elevation planes by subscripts "a" and "e," respectively. Then two types of attenuation, $A_{ap,a,off}\left(\phi_{ap,off}\right)$ and $A_{ap,a,str}\left(\phi_{ap,str}\right)$, can be obtained by substituting $\phi_{ap,off}$ and $\phi_{ap,str}$ into $A_a\left(\phi\right)$ in (2.2), where $\phi_{ap,off,3db} = 6°$ and $\phi_{ap,str,3db} = 65°$ [62].

Fig. 2.9 describes an elevation plane of the interference scenario of interest. Similarly to the azimuth-plane analysis, the off-axis angles of the interfering transmitter and the victim

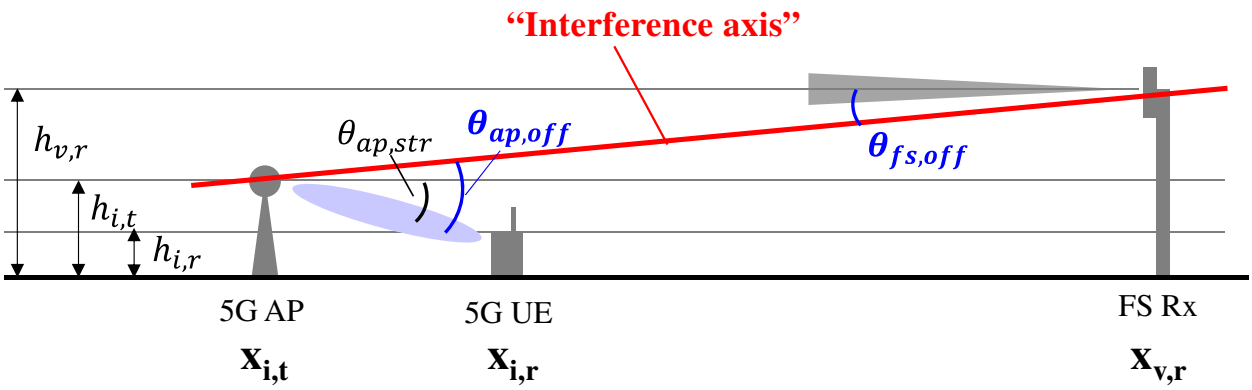

Figure 2.9: 5G AP as interferer on the elevation plane

receiver, $\theta_{ap,off}$ and $\theta_{fs,off}$, are defined with respect to the interference axis. The angles can be calculated based on locations and heights, which are given by

$$\theta_{ap,off} = \arctan\left(\frac{h_{v,r} - h_{i,t}}{\|\mathbf{x}_{v,r} - \mathbf{x}_{i,t}\|}\right) + \theta_{ap,str} \tag{2.14}$$

$$\theta_{fs,off} = \arctan\left(\frac{h_{v,r} - h_{v,t}}{\|\mathbf{x}_{v,r} - \mathbf{x}_{v,t}\|}\right). \tag{2.15}$$

Note that although it is set $h_{v,t} = h_{v,r}$ in Fig. 2.9, it can be generalized as in (2.15). Again, by substituting $\theta_{ap,off}$ into $A_e(\theta)$ in (2.2), we can obtain $A_{ap,e,off}(\theta_{ap,off})$ with $\theta_{ap,off,3db} = 6°$ and $\theta_{ap,str,3db} = 65°$ [62].

Also, for the FS receiver, the azimuth and elevation off-axis angles, $\phi_{fs,off}$ and $\theta_{fs,off}$, are substituted into (2.8) to obtain the $G_{fs}(\phi_{fs,off})$ and $G_{fs}(\theta_{fs,off})$.

Analysis Framework

An interference power received at a victim receiver is computed as

$$I = \frac{P_T G_i(\phi_i, \theta_i) G_v(\phi_v, \theta_v)}{PL(\mathbf{x}_{i,t}, \mathbf{x}_{v,r})} \tag{2.16}$$

where P_T denotes a transmit power of the interferer system's transmitter; $G(\cdot)$ denotes an antenna gain that is given in (2.4). Again, for a 5G device (either AP or UE), the angles $\phi_{i \text{ or } v}$ and $\theta_{i \text{ or } v}$ include ϕ_{off} and ϕ_{str}, and θ_{off} and θ_{str}. It is important to note that although not explicitly expressed, an I is a function of $(\mathbf{x}_{i,t}, \mathbf{x}_{v,t}, \mathbf{x}_{v,r})$ in an FS-to-5G interference and $(\mathbf{x}_{i,t}, \mathbf{x}_{i,r}, \mathbf{x}_{v,r})$ in a 5G-to-FS interference, which can be expressed through (2.9) and (2.11)

and written as

$$I = \begin{cases} I_{fs\to ap}\left(\mathtt{x}_{i,t}, \mathtt{x}_{v,t}, \mathtt{x}_{v,r}\right) \\ I_{ap\to fs}\left(\mathtt{x}_{i,t}, \mathtt{x}_{i,r}, \mathtt{x}_{v,r}\right). \end{cases} \tag{2.17}$$

Also, $PL\left(\cdot\right)$ is a path loss that is a function of $\mathtt{x}_{i,t}$ and $\mathtt{x}_{v,r}$. By generalizing an expression for path loss given in [62] as $PL = \xi d^{\alpha}$ where d is a distance, one can rewrite (3.3) as

$$I = P_T G_i\left(\phi_i, \theta_i\right) G_v\left(\phi_v, \theta_v\right) \xi^{-1} \|\mathtt{x}_{i,t} - \mathtt{x}_{v,r}\|^{-\alpha}. \tag{2.18}$$

5G as Interferer

Based on (2.18), we can calculate 5G-to-FS interference. The analysis focuses on the AP-to-FS interference only but can readily be extended to the UE-to-FS scenario. We consider an aggregate AP-to-FS interference with the 5G system that is fully loaded in both downlink and uplink. An aggregate interference is defined as an interference that is received at a *victim* FS receiver at $\mathtt{x}_{v,r}$ from all the 5G sectors, which can be formulated as

$$\begin{aligned} I_{aggr} &= \sum_{k=1}^{\mathbb{N}[\mathcal{S}_{5s}]} I_{ap\to fs}^{(k)}\left(\mathtt{x}_{i,t}^{(k)}, \mathtt{x}_{i,r}^{(k)}, \mathtt{x}_{v,r}\right) \\ &= P_T \xi^{-1} \sum_{k=1}^{\mathbb{N}[\mathcal{S}_{5s}]} G_i^{(k)}\left(\phi_i, \theta_i\right) G_v^{(k)}\left(\phi_v, \theta_v\right) \|\mathtt{x}_{i,t}^{(k)} - \mathtt{x}_{v,r}\|^{-\alpha} \end{aligned} \tag{2.19}$$

where a superscript (k) indicates that the quantity is defined for a sector region, $\mathcal{R}_k^2$; a set of AP sectors is denoted by $\mathcal{S}_{5s}$.

Now we need to compute the mean of aggregate interference over all the possible positions of $\mathtt{x}_{i,t}^{(k)}$, $\mathtt{x}_{i,r}^{(k)}$ and $\mathtt{x}_{v,r}$, which is given by

$$\begin{aligned} &\bar{I}_{aggr} \\ &= \mathbb{E}\left[I_{aggr}\right] \\ &= \underbrace{\frac{1}{\mathbb{N}\left[\mathcal{S}_{fs}\right]} \sum_{\mathcal{S}_{fs}}}_{\text{average of } \mathtt{x}_{v,r}} \sum_{k=1}^{\mathbb{N}[\mathcal{S}_{5s}]} \underbrace{\frac{1}{\delta^2} \int_{\mathtt{x}_{i,t}^{(k)}}}_{\text{average of } \mathtt{x}_{i,t}^{(k)}} \underbrace{\frac{1}{|\mathcal{R}_k^2|} \int_{\mathtt{x}_{i,r}^{(k)} \in \mathcal{R}_k^2}}_{\text{average of } \mathtt{x}_{i,r}^{(k)}} \\ &\qquad\qquad \left(I_{ap\to fs}^{(k)}\right) d\mathtt{x}_{i,r}^{(k)} d\mathtt{x}_{i,t}^{(k)} \\ &= \frac{P_T \xi^{-1}}{\delta^2 \left|\mathcal{R}_k^2\right| \mathbb{N}\left[\mathcal{S}_{fs}\right]} \sum_{\mathcal{S}_{fs}} \sum_{k=1}^{\mathbb{N}[\mathcal{S}_{5s}]} \int_{\mathtt{x}_{i,t}^{(k)}} \int_{\mathtt{x}_{i,r}^{(k)} \in \mathcal{R}_k^2} \\ &\qquad \left(G_i^{(k)}\left(\phi_i, \theta_i\right) G_v^{(k)}\left(\phi_v, \theta_v\right) \|\mathtt{x}_{i,t}^{(k)} - \mathtt{x}_{v,r}\|^{-\alpha}\right) d\mathtt{x}_{i,r}^{(k)} d\mathtt{x}_{i,t}^{(k)} \end{aligned} \tag{2.20}$$

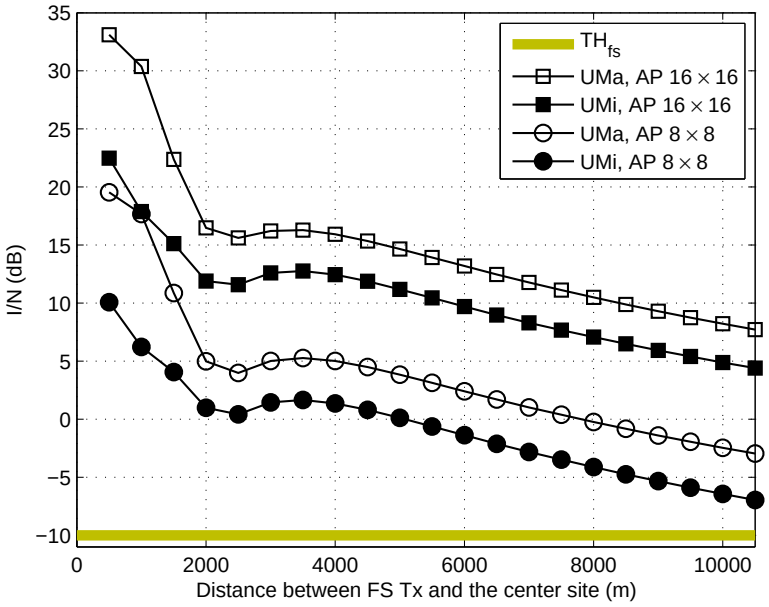

Figure 2.10: Interference from 5G APs to FS

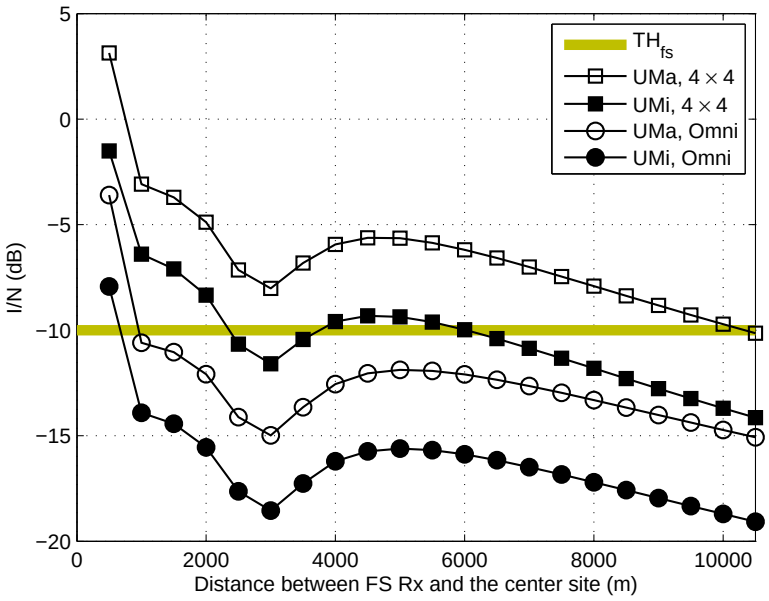

Figure 2.11: Interference from 5G UEs to FS

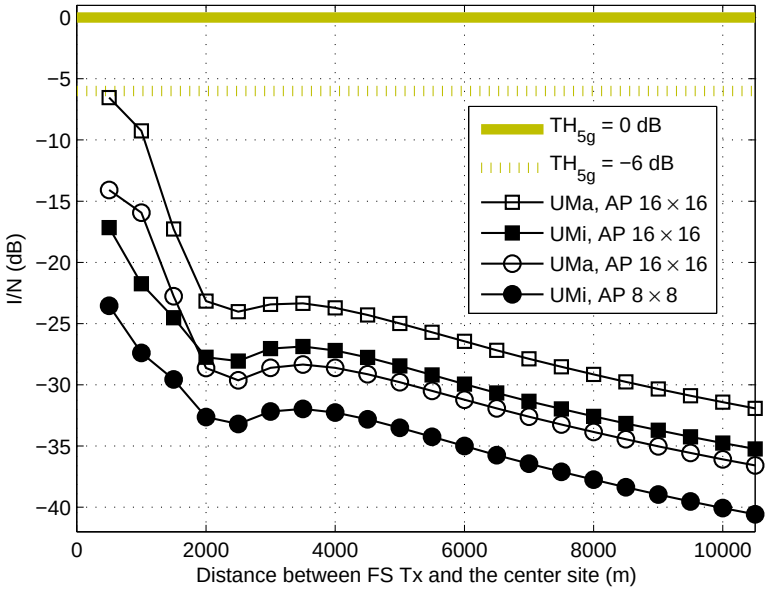

Figure 2.12: Interference from FS to 5G APs

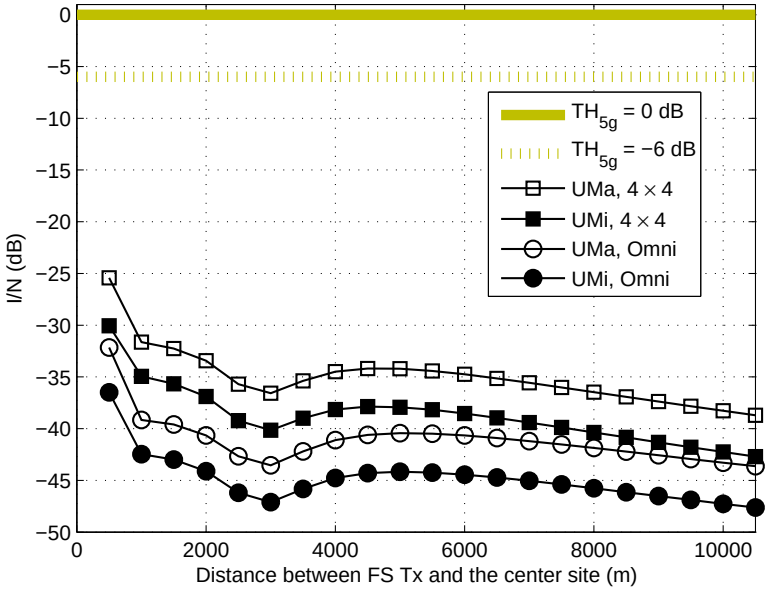

Figure 2.13: Interference from FS to 5G UEs

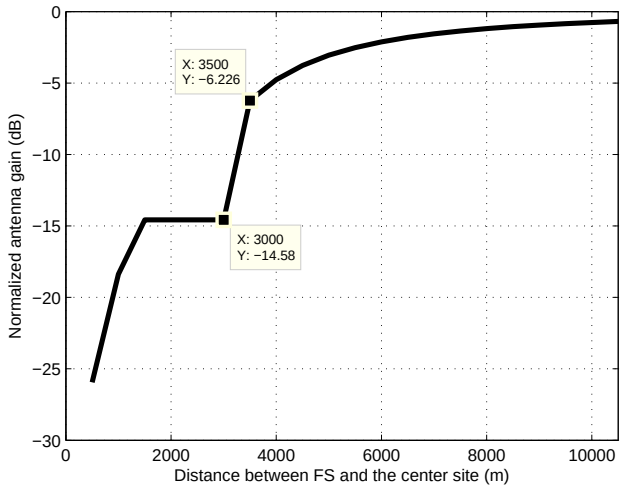

(a) Elevation antenna gain of FS, $G_{fs,e}\left(\theta_{fs,off}\right)$

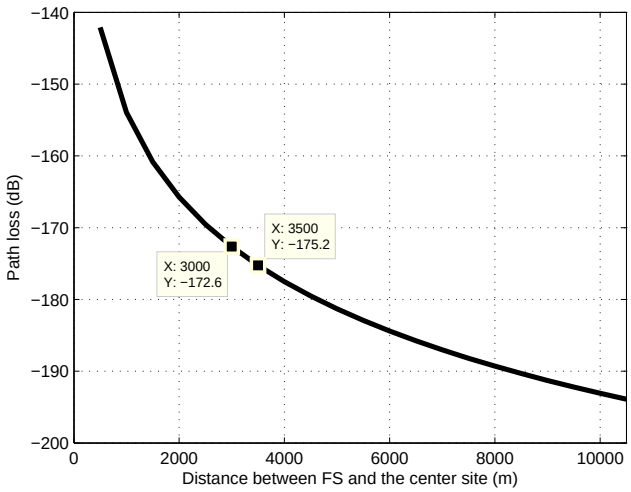

(b) Path loss, $PL_{5g\rightarrow fs}$

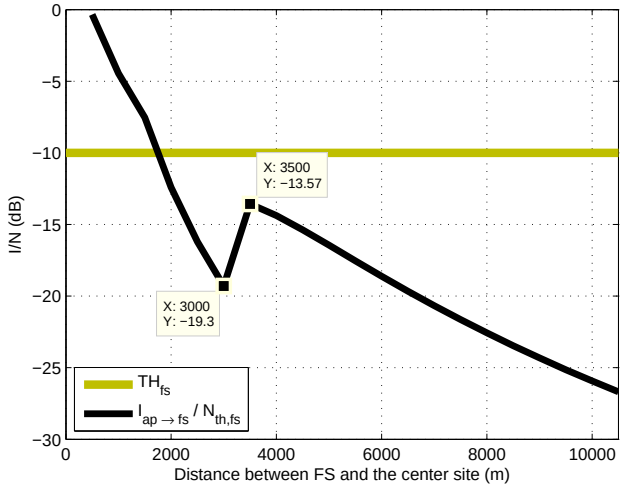

(c) Resulting AP-to-FS interference

Figure 2.14: Non-convexity in 5G-to-FS interference

where $\mathcal{S}_{fs}$ denotes a set of positions of the FS node. The integral expression in (2.20) is not amenable to analytic evaluation due to high complexity in calculation. Therefore, in the rest of the paper we evaluate (2.20) via Monte-Carlo simulations.

5G as Victim

The FS-to-5G interference is a *per-sector* interference power averaged over the $\mathbb{N}[\mathcal{S}_{5s}] = 57$ sectors. As above and without loss of generality, we analyze the FS-to-AP interference scenario in detail, and this analysis is applicable to the FS-to-UE interference scenario by replacing parameters for the AP with those for the UE. From (3.4), the average interference that is received at an AP located at $\mathtt{x}_{v,r}^{(k)}$ and pointing its receive beam at a UE located at $\mathtt{x}_{v,t}^{(k)}$ in $\mathcal{R}_k^2$ can be formulated as

$$I_{avg} = \frac{1}{\mathbb{N}[\mathcal{S}_{5s}]} \sum_{k=1}^{\mathbb{N}[\mathcal{S}_{5s}]} I_{fs\to ap}^{(k)} \left(\mathtt{x}_{v,t}^{(k)}, \mathtt{x}_{v,r}^{(k)}, \mathtt{x}_{i,t} \right). \tag{2.21}$$

Similarly to (2.20), an average of (2.21) over all the possible positions of $\mathtt{x}_{v,t}^{(k)}$, $\mathtt{x}_{v,r}^{(k)}$, and $\mathtt{x}_{i,t}$ can be calculated as

$$\begin{aligned} \bar{I}_{avg} &= \mathbb{E}[I_{avg}] \\ &= \mathbb{E}\left[\frac{1}{\mathbb{N}[\mathcal{S}_{5s}]} \sum_{k=1}^{\mathbb{N}[\mathcal{S}_{5s}]} I_{fs\to ap}^{(k)} \left(\mathtt{x}_{v,t}^{(k)}, \mathtt{x}_{v,r}^{(k)}, \mathtt{x}_{i,t} \right) \right]. \end{aligned} \tag{2.22}$$

Recalling the accuracy of uniform distribution when adopting an "average" interference, the interference analysis method that is provided in (2.20) might be questionable, based on the discussion provided in [60]. However, in this model, the 5G system adopts beamforming that utilizes very narrow beams and thus each 5G cell is sectorized. Such sectorization provides "angle" as an additional dimension in distribution of interference victim receivers (5G APs or UEs). This makes well distinguished distributions of (i) the interference victim receivers and (ii) the interfering transmitter, which leads to more accurate statistical analysis.

2.4.3 Evaluation of Interference

Similarly to the ES-to-AP interference study, we adopt I/N as our coexistence interference metric, which is defined according to the direction of interference as

$$(\mathrm{I/N})_{ap \text{ or } ue\to fs} = \bar{I}_{aggr}/N_{th,fs} \tag{2.23}$$

$$(\mathrm{I/N})_{fs\to ap \text{ or } ue} = \bar{I}_{avg}/N_{th,ap \text{ or } ue} \tag{2.24}$$

where $N_{th,(\cdot)}$ is the thermal noise power of a receiver device according to the system type.

As mentioned in Section 2.3, TH_{5g} of -6 and 0 dB are typically used for mobile terrestrial systems. An TH_{fs} of -10 dB was chosen for the FS as per [64].

Recall from (2.20) and (2.22) that the 5G-to-FS interference metric is aggregated whereas the FS-to-5G interference is averaged over $\mathbb{N}[\mathcal{S}_{5s}] = 57$ sectors in the 5G system. This is why 5G-to-FS interference is more significant, as observed in Figs. 2.10 through 2.13. It is shown in Figs. 2.10 and 2.11 that the 5G-to-FS interference is above the interference protection criterion of the FS, $TH_{fs} = -10$ dB of I/N, in many cases where the FS node is situated in the proximity of the 5G system. On the other hand, Figs. 2.12 and 2.13 show that the FS-to-5G interference is below the interference protection criterion of the 5G, $TH_{5g} = -6$ and 0 dB of I/N, in all cases of interest. Comparing both sets of figures, it is consistently observed that UMi yields lower interference than UMa, in both scenarios of 5G-to-FS and FS-to-5G interference. This is because UMi predicts a higher propagation loss which in turn leads to a lower interference signal power.

One interesting observation is that an *inflection point* is observed in the region of 2,000 to 4,000 m, in all of Figs. 2.10 through 2.13. To analyze this phenomenon, we consider a single AP and place it at the center of the 5G system (see Fig. 2.7 for the layout). We found two dominant factors contributing to the AP-to-FS interference: (i) the elevation antenna gain of the FS node, $G_{fs,e}(\theta_{fs,off})$, and (ii) the path loss from the AP to the FS as a function of distance, $PL_{5g\to fs}$. Fig. 2.14 shows the two factors separately, and the resulting I/N with the two factors combined. In Fig. 2.14a, around the region of 3,000 to 3,500 m, $G_{fs,e}(\theta_{fs,off})$ increases by 8.35 dB while $PL_{5g\to fs}$ drops by only 2.3 dB in Fig. 2.14b. Therefore, in Fig. 2.14c, the resulting I/N increases by 5.73 dB which causes an inflection point. We note that the elevation antenna gain curve is the result of the FS antenna beam pattern model adopted by the ITU [63]. Hence, the behavior of I/N is dependent on the specific properties of the FS node antenna pattern.

2.5 Mitigation of Interference from 5G into Fixed Service

As demonstrated in Section 2.4, in the coexistence between 5G and FS, the 5G-to-FS interference is more problematic due to aggregation of interference from multiple 5G sectors. This section proposes practical mechanisms to mitigate AP-to-FS and UE-to-FS interference. Although the proposed mechanisms refer to the system model and parameters discussed in Section 2.4, these mechanisms can be applied to any interference scenario where a 5G system adopting high-gain steerable directional antennas coexists with a terrestrial incumbent system.

The key idea of the proposed mitigation methods is to prohibit transmissions from 5G nodes

(APs or UEs) with transmit beams pointing at the victim FS receiver. In other words, the 5G transmitters are driven to point the beams away enough from the FS receiver so that they have sufficiently attenuated transmit gains toward the FS.

2.5.1 Mitigation of AP-to-FS Interference

Without loss of generality, let us consider beam restriction techniques on the azimuth plain. For an AP, $\phi_{ap,off}$ and $\phi_{ap,str}$ are recalled from Fig. 2.8 as an off-axis angle and a steering angle. Note that the antenna gain of an AP's beam attenuates as it (i) points further away from the FS receiver and (ii) gets further away from the sector's physical orientation. The victim FS receiver can undergo a lower interference if the transmit beam from an AP is sufficiently attenuated based on the two factors. To measure the two types of attenuation, we define the thresholds Φ_{off} and Φ_{str} that $\phi_{ap,off}$ and $\phi_{ap,str}$ must exceed, respectively. Fig. 2.15 illustrates the thresholds. If a beam is with $\phi_{ap,off} \leq \Phi_{off}$, it means that the beam points closer at the FS receiver than allowed. Similarly, if $\phi_{ap,str} \leq \Phi_{str}$, the beam is attenuated less than allowed by electrical steering.

Therefore, we shut down a beam if it does not meet $\phi_{ap,off} > \Phi_{off}$ and $\phi_{ap,str} > \Phi_{str}$ at the same time, which is formulated based on (2.4) as

$$G_{ap}\left(\phi_{ap,off}, \phi_{ap,str}\right) = \begin{cases} G_{ap}\left(\phi_{ap,off}, \phi_{ap,str}\right), & \phi_{ap,off} > \Phi_{off} \\ & \quad \text{and } \phi_{ap,str} > \Phi_{str} \\ 0, & \text{otherwise.} \end{cases} \tag{2.25}$$

Now, we can rewrite (3.3) to depict that an AP is the interfering transmitter and the FS is the victim receiver as

$$I_{ap\rightarrow fs}^{(k)} = \frac{P_{T,ap} G_{ap}\left(\phi_{ap,off}, \phi_{ap,str}\right) G_{fs}\left(\phi_v, \theta_v\right)}{PL_{ap\rightarrow fs}\left(\mathtt{x}_{ap}, \mathtt{x}_{fs}\right)} \tag{2.26}$$

where $P_{T,ap}$ denotes transmit power of an AP. Thus, an AP-to-FS interference aggregated over the $\mathbb{N}\left[\mathcal{S}_{5s}\right] = 57$ sectors is obtained by substituting (2.26) into (3.4), which now reflects the proposed interference mitigation method.

As mentioned in Section 2.2, this proposed method enables each AP to autonomously (without the need of an inter-system infrastructure) identify the beams that are to be avoided and perform the interference mitigation. The reason is that for the computation of Φ_{off}, the only information that an AP needs is location of the victim FS receiver. It can be learned from the license data registered to the FCC because all the FS devices in the 70 GHz band are required to register.

The proposed method is integrated into a realistic protocol that utilizes 5G interface as follows:

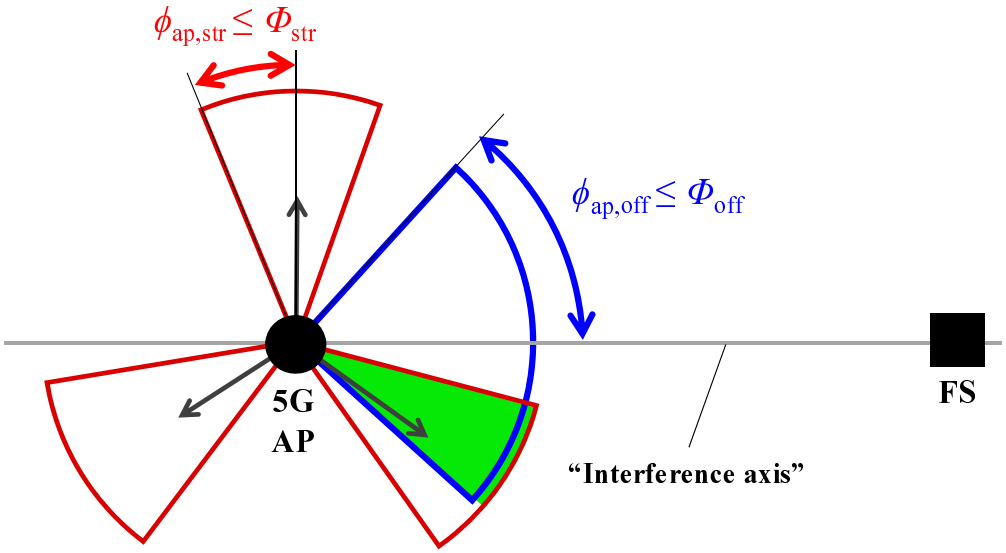

Figure 2.15: Definition of exclusion zone at a 5G AP

1. Define (a) beam exclusion zone(s) at each AP: Each AP constructs (an) exclusion zone(s), which is defined as an intersection (highlighted in light green in Fig. 2.15) of two fan-shaped areas that are formed by the following two inequalities: (i) $\phi_{ap,off} < \Phi_{off}$ and (ii) $\phi_{ap,str} < \Phi_{str}$.

2. Shut down the interfering beams: The interfering beams are identified as the beams in the exclusion zones. Downlink pilot transmissions corresponding to these beams are also shut down (or transmitted at reduced power levels) during the 5G beam scanning intervals. This enables 5G UEs to exclude such interfering beams during their initial beam attachment or periodic beam re-selection process. A UE requesting an attachment in an exclusion zone is handed over to another sector through a re-selection process.

2.5.2 Mitigation of UE-to-FS interference

The method of mitigating UE-to-FS interference is also a two-step process as follows:

1. Identify the interfering UE based on its uplink reference signal: The proposed UE-to-FS interference mitigation technique is similar to the AP-to-FS interference mitigation. It aims to reduce interference caused by UEs, based on identification of the specific beams causing unacceptable interference at the FS receiver. Hence it also refers to (2.26), but with the parameters for the UE.

However, the key problem with identification of the interfering UEs is that in general only

the AP is aware of which of its UEs are assigned to transmit during a certain uplink time slot. As a solution, this paper proposes a *probe-based* method where a 5G probe device is co-located with the victim FS receiver. The probe measures and reports its uplink Reference Signal Received Power (RSRP) measurements to the 5G system server. The probe device is frame-synchronized with the 5G system and may rely on the uplink 5G air-interface beam measurement procedures. Also, the antenna characteristics of the probe device should match those of the FS node (Table 2.6), which enables the probe to accurately track UE-generated interference as received by the FS node.

To enable interfering UE identification by the 5G system, it is proposed for the emerging 5G air interface to embed a cell-specific identification signal into the uplink Demodulation Reference Signal (DMRS). The cell-specific identification signal can take a form of a pseudo-noise (PN) sequence with a particular index of the sequence tied a particular 5G cell in which the uplink transmission was performed. Given the probe's RSRP report and the identity of the cell in which the interfering transmission has occurred, the 5G system can readily identify the interfering UE(s) by learning the particular frame and cell of the interfering transmission(s).

2. Hand over the interfering UEs to another sector: Given that the interfering UEs have been successfully detected and identified, the 5G system initiates a handover of the interfering UEs to another sector. Because of the highly directional transmit beams deployed by the 5G UEs on the uplink, simply handing over the interfering UEs will very likely change the direction of the UEs' transmit beams even if the UEs remains stationary. This change in the transmit beam direction will mitigate or even fully eliminate the interference observed at the FS node prior to the handover.

2.6 Evaluation of the Proposed Interference Mitigation Technique

We evaluate performance of the interference mitigation methods that are discussed in Section 3.4. The settings and parameters for the evaluation refer to Table 2.6 of Section 3.4.

2.6.1 Evaluation Method

We assess the proposed interference mitigation techniques in the following two aspects: (i) 5G-to-FS interference and (ii) impact on performance of the 5G system itself. Firstly, the improvement in the 5G-to-FS interference is calculated based on (2.23). Secondly, the application of the proposed AP and UE interference mitigation methods will invariably lead to performance degradation of the 5G system, since the AP interference mitigation technique restricts the selection of beams available for UE attachment on the downlink and forces

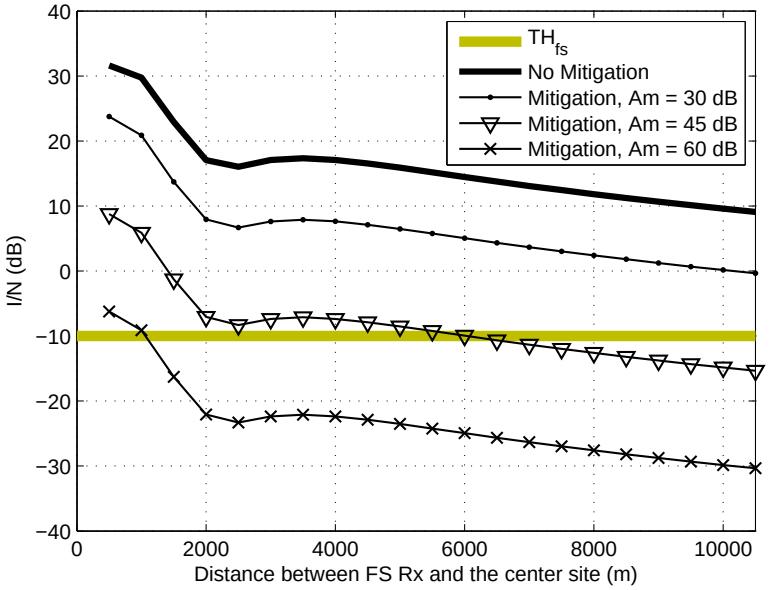

Figure 2.16: Mitigation of AP-to-FS interference

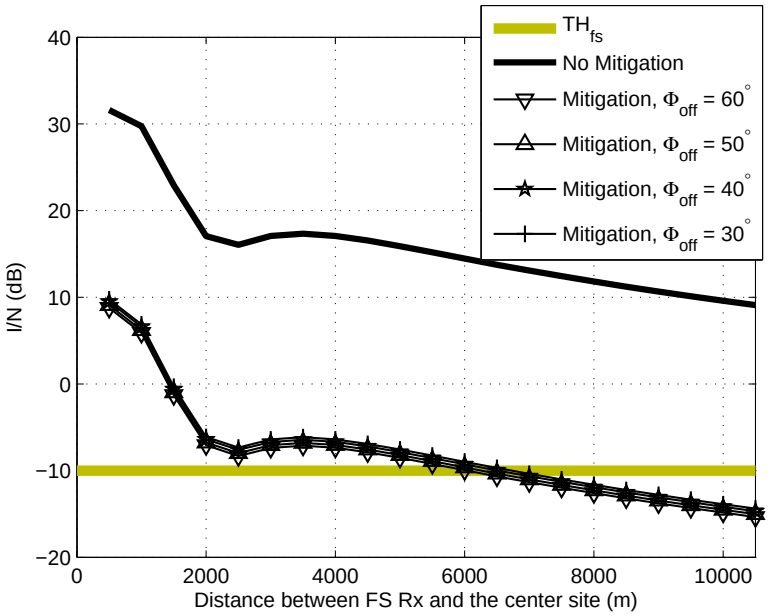

Figure 2.17: Reduction of Φ_{off} ($\Phi_{str} = 60°$, $A_m = 45$ dB)

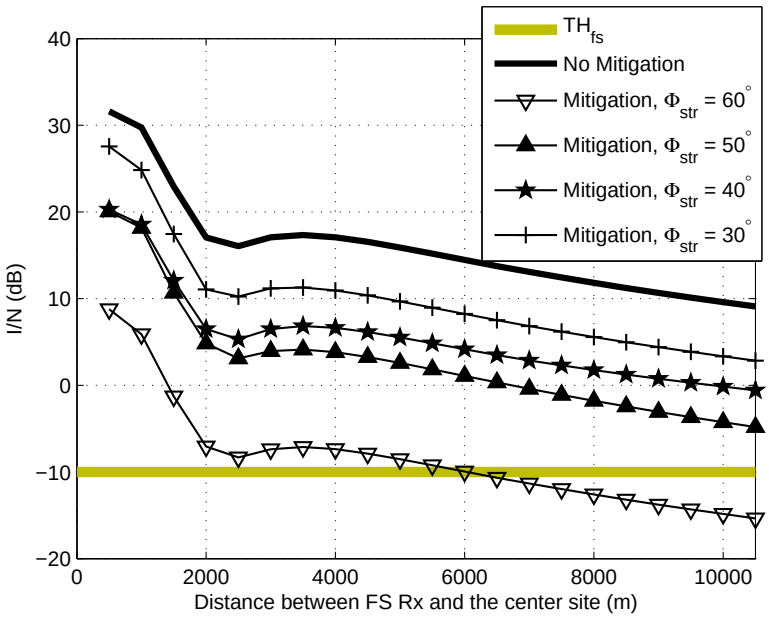

Figure 2.18: Reduction of Φ_{str} ($\Phi_{off} = 60°$, $A_m = 45$ dB)

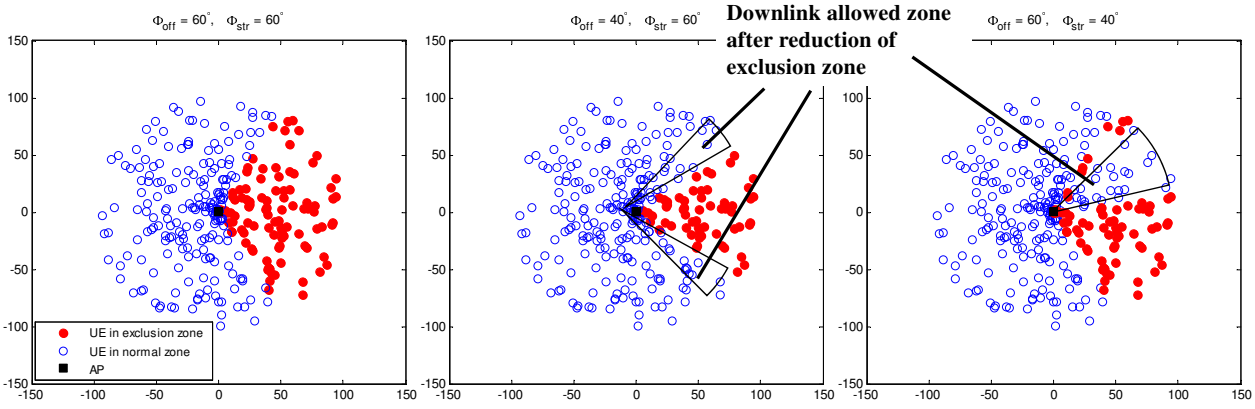

(a) $\Phi_{off} = 60°, \Phi_{str} = 60°$ (b) $\Phi_{off} = 40°, \Phi_{str} = 60°$ (c) $\Phi_{off} = 60°, \Phi_{str} = 40°$

Figure 2.19: Example of reduction of the thresholds, Φ_{off} and Φ_{str}

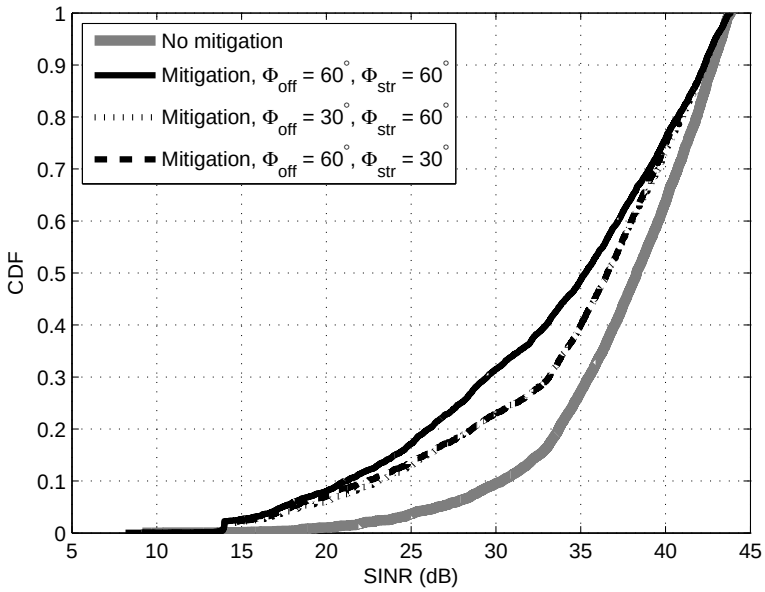

Figure 2.20: Impact of reducing Φ_{off} and Φ_{str} on the 5G downlink SINR

handover to a possibly suboptimum attachment point for the UE interference mitigation on the uplink. We characterize this performance degradation by computing downlink SINR and uplink SNR before and after applying the downlink and uplink interference mitigation techniques.

For the downlink, a signal-to-interference-plus-noise ratio (SINR) that is measured at a UE in the jth sector, $\mathcal{R}_j^2$, is calculated as

$$\text{SINR} = \frac{P_{R,ue}^{(j)} G_{ue} G_{ap}}{N_{th,ue} + \sum_{k \in \mathbb{N}[\mathcal{S}_{5s}], k \neq j} P_{R,ue}^{(k)}}. \tag{2.27}$$

where $P_{R,ue}^{(j)}$ denotes the signal power that the UE receives from the jth sector's antenna. Note that this SINR does not include the interference from the FS; referring to Fig. 2.12, the FS-to-AP interference is insignificant compared to the noise level observed at the UEs.

For the uplink, a signal-to-noise ratio (SNR) at an AP is obtained as

$$\text{SNR} = \frac{P_{R,ap}^{(j)} G_{ap} G_{ue}}{N_{th,ap}}. \tag{2.28}$$

where $P_{R,ap}^{(j)}$ denotes a signal power received at the jth sector. Similarly, the FS-to-UE interference is excluded since it has little impact on the SNR as observed from Fig. 2.13. As a further simplification, we note that the uplink performance is noise-limited due to lower UE transmit powers and also exclude inter-cell interference from calculation of the uplink SNR.

2.6.2 AP-to-FS Interference Mitigation

Fig. 2.16 shows the impact of the proposed interference mitigation technique on the AP-to-FS interference. Note that the decrease in AP-to-FS interference follows the corresponding increase in sector antenna's front-to-back ratio, A_m; this is especially pronounced in the region of AP-to-FS distance of 2,000 m or more. That is, a 15 dB increase in A_m roughly results in a 15 dB decrease in I/N. This effect demonstrates that the dominant interfering beams in the sectors that are pointed directly at the FS node have been suppressed and the interference is now largely dependent on the power received from the sectors that are pointed away from the FS node.

As the performance of the 5G system can be adversely affected by the size of a beam exclusion zone, here we explore the sensitivity of the resulting I/N at the FS node to the size of the exclusion zone at an AP. Reduction of exclusion zone can be achieved by reduction of either Φ_{off} or Φ_{str}, defined above in Fig. 2.15. Impacts of reduction of the two thresholds are shown in Figs. 2.17 and 2.18. Reducing the exclusion zone according to Φ_{off} does not result in a significant increase in AP-to-FS interference, as shown in Fig. 2.17. On the other hand, Fig. 2.18 shows that reduction of exclusion zone according to Φ_{str} significantly increases AP-to-FS interference.

The reason for this behavior is explained in Fig. 2.19. Each subfigure shows a cumulative snapshot of 10 drops with 10 UEs dropped per sector. For consistency with the topology shown in Fig. 2.15, the victim FS node is fixed at $(x, y) = (500, 0)$ which is on the right side of the cell; thus the interference axis is defined as a horizontal line passing through the AP at $(0, 0)$ in each subfigure. The red dots represent the UEs in the exclusion zone, while the blue ones indicate those outside of the zone where downlink transmissions are allowed. Let us begin with the case of $\Phi_{off} = 60°, \Phi_{str} = 60°$ that is given in Fig. 2.19a. The cases where the thresholds Φ_{off} and Φ_{str} are reduced are presented in Figs. 2.19b and 2.19c, respectively. In Fig.2.19b, reduction of Φ_{off} opens up a beam transmission area that is further away from the interference axis, which does not translate into increased interference at the FS node. On the other hand, in Figs. 2.19c, reduction of ϕ_{str} opens up an area with interfering beam transmissions that is closer to the interference axis, resulting in significant interference increase at the FS node.

We further note that reducing either of the two thresholds results in a similar level of improvement in SINR for the 5G downlink which is given in (2.27). Fig. 2.20 displays a CDF of the downlink SINRs with no interference mitigation and three different Φ_{off} and Φ_{str} settings. The figure shows that reduction of either Φ_{off} or Φ_{str} improves the SINRs since both of these thresholds about equally reduce the beam exclusion zone at each AP. This is also evident in Figs. 2.19b and 2.19c, where the sizes of the exclusion zones (areas with red dots) are roughly equal after reduction. As a consequence, it is much more efficient to adjust Φ_{off} for controlling the size of the exclusion zone, while keeping Φ_{str} fixed, since adjusting Φ_{off} yields a similar level of downlink SINR improvement but without increasing the AP-to-FS interference.

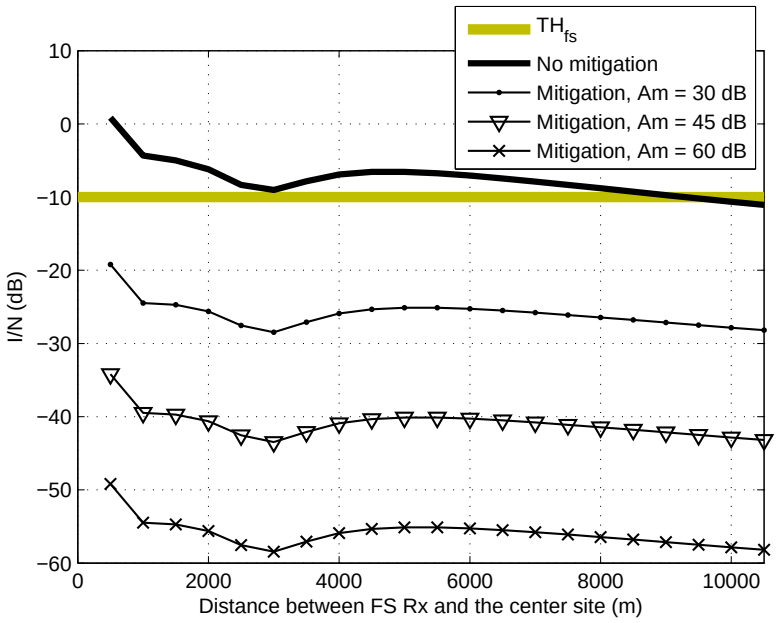

Figure 2.21: Mitigation of UE-to-FS interference

2.6.3 UE-to-FS Interference Mitigation

Fig. 2.21 evaluates the UE-to-FS interference with application of the proposed mitigation technique. Similar to the trend observed in Fig. 2.16, the change in residual interference level observed at the FS node roughly follows the change in the UEs' antenna front-to-back ratio, A_m. We again conclude that the proposed mitigation technique on the UE side is effective in suppression of the beams pointed directly at the FS node, as it is observed that the residual interference becomes a function of the energy received from the back side of a UE's antenna.

Fig. 2.22 presents the impact of the UE-to-FS interference mitigation technique on the uplink 5G system performance. Maximum degradation observed with this mitigation technique is approximately 15 dB, which is due to forcing the interfering UEs to re-attach to a sector that provides a sub-optimum uplink signal strength.

2.6.4 Discussion on Performance of 5G

In general, 5G systems will be expected to provide a high degree of coverage and reliability even in the most severe propagation environments. In [18], typical values of SINR for uplink and downlink at mmW frequencies are displayed. According to the results in [18], SINRs

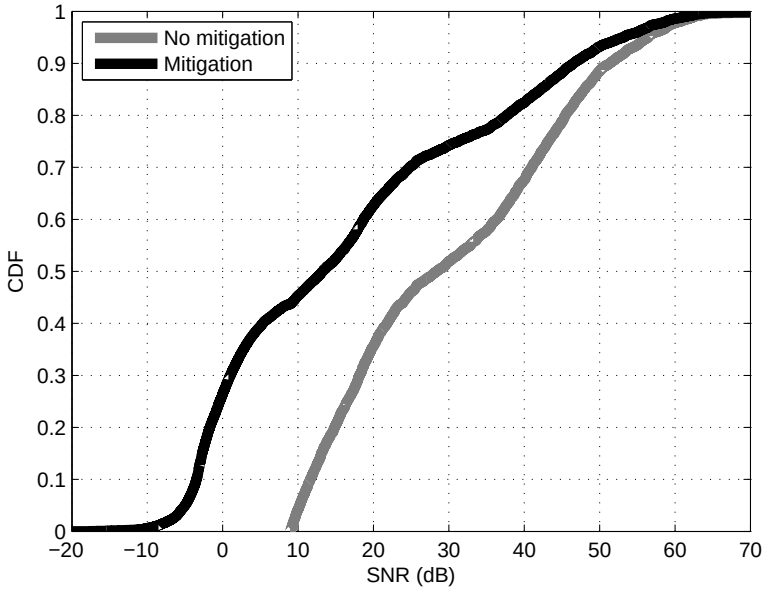

Figure 2.22: Impact of UE-to-FS interference mitigation on 5G uplink performance

as low as -10 dB could be observed at these frequencies in challenging propagation conditions, and 5G systems are expected to remain fully operational even in these very low SINR conditions.

From Figs. 2.20 and 2.22, one can see that the "worst-case" downlink SINR and uplink SNR of a 5G system adopting the proposed interference mitigation techniques are also in the range of -10 dB. Thus, we conclude that despite some degradation in both downlink and uplink due to incumbent interference mitigation, the performance of a 5G system will remain acceptable.

2.7 Chapter Summary

This paper performed a detailed analysis of coexistence scenarios for 5G in mmW bands, namely co-channel coexistence of 5G with FSS uplink at 28 GHz and with FS WB at 70 GHz. The first part of our 28 GHz study discussed the AP-to-SS and UE-to-SS interference. We showed that 5G can satisfy interference protection criteria of the FSS while allowing simultaneous transmissions from at least several thousands of sectors and tens of thousands of UEs under various LoS and NLoS channel conditions and with various sets of parameters for the FSS. In the analysis of ES-to-AP interference, we characterized the separation distances

in order to guarantee that higher than 95% of uplink transmissions in the nearest cell are protected. The required separation distances are not overly restrictive for deployment of 5G systems, and our results further validate that the 28 GHz band is viable for future 5G system deployments. In the 70 GHz study, we demonstrated that the 5G-to-FS interference is more significant than the FS-to-5G interference, due to aggregation of interference among all of the sectors. Motivated by this observation, we proposed the mechanisms that mitigate the interference from APs and UEs into the FS system. Our results showed that the proposed techniques can effectively suppress the interference at the FS receiver while maintaining operable performance of 5G.

Chapter 3

Communications-Radar Coexistence at 3.5 GHz: Part 1

This chapter discusses coexistence of Wi-Fi that is deployed outdoor with pulsed radar for spectrum sharing in the 3.5 GHz band. Note that the 3.5 GHz coexistence problem is discussed in two different chapters–Chapters 3 and 4. This chapter takes a geometric approach similar as in Chapter 2, in order to characterize separation distances between outdoor Wi-Fi and radar based on the interference toleration requirements of the two systems. Whereas Chapter 4 focuses on a signal processing aspect that can be applied to general wireless mobile communications systems adopting OFDM.

This chapter suggests a novel method that addresses the interference from the outdoor Wi-Fi to the radar at 3.5 GHz. While most of prior work is only interested in reduction of such interference by restricting Wi-Fi's operation, we propose a technique that mitigates such interference while maintaining the performance of Wi-Fi. We provide a framework for analyzing the coexistence between the two systems based on the stochastic geometry. In addition, we provide an accurate characterization of the Wi-Fi systems' behavior, by taking into account the two popular types of multiple access schemes: normal carrier-sensing multiple access (CSMA) and Enhanced Distributed Channel Access (EDCA).

3.1 Related Work

Since the United States Federal Communications Commission (FCC) released new rules for shared use of the 3.5 GHz band [14], IEEE 802.11 WG has been objecting to the decision that exclusion zones must exist for protecting federal radars, since Wi-Fi cannot bring enough benefit without serving users living in the coastal areas where a large population of this nation resides [7]. This communication-radar coexistence was discussed in some recent literature

[21]-[26]. More recent work proposed interference reduction techniques [41]-[44].

While little work exists beyond the prior work above, in this chapter our work proposes a WtR interference mitigation technique, assuming that the Wi-Fi is deployed *outdoors* and thus adopts *directional antennas*. The growing demand for affordable mobile broadband connectivity is driving the development of Heterogeneous Networks (HetNets) where macro cells will be complemented by a multitude of small cells, which will require broader deployment of outdoor Wi-Fi [65]. The outdoor deployment is expected to be the major source of WtR interference because it uses higher transmit power and antenna gain due to directional antennas for connecting cells and networks.

3.2 Main Contributions

The contributions of this chapter are as follows:

- It characterizes coexistence of radar with Wi-Fi, rather than the Long-Term Evolution (LTE) as in [43]-[44]. This chapter will serve a critical need in the 3.5 GHz band coexistence: *reduction of the exclusion zone*. Moreover, Wi-Fi is more complicated to model because the TX is randomly selected between an access point (AP) and a normal station (STA), whereas transmission of base stations and user equipments are strictly divided in LTE.
- It proposes a method that mitigates WtR interference. Our work is distinguished from [42]-[44] since it (i) requires no Wi-Fi network to stop transmission during an interference suppression period and (ii) maintains acceptable Wi-Fi performance while suppressing WtR interference.
- It proposes a comprehensive protocol that enables to (i) acquire the location and (ii) piggyback the location report on the channel sounding, based on the up-to-date 3.5 GHz rules. This distinguishes this chapter from [42] that unrealistically assumed perfect synchronization between the radar and the Wi-Fi.

3.3 Analysis of Interference

In this section, we provide an analysis framework for WtR and radar-to-Wi-Fi (RtW) interference.

Table 3.1: Summary of Key Notation

Notation	Description
$\mathtt{x} = (x, y)$	Position of a node
λ	Density (the number of points) of a PPP
θ_w, θ_r	*Off-axis angles* of a Wi-Fi node and the radar, respectively (See Fig. 3.1)
Θ	Threshold that limits a θ_w in the proposed method
$\mathcal{S}_{\theta_w}, \mathcal{S}_p$	Sets of Wi-Fi nodes sorted in θ_w and the priority, respectively

3.3.1 System Model

Geometry

One radar is placed at the origin of the quadrant, $\mathcal{O} = (0, 0)$. The radar beam rotates with a revolution rate of ρ rotations per minute (rpm). The distance between the radar and the center of a "Wi-Fi region" is denoted by d. A *Wi-Fi network* is composed of one "fixed" AP with multiple STAs attached to the AP. A *Wi-Fi region* refers to a region with multiple Wi-Fi networks. In a geometry given in Fig. 3.1, a Wi-Fi region is denoted by $\mathbf{R}^2_{reg}$ and a Wi-Fi network is denoted by $\mathbf{R}^2_{net}$. Distribution of $\lambda_{ap}\,(>0)$ Wi-Fi APs in a $\mathbf{R}^2_{reg}$ follows a Poisson Point Process (PPP): $\mathtt{x}_{ap} = (x_{ap}, y_{ap}) \in \mathbf{R}^2_{reg}$. Then, a Wi-Fi network is formed around each AP, which is expressed as $\left|\mathbf{R}^2_{net,k}\right| = |\mathtt{x}_{ap} - \mathtt{x}_{sta}| \leq r_{net}$ where $\mathbf{R}^2_{net,k}$ is the kth Wi-Fi region in a $\mathbf{R}^2_{reg}$ and r_{net} is the radius of a $\mathbf{R}^2_{net,k}$ and it is kept constant among different $\mathbf{R}^2_{net,k}$'s. Note that an $\mathbf{R}^2_{net,k}$ is circular although an AP antenna uses beamforming, since it represents a geometry that an AP can serve. Distribution of $\lambda_{sta}\,(>0)$ STAs is represented as another PPP: $\mathtt{x}_{sta} = (x_{sta}, y_{sta}) \in \mathbf{R}^2_{net}$. As such λ_{sta} and λ_{ap} are regarded as the *densities* of the PPPs that are defined in $\mathbf{R}^2_{net,k}$ and $\mathbf{R}^2_{reg}$, respectively. Note that $\mathtt{x}_{sta}$ and $\mathtt{x}_{ap}$ are homogeneous point processes where λ_{sta} and λ_{ap} are constant in different $\mathbf{R}^2_{net,k}$'s and $\mathbf{R}^2_{reg}$'s, respectively. Therefore $\mathtt{x}_{sta}$ and $\mathtt{x}_{ap}$ are distributed uniformly on X and Y axes on a quadrant [143].

We assume that antennas of the Wi-Fi TX and receiver (RX), and the radar are at the same height, which excludes the elevation plane from consideration. This assumption is reasonable because coexistence likely occurs along the coast, where the Wi-Fi networks are deployed at almost the same height from the sea level. Now, on the azimuth plane, an *interference axis* is defined as the line connecting an interferer TX and a victim RX. Since both the radar and the Wi-Fi use directional antennas, an interference level is dominantly determined by an angle of a beam relative to an interference axis, namely an *off-axis angle*. As in Fig. 3.1, θ_w and θ_r denote off-axis angles of a Wi-Fi TX and the radar, respectively.

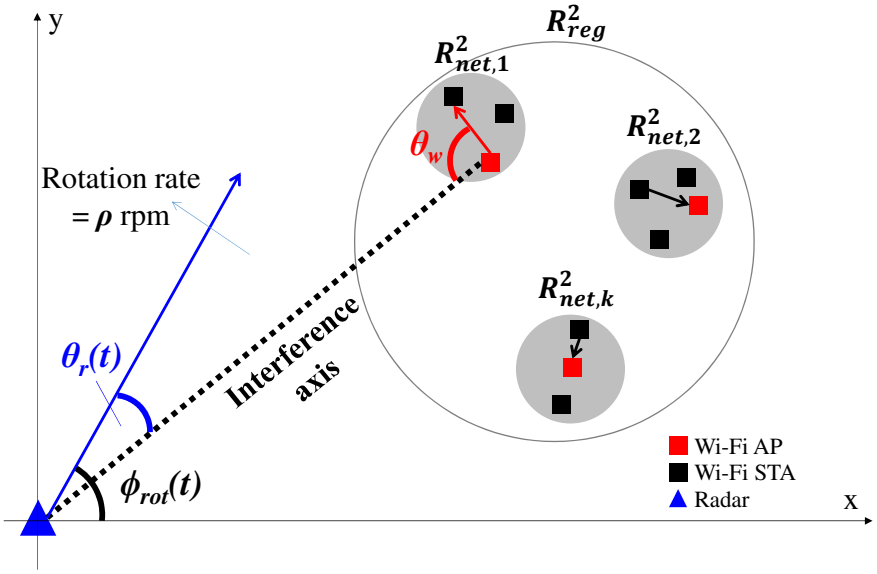

Figure 3.1: Geometry of a radar-Wi-Fi coexistence

Antenna Beam Patterns

The antenna gain for the radar is based on a *high-gain antenna model* [67] with $22 < G_{max} = 33.5 < 48$ dBi where G_{max} is a maximum antenna gain and the value of 33.5 dBi comes from a relevant benchmark [26].

For the Wi-Fi's radiation pattern, we adopt the general *linear array* which is given by [68]

$$G(\theta) = G_{max} - \exp(-2\pi\jmath\delta\sin\theta) \tag{3.1}$$

where δ denotes the antenna element separation distance that is half a wavelength, and θ denotes an azimuth angle. A Wi-Fi antenna (for both the AP and the STA) is composed of 4 elements that are placed horizontally linearly. The maximum antenna gain for an element is 2.15 dBi, which results in $G_{max} = 2.15 + 10\log_{10} 4 \approx 8.17$ dBi.

Multiple Access in Wi-Fi

In a Wi-Fi network, the AP and STAs compete for the medium in two different manners, enhanced distributed channel access (EDCA) and normal carrier-sense multiple access (CSMA), respectively. This chapter approximates a scheme where a priority value ranges $0 \leq \mathtt{p} \leq 7$ as in EDCA. Reflecting recent practical Wi-Fi environments where an AP requires more chance of transmission, the priorities are ranged in $4 \leq \mathtt{p} \leq 7$ for an AP and in $0 \leq \mathtt{p} \leq 7$ for a STA. The priority values are uniformly randomly distributed within a range. Note

that although there is prior work thoroughly characterizing EDCA, the focus of this chapter is the proposition of a new technique for mitigating WtR interference. As such it proposes a metric that reasonably approximates the performance of a Wi-Fi network, reflecting the difference between EDCA and normal CSMA. The metric is called *normalized priority-based performance indicator (*`NPPI`*)* which is given by

$$\texttt{NPPI} = \begin{cases} \texttt{SINR} * (\texttt{p}+1)/8, & \text{EDCA} \\ \texttt{SINR}, & \text{Normal CSMA} \end{cases} \tag{3.2}$$

where signal-to-interference-plus-noise ratio (`SINR`) at a Wi-Fi RX shall be discussed in (3.7). In the normal CSMA, the AP and the STAs within a network has equal chance of transmission.

3.3.2 Interference Calculation

Wi-Fi-to-Radar (WtR) Interference

Based on the geometry shown in Fig. 3.1, we can formulate an interference power that is received at a radar location in $\mathbf{R}^2_{reg}$ from an "individual" Wi-Fi TX at a time instant, t, which is given by

$$I\left(\mathtt{x}_{ap}, \mathtt{x}_{sta}, t\right) = l\left(\|\overrightarrow{\mathcal{OQ}}\|\right) P_T G_T\left(\theta_w\right) G_R\left(\theta_r\left(t\right)\right) \tag{3.3}$$

where G_T and G_R denote TX and RX antenna gains corresponding a Wi-Fi TX and the radar in this case, respectively. Also, $l\left(\cdot\right) = 259\|\overrightarrow{\mathcal{OQ}}\|^{-3.97}$ is a path loss [26] between the origin of the quadrant $\mathcal{O}$ (location of the radar) and a point $\mathcal{Q} = \mathtt{x}_{ap}$ or $\mathtt{x}_{sta}$. Note that (3.3) is a function of $\mathtt{x}_{ap}$, $\mathtt{x}_{sta}$, and t because they determine θ_w and θ_r. With an AP as an example as depicted in Fig. 3.1, $\theta_w = \cos^{-1}\frac{\overrightarrow{\mathtt{x}_{ap}\mathtt{x}_{sta}}\cdot\overrightarrow{\mathtt{x}_{ap}\mathcal{O}}}{\|\overrightarrow{\mathtt{x}_{ap}\mathtt{x}_{sta}}\|\|\overrightarrow{\mathtt{x}_{ap}\mathcal{O}}\|}$ and $\theta_r\left(t\right) = \cos^{-1}\frac{\overrightarrow{\mathcal{O}\mathtt{x}_{ap}}\cdot\overrightarrow{\mathcal{OO'}}}{\|\overrightarrow{\mathcal{O}\mathtt{x}_{ap}}\|\|\overrightarrow{\mathcal{OO'}}\|}$ where $\mathcal{O}'$ is a reference point to indicate the radar beam's direction. Note that it is given by $\mathcal{O}' = \left(d\cos\phi_{rot}\left(t\right), d\sin\phi_{rot}\left(t\right)\right)$. A radar beam rotation angle, $\phi_{rot}\left(t\right)$, is a function of time and is given by $\phi_{rot}\left(t\right) = \frac{2\pi\rho}{60}t$ where ρ is recalled to be a revolution rate (the number of rotations per minute) of a radar, and t is a time instant measured in seconds. Note that P_T is differentiated according to whether the Wi-Fi TX being an AP or a STA. The probability that an AP or a STA becomes TX depends on the multiple access schemes, EDCA or normal CSMA.

It is very important to note that a WtR interference is composed of an *aggregate* signal power received by multiple Wi-Fi TXs simultaneously. From (3.3), an aggregate interference that is received by a radar located at $\mathcal{O}$ from all of the Wi-Fi networks in $\mathbf{R}^2_{reg}$ at a time instant t can be formulated as

$$I_{wtr}\left(\mathtt{x}_{ap}, \mathtt{x}_{sta}, t\right) = P_T \sum_{\mathtt{x}_{ap}\in\mathbf{R}^2_{reg}} l\left(\|\overrightarrow{\mathcal{OQ}}\|\right) G_T\left(\theta_w\right) G_R\left(\theta_r\left(t\right)\right). \tag{3.4}$$

For a PPP of density λ, Campbell's theorem [51] offers a way to calculate a mean of a sum of an arbitrary real-valued function $h(\cdot)$ over a point process $\mathcal{S}$ on a d-dimensional region $\mathbf{R}^d$ is given by $\mathbb{E}\left[\sum_{u\in\mathcal{S}} h(u)\right] = \lambda \int_{\mathbf{R}^d} h(u)\, du$.

Note that a radar's operation must be completely protected since it serves the national security, which requires theoretically "zero" possibility of violation of the RtW interference threshold (set to -10 dB). Hence, we identify the *maximum interference power* during a radar's rotation that is averaged over all possible $\mathtt{x}_{ap}$ and $\mathtt{x}_{sta}$. The formal definition of a radar rotation time is $t_n \le t \le t_{n+1}$ where t_n is the time at which the nth rotation is completed and thus $t_{n+1} - t_n$ represents a rotation time. This leads to a *mean maximum aggregate interference (*`MMAI`*)* as

$$\begin{aligned}&\mathbb{E}\left[\max_t \left[I_{wtr}\left(\mathtt{x}_{ap}, \mathtt{x}_{sta}, t\right)\right]\right]_{\mathtt{x}_{ap},\mathtt{x}_{sta}} \\ &= \lambda_{ap}\lambda_{sta} P_T \int_{\mathtt{x}_{ap}\in\mathbf{R}^2_{reg}} \int_{\mathtt{x}_{sta}\in\mathbf{R}^2_{net}} l\left(\|\overrightarrow{\mathcal{O}Q}\|\right) G_T\left(\theta_w\right) G_R\left(\theta_r\left(t_0\right)\right) d\mathtt{x}_{sta} d\mathtt{x}_{ap}, \quad t_n \le t \le t_{n+1}\end{aligned} \tag{3.5}$$

where $t_0 = \arg\max_t I_{wtr}\left(\mathtt{x}_{ap}, \mathtt{x}_{sta}, t\right),\ t_n \le t \le t_{n+1}$.

Radar-to-Wi-Fi (RtW) Interference

A RtW interference is defined as an *average* radar signal power received by all the Wi-Fi RXs from the radar within its one rotation time. Changing (3.3) to indicate that the radar is the interfering TX and a Wi-Fi node is the victim RX, a RtW interference can be formulated as

$$\begin{aligned}I_{rtw}\left(\mathtt{x}_{ap}, \mathtt{x}_{sta}, t\right) &= \frac{1}{\lambda_{ap}} \sum_{\mathtt{x}_{ap}\in\mathbf{R}^2_{reg}} I\left(\mathtt{x}_{ap}, \mathtt{x}_{sta}, t\right) \\ &= \frac{P_T}{\lambda_{ap}} \sum_{\mathtt{x}_{ap}\in\mathbf{R}^2_{reg}} l\left(\|\overrightarrow{\mathcal{O}Q}\|\right) G_T\left(\theta_r\left(t\right)\right) G_R\left(\theta_w\right).\end{aligned} \tag{3.6}$$

Now performance of a Wi-Fi RX is

$$\mathtt{SINR}\left(\mathtt{x}_{ap}, \mathtt{x}_{sta}, t\right) = \frac{P_T G_T G_R l_w\left(\|\overrightarrow{\mathtt{x}_{ap}\mathtt{x}_{sta}}\|\right)}{I_{rtw}\left(\mathtt{x}_{ap}, \mathtt{x}_{sta}, t\right) + N_0} \tag{3.7}$$

where $l_w(\cdot)$ is the 3rd Generation Partnership Project (3GPP) Urban Micro (UMi) path loss model for a small cell environment [69]. Note that this `SINR` is used to finally obtain (3.2).

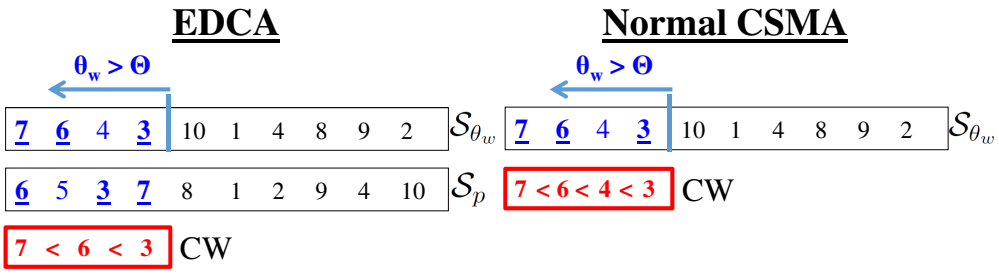

Figure 3.2: Example of the proposed mechanism ($\lambda_{sta} = 10$)

3.4 WtR Interference Mitigation

In this section, we propose a WtR interference mitigation method. Distinguished from [41]-[44], it enables every Wi-Fi network to keep operation, with the nodes with its beams sufficiently *off from the interference axis*; that is, $\theta_w > \Theta$ where Θ is the threshold of θ_w. The unnecessity of ceasing operation by any Wi-Fi network is the key benefit that this method introduces and thus keeps the Wi-Fi performance at an operable level.

3.4.1 Radar Sweep Period, T_{sweep}

A radar beam faces a Wi-Fi region for only a proportion of time within a rotation. We divide a rotation time into "sweep" and "safe" periods, denoted by T_{sweep} and T_{safe}, respectively. During a T_{safe}, no interference mitigation is needed and thus the Wi-Fi TXs can access the medium as described in Section 3.3.1. On the other hand, for a T_{sweep}, only the Wi-Fi TXs with $\theta_w > \Theta$ are eligible for competition for the medium.

A T_{sweep} is measured and periodically broadcasted to the Wi-Fi APs by the spectrum access system (SAS), the database mediating the radar and the communications system [14]. In turn, an AP updates T_{sweep} and broadcasts to the network using a beacon. For accurate measurement, a SAS sensor is almost co-located at the Wi-Fi networks so that a T_{sweep} is evaluated approximately the same for the Wi-Fi nodes. At every transition from a T_{safe} to T_{sweep}, there is a mitigation time, τ. If a packet to be transmitted is shorter than τ, the node is *eligible* to participate in a competition for the medium; otherwise, the node must add T_{sweep} to its backoff time.

3.4.2 Wi-Fi Off-axis Angle, θ_w

Each Wi-Fi node (AP or STA) is able to compute θ_w autonomously, based on (i) *location of the radar* provided via the SAS and (ii) its own position measured on its own. Whereas

the location measurement method is beyond the scope of this dissertation, the assumption remains reasonable based on prior methods such as [70].

However, it is necessary to analyze the impacts of the inaccuracy on the radar performance. For instance, an inaccurate localization can lead a Wi-Fi node with a smaller θ_w to be chosen for transmission. It results in a higher WtR interference occurs than it should be, which consequently incurs a lower radar performance. Also, the Wi-Fi performance can be affected when the opposite is the case. A Wi-Fi TX with a large enough θ_w and a high priority can be excluded from transmission due to an inaccurate localization. This will incur performance degradation in Wi-Fi.

3.4.3 Wi-Fi Protocol for WtR Interference Mitigation

Assuming accurate localization of Wi-Fi nodes, we propose a hybrid coordination function (HCF) where a distributed coordination function (DCF) during a T_{safe} and a point coordination function (PCF) during a T_{sweep}. For the EDCA, the eligible nodes are selected in the following manner. $\mathcal{S}_p$ and $\mathcal{S}_{\theta_w}$ are sets of indexes of the nodes in a network that are sorted in descending order in terms of priority and off-axis angle θ_w, respectively, where $\mathbb{N}[\mathcal{S}_p] = \mathbb{N}[\mathcal{S}_{\theta_w}] = \lambda_{sta}$. Suppose that the first m nodes of $\mathcal{S}_{\theta_w}$ meet the criterion $\theta_w > \Theta$. Then take the first m nodes from $\mathcal{S}_p$ as well, and obtain the node indexes that belong to the m-element subsets of both sets. Fig. 3.2 describes an example of this mechanism. Applying the off-axis angle criterion $\theta_w > \Theta$, nodes $\{6, 5, 3, 7\}$ remain in $\mathcal{S}_p$ and $\{7, 6, 4, 3\}$ remain in $\mathcal{S}_{\theta_w}$. Prioritizing $\mathcal{S}_{\theta_w}$ over $\mathcal{S}_p$, the intersection is sorted as $7 < 6 < 3$ and allocated smaller values of CW in that order. Note from Fig. 3.2 that *as* Θ *increases,* $\mathbb{N}[\mathcal{S}_{\theta_w}]$ *decreases and thus the intersection gets smaller as an immediate consequence.* For the normal CSMA, since no $\mathcal{S}_p$ is defined, nodes $\{7, 6, 4, 3\}$ are eligible and CW values are allocated in the order of $7 < 6 < 4 < 3$.

A STA exploits a channel sounding event to report its location to the AP. Although channel sounding sacrifices throughput due to overhead, this protocol adopts an obligatory reporting policy as in the Dynamic Frequency Selection (DFS) of IEEE 802.11h, considering the significance of the radar operation. Our protocol suggests that every STA reports its location at least once within a radar "revolution" time.

3.5 Numerical Results

In this study, we distribute Wi-Fi networks in a region with area of $\left|\mathcal{R}^2_{reg}\right| \approx 3.14$ km^2. The area of each Wi-Fi network is $|\mathcal{R}^2_{net}| \approx 0.04$ km^2. We run 10,000 "drops" in MATLAB with the parameters that are summarized in Table 3.2.

In Fig. 3.3, we show that the proposed method leads to reduction of separation distance.

Table 3.2: Parameters

Parameter	**Wi-Fi**	**Radar**
Carrier frequency	3.5 GHz	
Bandwidth	20 MHz	10 MHz
TX power	30 dBm (AP), 10 dBm (STA)	90 dBm
Max antenna gain	2.15 dBi per element, 4×4 array ($\lambda/2$ array)	33.5 dBi
Noise power (dBm)	-100.99 dBm	-104 dBm

We use interference-to-noise ratio (INR) to examine the separation distance where `MMAI` in (3.5) is used for the "interference." Normal CSMA yields lower INR as it incurs lower probability that an AP wins the medium, whereas EDCA yields higher WtR interference due to higher probability of AP transmission. With the mitigation technique, the interference gap between EDCA and normal CSMA decreases since the mitigation techniques forces a network to consider the off-axis angles before the priority.

In Fig. 3.4, we show a cumulative distribution function (CDF) of `NPPI` derived in (3.2) according to type of access and whether the interference mitigation method is applied. The interference mitigation method yields at maximum 15-dB `NPPI` degradation mainly due to (i) higher RtW interference and (ii) less chance of priority-based TX selection. The higher RtW interference under the mitigation mode is due to the fact that by having a TX not facing the radar, a RX points its RX beam at the radar with a smaller θ_w. The EDCA yields higher `NPPI` as it guarantees higher values of priority of the Wi-Fi TXs.

In Fig. 3.5, we compare the WtR interference according to the off-axis angle threshold Θ, with the EDCA. It is interesting that (i) variation of Θ has only little impact on WtR interference and (ii) the INR is in the order of $90° > 30° > 180°$. The same tendency is shown in the `NPPI` that is given in Fig. 3.6 as well. We discover that the WtR interference is a concave function according to Θ, in which $\Theta = 90°$ yields the maximum. As $\Theta = 0 \rightarrow 90°$, the intersection between $\mathcal{S}_p$ and $\mathcal{S}_{\theta_w}$ becomes smaller as $\mathbb{N}[\mathcal{S}_{\theta_w}]$ set becomes smaller. Now the priority becomes the dominant criterion in selection of the TX. As a result, it is more probable that an AP becomes the TX. Therefore, (i) WtR interference increases due to higher interfering TX power, and (ii) `NPPI` increases by being more dominated by the priority. As $\Theta = 90 \rightarrow 180°$, now it is very probable that no intersection exists between $\mathcal{S}_p$ and $\mathcal{S}_{\theta_w}$; hence, a TX is chosen in terms of θ_w only. As a result, (i) WtR interference decreases by having greater θ_w's, and (ii) `NPPI` decreases due to lower probability that an AP transmits.

3.6 Chapter Summary

This chapter proposed a technique that mitigates WtR interference while maintaining Wi-Fi system operation. It suggested a novel method that addresses the interference from the outdoor Wi-Fi to the radar at 3.5 GHz. While most of prior work is only interested in reduction of such interference by restricting Wi-Fi's operation, we proposed a technique that mitigates such interference while maintaining the performance of Wi-Fi. We provided a framework for analyzing the coexistence between the two systems based on the stochastic geometry. In addition, we provided an accurate characterization of the Wi-Fi systems' behavior, by taking into account the two popular types of multiple access schemes: normal CSMA and EDCA.

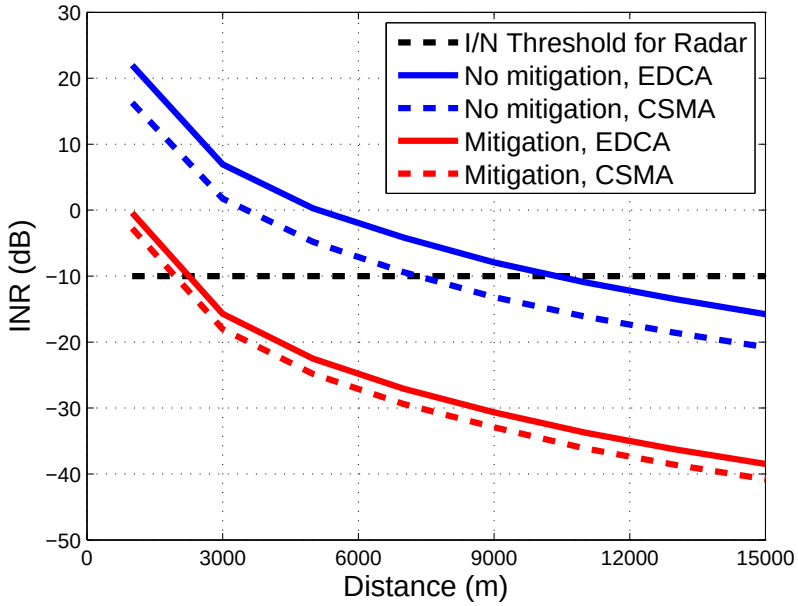

Figure 3.3: `MMAI` vs. d ($\lambda_{ap} = 100, \lambda_{sta} = 10$)

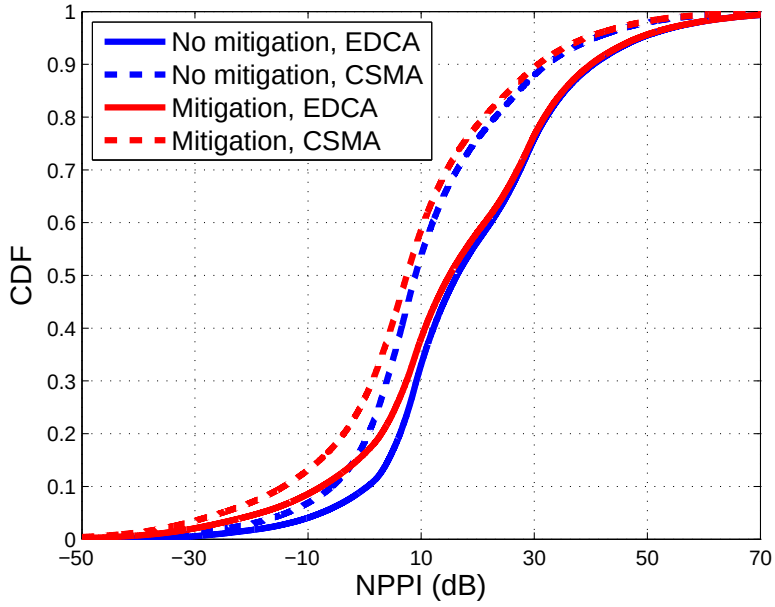

Figure 3.4: CDF of `NPPI` ($\lambda_{ap} = 100, \lambda_{sta} = 10$)

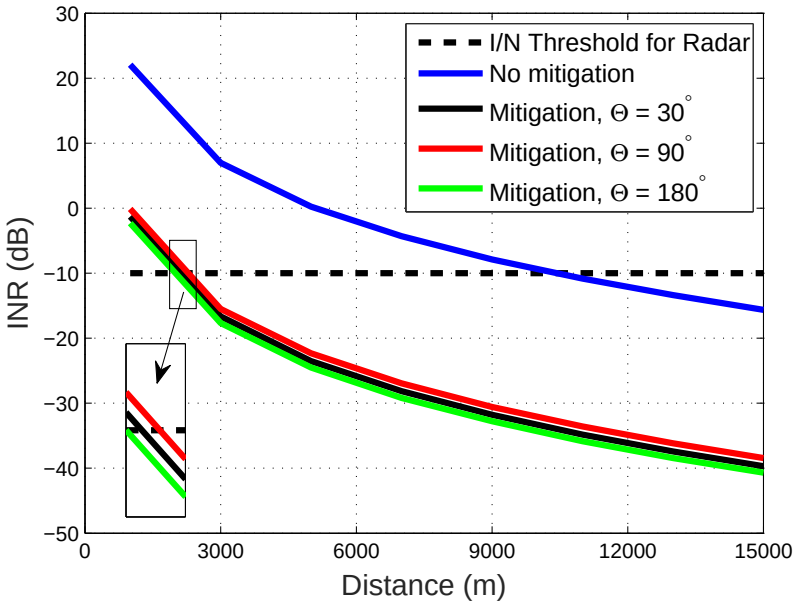

Figure 3.5: `MMAI` vs. Θ ($\lambda_{ap} = 100, \lambda_{sta} = 10$, EDCA)

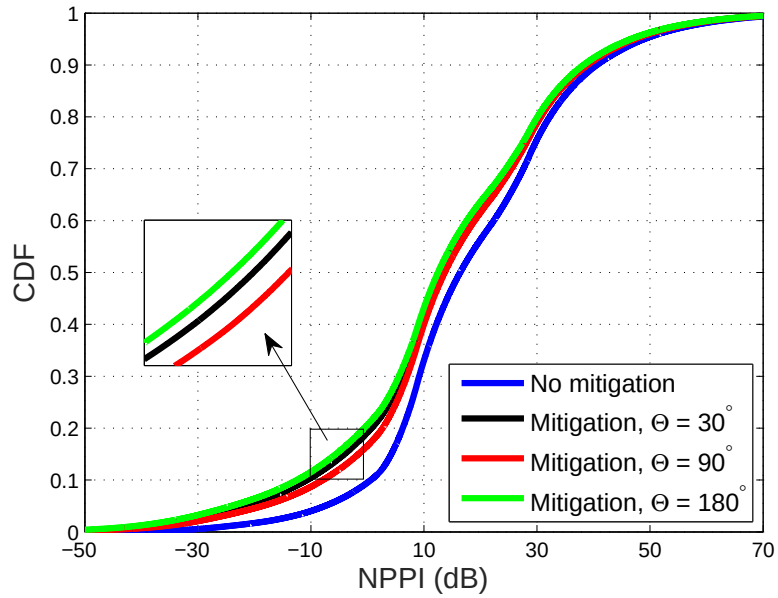

Figure 3.6: CDF of `NPPI` for Θ ($\lambda_{ap} = 100, \lambda_{sta} = 10$, EDCA)

Chapter 4

Communications-Radar Coexistence at 3.5 GHz: Part 2

This chapter discusses coexistence of wireless communications employing OFDM with pulsed radar for spectrum sharing in the 3.5 GHz band. Recall that Chapter 3 presented a geometric approach similar as in Chapter 2, in order to characterize separation distances between outdoor Wi-Fi and radar based on the interference toleration requirements of the two systems. Distinguished from the previous chapter, this chapter focuses on a signal processing aspect that can be applied to general wireless mobile communications systems adopting OFDM.

It proposes Precoded SUbcarrier Nulling (PSUN), an orthogonal frequency-division multiplexing (OFDM) transmission strategy for a wireless communications system that needs to coexist with federal military radars generating pulsed signals in the 3.5 GHz Band. This chapter considers existence of Environmental Sensing Capability (ESC), a sensing functionality of the 3.5 GHz Band coexistence architecture, which is one of the latest suggestions among stakeholders discussing the 3.5 GHz Band. Hence, the chapter considers impacts of imperfect sensing for a precise analysis. An imperfect sensing occurs due to either a sensing error by an ESC or a parameter change by a radar. This chapter provides a framework that analyzes performance of an OFDM system applying PSUN with imperfect sensing. Our results show that PSUN is still effective in suppressing inter-carrier interference (ICI) caused by radar interference even with imperfect pulse prediction.

4.1 Related Work

In [77], a novel radar waveform that minimizes a radar's in-band interference on a coexisting communications system is proposed. This approach assumes that a radar has full knowledge of the interference channel and modifies its own signal vectors in such a way that they fall into

the null space of the channel matrix between the radar and the coexisting communications system. In [78], the coexistence scenario of [77] is extended to more than one interference channel. Our work is distinguished from [77][78] because it proposes a strategy that requires *no change of the incumbent radar system*. It is a meaningful contribution considering the widely acknowledged concern about national security and cost of changing the incumbent system.

In [79][80], opportunistic spectrum sharing between an incumbent radar and a secondary cellular system is studied. The work specifies applications that are feasible in such a coexistence scenario. It is found that non-interactive video on demand, peer-to-peer file sharing, file transfers, automatic meter reading, and web browsing, are feasible, while real-time transfers of small files and VoIP are not. In [81], it is suggested that the secondary communication system utilize information of the incumbent radar that is provided by a database. In [82], impacts of interference from shipborne radars to LTE systems are studied. An eNodeB's signal-to-interference-plus-noise ratio (SINR) plummets when hit by radar pulses, but an LTE system is able to recover during the time between radar pulses. Average throughput of a user equipment (UE) drops under radar interference. The authors concluded that the UE throughput loss in the uplink direction is tolerable even with a radar deployed only 50 kilometers away from the LTE system. In [23], the study in [82] is extended. The authors studied impacts of shipborne radars that co-channel with and in the vicinity of a 3.5 GHz macro-cell and outdoor small-cell LTE systems. With such additional consideration of out-of-band effects of shipborne radars, the authors still conclude that both macro-cell and outdoor small-cell LTE systems can operate inside current exclusion zones. In [83], on the other hand, it is concluded that LTE systems are unable to cope well with narrow-band bursty interference on the downlink. Our work is distinguished from [79]-[83] because in this chapter we study *how to actually cancel radar interference*, while only feasibility of coexistence was discussed in the prior studies.

In addition, this chapter provides *a generalized analytical framework*. It takes into consideration a comprehensive interplay among multiple variables regarding the military radars' operations, such as the number of radars, pulse parameters, antenna sidelobes, and out-of-band emissions, which will be discussed in Section 4.3. Moreover, impacts of imperfect prediction of radar interference are measured by appropriate probabilities which will be explained in Section 4.5.

Note that the work that is provided in this chapter is an extension of our previous study that was published in [71]. The extension is twofold: (i) we change the performance metric from bit error rate to maximum data rate to more fairly reflect the impact of PSUN on an OFDM system performance; (ii) we use 3.5 GHz LTE as a near-term example that serves to illustrate how the technique could be applied to operation of future 5G systems in bands shared with pulsed radars.

4.2 Main Contributions

This chapter takes a signal process point of view to suggest a method that addresses coexistence between a general OFDM-based wireless communications system and pulsed radar in 3.5 GHz band. Main contributions of this dissertation to providing a solution to the coexistence problem can be presented as follows.

Pulse blanking (PB) is known to be one of the most effective techniques for suppressing pulsed interference [96]-[99]. Unfortunately, PB still leaves a significant level of ICI. In PB, time-domain samples of the received signal affected by pulsed interference are set to zero. The technique deteriorates performance of an OFDM system by affecting not only the interfered samples but also the desired samples. This problem occurs due to the fact that (inverse) Fourier transform provides a time-frequency mapping in such a way that every frequency/time sample contributes to generating a time/frequency symbol. In an OFDM system, PB takes place in the time domain whereas the data symbols are mapped to the subcarriers in the frequency domain. An OFDM RX blanks only several samples that are radar-interfered in the time domain. However, such a partial change leads to corruption of all the samples in the frequency domain due to characteristic of the Fourier transform, which still causes ICI. This chapter focuses on suppression of such ICI that remains after applying PB at an OFDM RX.

The main contribution of this research is analysis of coexistence in the 3.5 GHz Band (3.550-3.700 GHz) between the radar (incumbent) and the LTE (secondary). The insights that have been gained through this research so far are summarized as below:

- This research modified the LTE, leaving the incumbent radar unchanged.
- It discussed a method of "actual mitigation" of interference. Previous works only discussed performance under radar interference.
- It reflectd the up-to-date rules of the 3.5 GHz LTE; existence of ESC is included in the final rule for the system.
- It discussed impact of imperfect sensing on the performance of the 3.5 GHz LTE.

The new insights that are expected from the remaining part of this research are listed below.

- The results and framework of this research will be combined with Contribution 2 in order to discuss feasibility of the 3.5 GHz LTE for safety-critical V2V applications.

4.3 Coexistence Model

Recall that this chapter discusses the performance of an LTE small-cell system that coexists with multiple military radars that rotate and generate pulsed signals. It is important to note that we focus on the *downlink* of an LTE system where an eNodeB acts as a transmitter (TX) and a UE becomes a receiver (RX).

Also, we assume that there is no impacts of fading from mobility nor multipath since the ICI that is caused by radar interference has far more significant impacts than Doppler shift and delay spread. Therefore, we assume that the only two channel impairments are *radar interference* and *additive white Gaussian nose (AWGN)*. In other words, an OFDM symbol goes through an AWGN channel when the LTE system is not interfered by the radar. There is a period of time when the radar beam does not point at the LTE system since a radar rotates; during this time, an LTE system is assumed to experience an AWGN channel. It should be noted that hence the simulation results that are presented in Section 4.6 do not take fading into consideration.

4.3.1 Characterization of a Military Radar

It is noteworthy that a 3.5 GHz Band coexistence problem is more challenging than is often acknowledged. This study considers two aspects that increase the impact of a pulsed radar's interference on an LTE cell: a radar's antenna sidelobes and out-of-band emissions. These analogous spatial and frequency domain effects are serious due to the *extreme difference in transmit power between radar and LTE*.

Antenna Sidelobes

Following the FCC's guideline in designing a CBRS system coexisting with military radars [73]-[75], a sufficiently large spatial separation must be guaranteed between a federal military radar and an LTE system to guarantee a low level of interference from an LTE eNodeB (TX) to the radar. In spite of this large distance from a radar, an LTE UE (RX) cannot avoid radar interference with a very high level due to the much higher transmit power of a radar. The power of a radar's signal received at an LTE RX is so high that even sidelobes cause significant interference to the communications system. This is interpreted as *a greater value of horizontal angle of a radar's beam* that actually causes interference on a coexisting LTE system. Figure 4.1 illustrates such an impact of a radar antenna's horizontal sidelobes. It describes that the angle of a radar beam, θ_{beam}, contains not only its main lobe but also the sidelobes. The value of θ_{beam} differs according to type of radar. For instance, the antenna pattern of a radar analyzed in [7] has cosine pattern with sidelobes that are 14.4 dB lower than the main lobe.

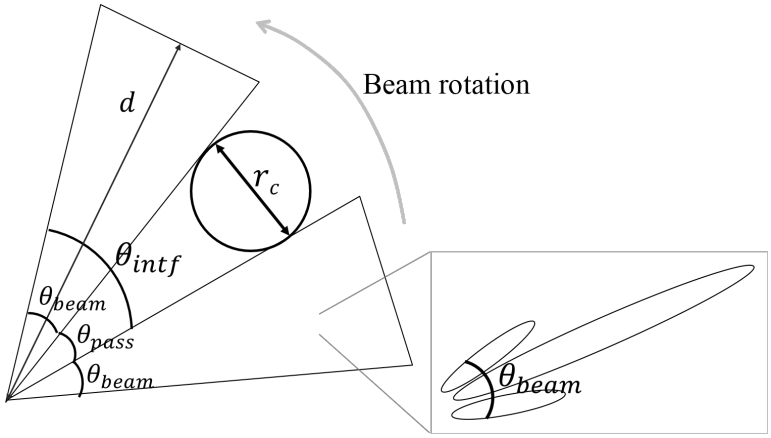

Figure 4.1: Impact of antenna horizontal sidelobes

Table 4.1: Parameters for antenna horizontal sidelobe analysis

Parameter	**Remark**
θ_{beam}	Angle of a radar antenna's horizontal beam with main lobe and sidelobes that cause interference on an LTE system
θ_{pass}	Angle that a radar antenna's horizontal beam passes through an LTE cell
θ_{intf}	The total angle that a radar antenna's horizontal beam interferes an LTE cell
d	Distance between a radar and an LTE cell
r_c	Diameter of an LTE cell
T_{rot}	Radar rotation time

Now we formulate such a coexistence model in which an LTE system is interfered by a radar that rotates and transmits pulses. Table I describes parameters used in the analysis, including those shown in Figure 1. Suppose that a radar rotates counterclockwise and an LTE system is within interference range of the radar's signal. The angle of rotation during which the radar's beam passes through a cell of an LTE system is given by

$$\theta_{pass} = \frac{360^\circ \cdot r_c}{2\pi d}. \tag{4.1}$$

As illustrated in Figure 4.1, the total angle through which the radar beam interferes with a cell of an LTE system can be written as

$$\theta_{intf} = \theta_{beam} + \theta_{pass}. \tag{4.2}$$

Note that θ_{beam} differs according to type of radar, while θ_{pass} is determined by d and r_c. Then the total interference time is defined as the time period when a cell of an LTE system is interfered by a radar within a beam rotation, which is obtained by

$$T_{intf} = \frac{\theta_{intf}}{360} \cdot T_{rot}. \tag{4.3}$$

Such an impact of a radar's antenna horizontal sidelobes is evidenced in Figure 5 of [95]. The report describes an observed case in which a wireless communication system receives energy from an SPN-43 shipborne radar at a level that is approximately 30-dB higher than the noise floor, even when the main lobe of the radar antenna is towards the direction opposite to a cell of the wireless communications system. This implies that sidelobes of a radar beam can have a significant impact on operation of a coexisting wireless communications system.

Out-of-Band Emission

Due to extremely high peak transmit power of a radar, out-of-band emission from a radar operating in a neighboring channel also has a significant impact on a coexisting LTE system. Radars themselves are separated among different channels to avoid interfering with each other. This spectral separation is enough to protect radars from interference due to other radars, but is insufficient to protect a wireless communications system that operates with a much lower transmit power.

Figure 4.2 illustrates a simulation result of a radar's out-of-band interference on an LTE system. We simulated an LTE system operating at 3.5 GHz and a radar generating pulses at 3.5, 3.55, and 3.6 GHz. The transmit powers of a radar and an LTE eNodeB are assumed to be 83 dBm and 23 dBm, respectively. The distance between an LTE eNodeB and a UE is 100 meters, while the radar is assumed to be separated by distance of 100 kilometers. Also, the radar's pulse repetition time (PRT) and duty cycle are 1 msec and 10%, respectively. A radar has an extremely large bandwidth due to its pulsed nature. Since transmit power

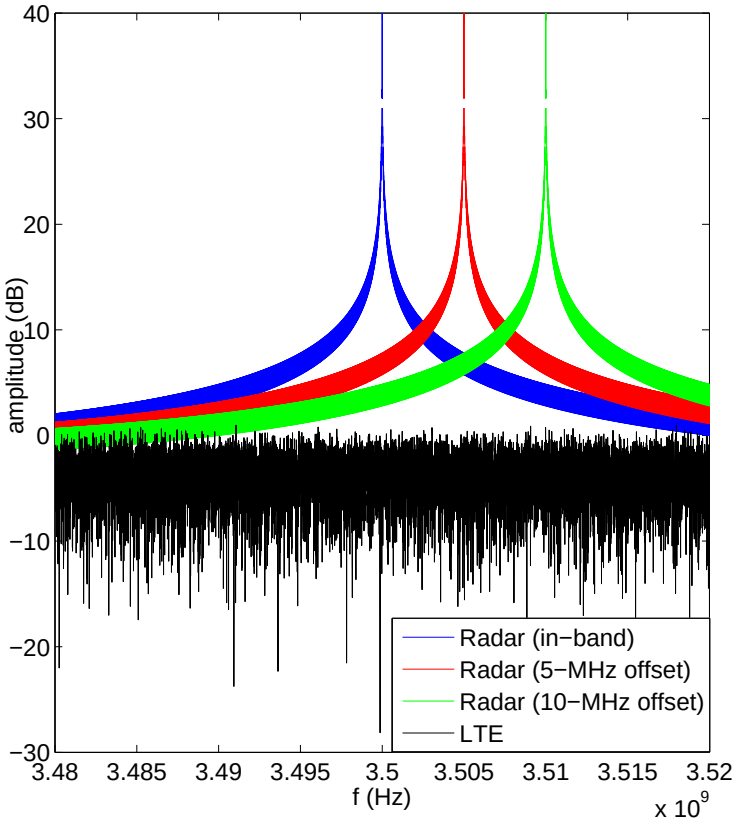

Figure 4.2: Impact of out-of-band emissions

of a radar is too much higher than that of a wireless communications TX, it is still higher than an LTE eNodeB's signal at a UE, even with a 50-MHz or 100-MHz offset. This implies that we must take into account interference caused by radars' out-of-band emissions when we analyze coexistence between a pulsed radar and a wireless communications system. As mentioned earlier, a radar's out-of-band transmission does not cause significant interference to another radar in an adjacent band because transmit powers of the radars are similar. However, to an LTE system, an out-of-band radar emission causes significant interference due to a significant difference in transmit power between an LTE eNodeB and a radar.

Regarding the simulation setting discussed above, it is noteworthy to elaborate the rationale behind selection of the value of *path loss exponent* that equals to 2. In the geography of the coexistence model, the lengths are significantly different between the two main parts: (i) between a radar and an LTE system; (ii) between an eNodeB and a UE in an LTE system. The idea is that the former part is much longer in distance, and thus more affected by the path loss. In the former part of a coexistence geography, the path loss becomes the dominant channel impairment due to the long distance (e.g., tens of kilometers). On the other hand, in the latter part, radar interference becomes the main channel impairment since the path loss does not influence the performance due to short-distance propagation. As mentioned earlier, in a LTE–radar coexistence scenario, the former part is much longer in length than the latter part. Therefore, when selecting a value of the path loss exponent, it is the former part that we should consider more significantly than the latter part. Since the former part is very likely composed of a long line-of-sight path, it is reasonable to assume the path loss exponent to be 2.

Such interference from out-of-band radars can be interpreted as a greater number of radars that cause interference since radars operating in neighboring channels also cause interference to an OFDM system. Hence, there are additional bursts of interference from the out-of-band radars within an in-band radar's rotation period. It is likely that the radars have different values of T_{rot}, duty cycle, and PRT, which makes the task of an LTE system to track interfering pulses more difficult. In this work, we reflect the impact of out-of-band interference due to radars on lower and upper adjacent frequencies in such a way that there occurs a *three-fold increase* in the number of OFDM symbols that are hit by a radar pulse. Therefore, *the total length of time that a radar interferes with an LTE cell within a radar rotation*, T'_{intf}, can be given by $T'_{intf} \leq 3T_{intf}$. Note that $T'_{intf} = 3T_{intf}$ is true when there is no overlap in time among pulses generated by the three radars.

Table 4.2 demonstrates T'_{intf} according to different values of θ_{beam}, assuming that $T'_{intf} = 3T_{intf}$. We set θ_{beam} to $5, 10$, and 30 degrees. Let us apply $T'_{intf} = 595.5$ msec to the current LTE standard as an example. Within a radar rotation time $T_{rot} = 2$ sec, 2000 LTE subframes can be transmitted. Since 14 OFDM symbols are transmitted in a subframe, 28000 OFDM symbols can be transmitted. As a result, $\frac{595.5}{2000} \times 28000 \approx 8337$ out of 28000 OFDM symbols are hit within a rotation of a radar.

Table 4.2: Computation of the total interference time T'_{intf}

θ_{beam} (deg)	θ_{intf} (deg)	T_{intf} (msec)	T'_{intf} (msec)
5	10.7	59.6	178.8
10	15.7	87.4	262.2
30	35.7	198.5	595.5

4.3.2 Generalized Expression of Radar Interference

In the 3.5 GHz Band, radars report their operating parameters (i.e., pulse parameters and position) to a SAS, and an ESC also senses and sends the parameters to a SAS. Based on such a coexistence model, *the frequency of pulse interference within a certain time* can be quantified for use in analysis. There are four factors affecting the frequency: (i) the number of radars, (ii) PRT of a radar, (iii) level of interference from antenna sidelobes of a radar, and (iv) level of interference caused by out-of-band radars. However, it is extremely difficult for an ESC to keep track of all the four factors since military radars keep changing their parameters and the radars' parameters are even classified in many cases, as explained in an army's regulation document [84]. To this end, this research generalizes the frequency of pulse occurrence by defining a quantity called *the probability of pulsed interference*, ρ. It is defined to be the probability that an OFDM system experiences a pulsed interference within a certain period of time. In this way, the quantity ρ generalizes the impacts of all of the four factors described above.

Note that the LTE standard's parameters are adopted for simulation of a CBRS system as will be demonstrated in Section 4.6, and the scope of defining ρ is 1 msec, the length of a subframe defined in the LTE standard. If $\rho = 0$ during a simulation of 1000 subframes, none of the subframes are hit by a radar pulse. If $\rho = 1$, on the other hand, every subframe experiences radar interference during the simulation. Note that this analytical framework can be extended to any other type of OFDM communication without loss of generality. In other words, the definition of ρ can be set within any specified time period that can be measured by the number of OFDM symbols.

4.4 Precoded SUbcarrier Nulling (PSUN)

4.4.1 Motivation of PSUN

The PHY-layer approach is a very thoroughly studied area relative to the geometric approach. Therefore, this dissertation relies on a certain policy in selection of techniques: "the best performance in suppression of pulsed interference from a radar."

Motivation of PB

The most straightforward description on motivation of using the technique is presented in [85][86]: "PB is easy to implement, while providing a remarkable performance gain, compared to a conventional OFDM receiver."

In general, OFDM systems are less sensitive to impulsive noise than single carrier systems. The longer OFDM symbol duration provides an advantage, since the impulsive noise energy is spread among simultaneously transmitted OFDM subcarriers. However, it has been recently recognized that this advantage turns into a disadvantage if impulsive noise energy exceeds a certain threshold [87][88]. A simple method of reducing the adverse effect of impulsive noise is to precede a conventional OFDM demodulators with PB. This method is widely used in practice, because it is very simple to implement and provides an improvement over conventional OFDM demodulators in impulsive noise channels [88]-[90]. However, performance analysis of this scheme has not yet appeared. In this chapter, we address the problem of optimal threshold selection and performance characterization of an OFDM receiver that uses PB for impulsive noise cancellation.

It should be noted that the idea of using PB for impulsive noise cancellation is not new. It was shown over four decades ago that the locally optimal detector for arbitrary signals in impulsive noise under a low signal-to-noise ratio (SNR) assumption is comprised of a conventional detector (optimal in a Gaussian noise environment) preceded by amemoryless PB [91][92].Generally, the shape of the optimal memoryless PB is determined by the probability density function of the impulsive noise process [91][92]. However, it is shown that the PB is one of the best (and the simplest) approximations to the locally optimal nonlinear preprocessor [93][94]. Recently, the idea of using (suboptimal) PB for impulsive noise cancellation has been successfully applied to modern OFDM communication systems [88][90].

Drawback of PB

As such, interference power is reduced significantly with PB. However, the approach affects an OFDM signal such that the potential performance improvement degrades considerably. Considering PB, the impact on the OFDM signal can be determined and compensated to a wide extend. However, this is not applicable to clipping, since the RX signal is clipped rather than simply erased.

The impact of PB on the OFDM signal can be determined exactly when representing PB as a windowing operation. The window function is a rectangular window that exhibits notches at those positions where the RX signal is blanked. Recalling that the shape of the window determines the spectrum of the OFDM subcarriers, the subcarrier spectra can be determined and the distortion induced by PB is identified as ICI. The ICI can easily be reduced by subtracting the known impact of all other subcarriers from the considered subcarrier as applied for example for reducing ICI in OFDMA induced by frequency offsets

[97].

Motivation of ISC

We now discuss the solution for the aforementioned problem of ICI still remaining after PB due to damages to desired signals. One can expect several techniques to address this drawback of PB.

This work suggests that the negative impact of PB can be considered a form of time-selective fading. Channel coding is usually applied in combination with interleaving and diversity to mitigate performance degradation due to fading [100]. In OFDM systems, the main means of combating time-selective fading are block interleaving and antenna diversity. However, our results indicate that neither method can effectively mitigate ICI caused by PB. Interleaving is ineffective because PB does not result in bursty errors due to the one-to-all mapping characteristic of the Fourier transform. Antenna diversity is also not effective against the ICI caused by PB because an entire LTE cell is likely to be hit at once by a radar's beam. A multiple-antenna technology can bring no benefit when the signals received by all the antennas are interfered with simultaneously.

Prior art started to be interested in ISC as a countermeasure against frequency offset, one of the most significant challenges that OFDM inherently has. To mitigate the problem, two types of approaches have been proposed in the literature. One is estimation. A RX estimates and removes the frequency offset [103]-[106]. In this approach, the frequency-offset estimation is generally performed in two steps: coarse frequency-offset estimation, which estimates the part of frequency offset that is a multiple of the subcarrier spacing, and fine frequency-offset estimation, which estimates the remaining part of the offset that is smaller than half the subcarrier spacing. While many methods exist that can estimate and remove the frequency offset quite accurately, they often have considerable computational complexity.

Another approach is to use signal processing and/or coding to reduce the sensitivity of the OFDM system to the frequency offset [107]. These methods can either be used as low-complexity alternatives to fine frequency-offset estimation techniques or they can be used together with a somewhat accurate oscillator. Windowing has also been used to reduce the ICI created as a result of frequency offset [108][109].

A simple and effective method known as the ICI self-cancellation scheme where polynomial coding in the frequency domain is used to mitigate the effect of frequency offset [101][102]. In the Zhao-Haggman method, copies of the same data symbol are modulated on adjacent subcarriers using optimized weights. The weights are designed such that at the receiver, after maximal ratio combining of these copies, the signal of each subcarrier is shaped in frequency such that less ICI is created when a frequency offset is present. This method can significantly reduce ICI at the price of lowering the transmission rate by a factor of L and a slight increase in complexity. Zhao and Haggman show that, compared to a coded system with a similar

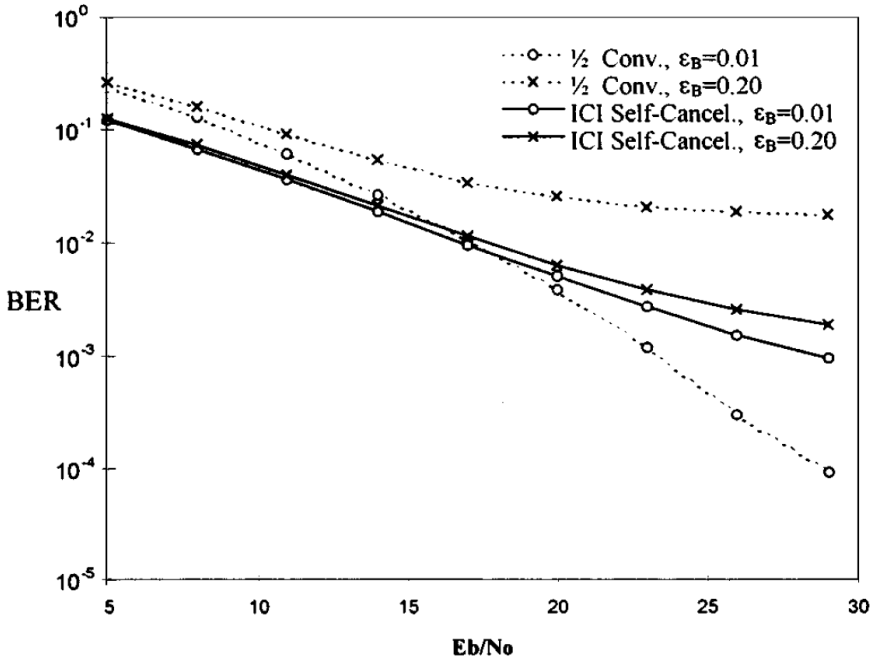

Figure 4.3: Comparison of BER between ISC and error correction coding [102]

rate $(1/L)$, their proposed scheme has better performance. Other frequency-domain coding methods have been proposed that do not reduce the data rate [110][111]. However, these methods produce less reduction in ICI.

Effectiveness of ISC

Fig. 4.3 presents BER simulation results of the ICI self-cancellation scheme compared with results for the error correction coding system. The channel is the typical urban area channel, and frequency-domain differential decoding is used in both systems. The comparison will be carried out between two systems. One is a binary phase shift keying (BPSK) modulation OFDM applying ICI self-cancellation scheme. The other is BPSK modulation with 1/2 convolutional coding, where the Viterbi algorithm is used for soft-decision decoding. The two systems have the same bandwidth efficiency. Since the ICI self-cancellation scheme is intended to minimize system ICI, it performs better in the case when the ICI signals dominate the channel interference. On the other hand, the convolutional coding will give a larger coding gain when the frequency offsets are small and is high.

In addition, the ICI self-cancellation scheme can be combined with error correction coding. Such a system is robust to both AWGN and ICI, however, the bandwidth efficiency is reduced.

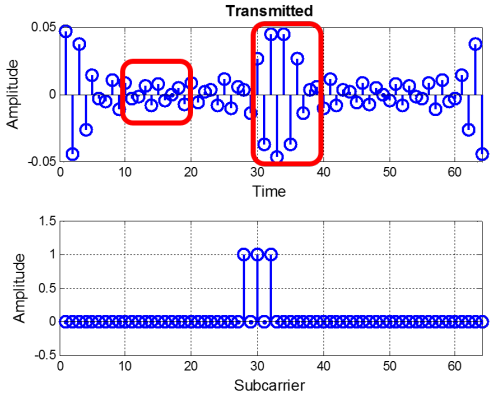

(a) Transmitted

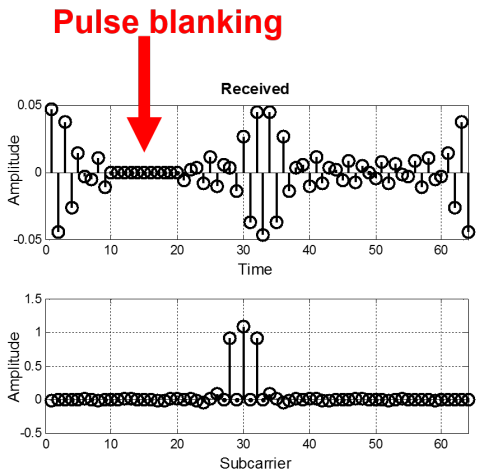

(b) Received (PB on *low-amplitude* samples)

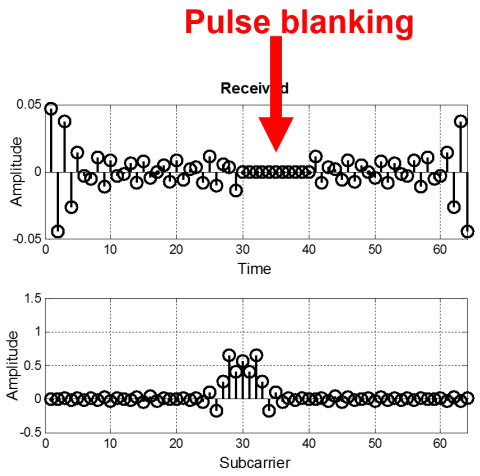

(c) Received (PB on *high-amplitude* samples)

Figure 4.4: Dependency of ICI on the location of PB

Table 4.3: Existing ICI self-cancellation (ISC) schemes and the proposed subcarrier nulling ($L = 2$)

Scheme	**Subarrier allocation**
Data conversion [101]	$X'(k) = X(k), \quad X'(k+1) = -X(k)$, where k is the subcarrier index
Symmetric data conversion	$X'(k) = X(k), \quad X'(N-k-1) = -X(k)$, where N is the FFT size
Weighted data conversion [112]	$X'(k) = X(k), \quad X'(k+1) = -\mu X(k)$, where μ is a real number in $[0, 1]$
Plural weighted data conversion [113]	$X'(k) = X(k), \quad X'(k+1) = -e^{-j\pi/2}X(k)$
Data conjugate	$X'(k) = X(k), \quad X'(k+1) = -X^*(k)$
Data rotated and conjugate [114]	$X'(k) = X(k), \quad X'(k+1) = -e^{-j\pi/2}X^*(k)$
PSUN	$X'(k) = X(k), \quad X'(k+1) = 0$

4.4.2 Proposition of PSUN

As aforementioned, ICI self-cancellation (ISC) is an aggressive means of combating ICI. It cancels ICI by allocating precoded $L - 1$ redundant subcarriers between data subcarriers, which results in a $1/L$ data rate. Based on the work of Zhao and Haggman [101], several ISC schemes have been proposed [112]-[114]. Some of the existing ISC schemes are summarized in Table 4.3, assuming $L = 2$. Note that $X(\cdot)$ and $X'(\cdot)$ indicate the original transmitted data symbol and the symbol after ISC precoding, respectively.

We discovered that the most effective way of reducing ICI induced by PB is *to insert null subcarriers*, instead of allocating any other types of redundant subcarriers. The rationale is illustrated in Figure 4.4. It is an example that is simplified to clearly demonstrate the impact of location of PB on the level of ICI. Figure 4.4(a) represents an example signal at TX while Figs. 4.4(b) and (c) show *two different locations of PB* at RX. The example signal contains three among 64 subcarriers around the center (28th, 30th, and 32nd) that are set to 1 while all the others set to 0. Note that the transmitted signal in Figure 4.4(a) shows the real part of the original complex signal. It is observed from Figure 4.4 that the location of PB has a very significant impact on the level of ICI caused by PB. Comparing Figure 4.4(b) and (c), *the ICI becomes more severe as higher-amplitude samples are blanked*. In other words, the ICI level can be reduced as the time-domain fluctuation gets flatter. It is straightforward that the simplest way of keeping time-domain amplitudes low is to reduce the number of subcarriers. An OFDM RX can suppress ICI remaining after PB better when a TX has allocated *null subcarriers* instead of other types of redundancy, since use of null subcarriers reduces the number of high-energy bins in the time domain.

For this reason, an OFDM TX employing PSUN *precodes an OFDM symbol by inserting null tones between data tones so that the ICI after PB at its RX can be suppressed*. This makes PSUN a type of ISC, as listed in Table 4.3. Various manners of inserting null tones for different purposes have been studied in the literature [118]-[120]. In this work, PSUN allocates the null tones in such a way that the radar interference is minimized. Figure 4.5 shows that PSUN outperforms the other ISC schemes. Note that for the Weighted data conversion scheme the value of μ becomes 1/2. The reason for PSUN's higher performance is that PSUN yields smaller variation of an OFDM symbol in the time domain because it transmits a smaller number of subcarriers.

4.4.3 The Transmission Protocol of PSUN

Let r denote the coding rate of PSUN. With the coding rate of $r = 1/L$, PSUN inserts $L - 1$ null tones between data tones. Figure 4.6 illustrates how PSUN inserts null tones in an exemplar OFDM symbol, with Quadrature Phase Shift Keying (QPSK) and the Fast Fourier Transform (FFT) size of 32. Figure 4.6(a) demonstrates an OFDM symbol without PSUN. Figure 4.6(b) and (c) show examples of precoding the OFDM symbol using PSUN with r equal to 1/2 and 1/4, respectively. PSUN extracts the first half/fourth of the data tones from the original OFDM symbol given in Figure 4.6(a). Note that this method of taking $1/L$ of its original data is only an example. PSUN can do it in various other ways; another example is to extract a data tone in every L subcarriers. Then PSUN inserts null tones (marked with red squares) between the data tones, which leads to the mapping illustrated in Figure 4.6(b) and (c).

This is where PSUN sacrifices data rate by $1/r$ within an OFDM symbol. To minimize such loss of data rate, an OFDM TX performs two important operations when adopting PSUN. First, it *localizes OFDM symbols to be hit a priori and allocates null tones in the symbols only*. The a priori knowledge about radar pulse parameters is provided by a SAS, but sensed by an ESC beforehand. Figure 4.7 shows a subframe in which an OFDM symbol is expected to be hit by a radar pulse. Only that symbol is precoded with the null subcarriers at TX before transmission. Second, within the OFDM symbol to be radar-interfered, an OFDM TX *disables channel coding and shifts the saved redundancy to PSUN*. This assumes that for an OFDM symbol to be radar-interfered, the pulsed interference is more severe than AWGN. This protects the symbol from radar interference, while keeping the total number of transmitted bits the same. Multiple OFDM symbols can be hit simultaneously because an interference pulse can either be shorter or longer than an OFDM symbol. In this case, the OFDM symbols are all precoded. All the other symbols that are not precoded are transmitted with channel coding and full data tones.

Figure 4.7 illustrates PSUN from such a macroscopic standpoint. An OFDM TX employing PSUN reduces loss of data rate by *selecting certain OFDM symbols to insert null subcarriers*. According to the FCC's suggestion, a priori knowledge of interference from incumbent

radars is available at an LTE eNodeB. Radars report their operating parameters (i.e., pulse parameters and position) to a SAS, and an ESC also senses the parameters and sends them to a SAS.

Taking LTE as an example of a CBRS system, there are 14 OFDM symbols in a subframe. Figure 4.6 showed only one OFDM symbol that is expected to be hit by a radar pulse. In Figure 4.7, an OFDM symbol to be radar-interfered is highlighted by orange color. However, there are 13 other OFDM symbols that are not radar-interfered. An OFDM TX applying PSUN does not precode these OFDM symbols for two reasons: (i) they undergo AWGN channels against which channel coding achieves better protection than PSUN; (ii) thus, as explained earlier, unnecessary loss of data rate can be avoided by not applying redundancy in subcarriers.

It is possible that two or more consecutive OFDM symbols can be interfered by the same pulse because an interference pulse can either be shorter or longer than an OFDM symbol depending on the pulse's duty cycle. In such a case, all of the OFDM symbols that are expected to be radar-interfered are precoded.

4.5 Imperfect Pulse Prediction

We discovered that based on the Neyman-Pearson detection theory, two types of imperfect pulse prediction are possible in this 3.5 GHz Band coexistence framework: false prediction and (ii) missed prediction. *False alarm* and *missed detection* are defined as an ESC's inaccurate claim of presence/absence of an interfering radar pulse, given that a pulse is in fact absent/present. More specifically, it is called a false alarm when an ESC predicts that an OFDM symbol is to be hit by a radar pulse but in fact the radar pulse does not hit the OFDM symbol. A missed detection is the opposite; an ESC predicts that an OFDM symbol is not to be hit but in fact the symbol is hit by a radar pulse. It will be formulated based on the detection theory in Section 4.5.1.

Let us interpret actual impacts of the two types of imperfect pulse prediction. Recall that channel coding and PSUN are countermeasures against AWGN and pulsed interference, respectively. A *false alarm* is interpreted as a situation where an OFDM symbol that is not to be radar-interfered is predicted to be radar-interfered and thus precoded with PSUN. Therefore, in the OFDM symbol, redundant bits for channel coding are removed and null subcarriers are allocated instead which is a weaker protection than channel coding against AWGN, but in fact the symbol is not hit by a radar pulse but goes through an AWGN channel. On the other hand, when a *missed detection* occurs, an OFDM symbol to be radar-interfered is not predicted to be radar-interfered and thus not precoded with PSUN. Thus the OFDM symbol is protected with channel coding instead which is a weaker protection than PSUN against pulsed interference. Overall, although in the opposite way, either a false alarm or a missed detection deteriorates performance of an OFDM system that applies

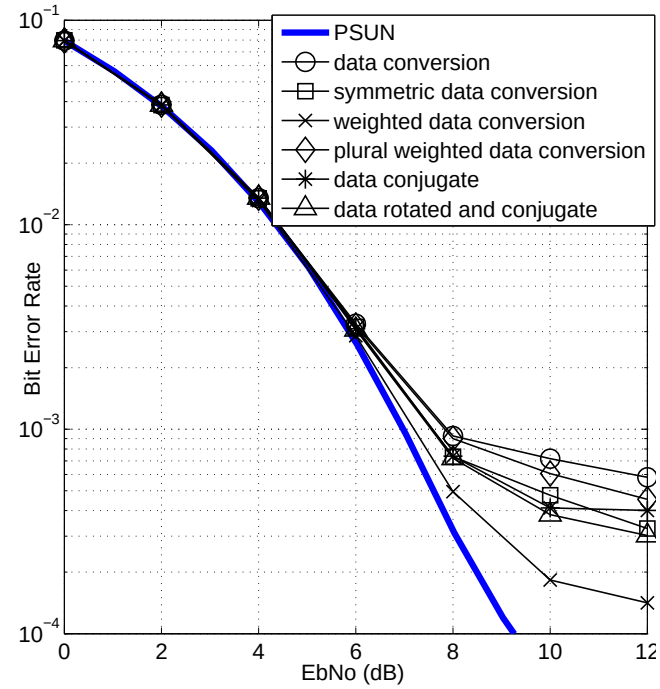

(a) Pulse duty cycle of 1%

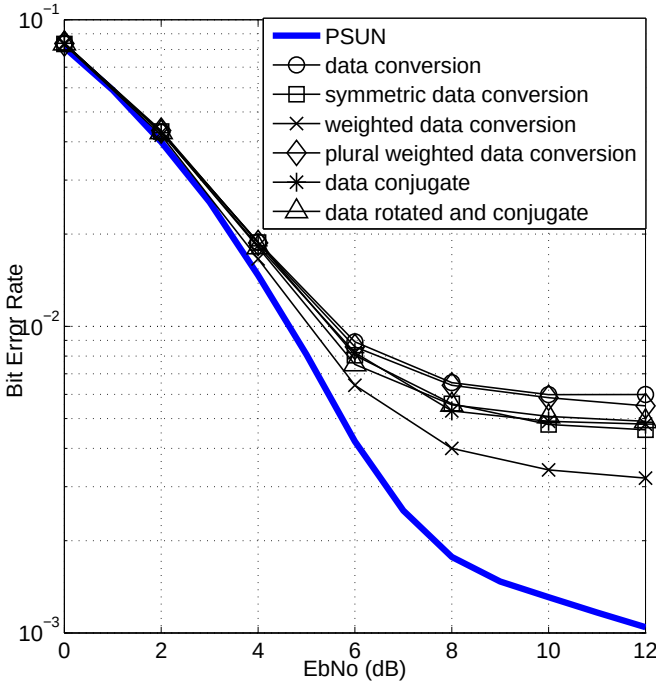

(b) Pulse duty cycle of 10%

Figure 4.5: Comparison of PSUN to other ISC schemes (QPSK, 1024-FFT)

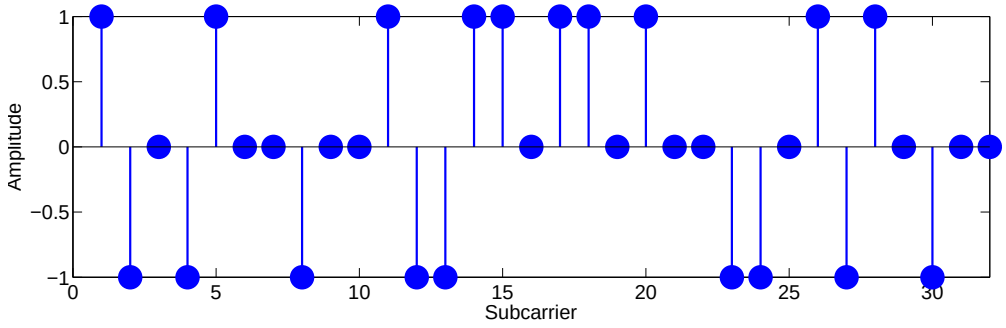

(a) Without PSUN

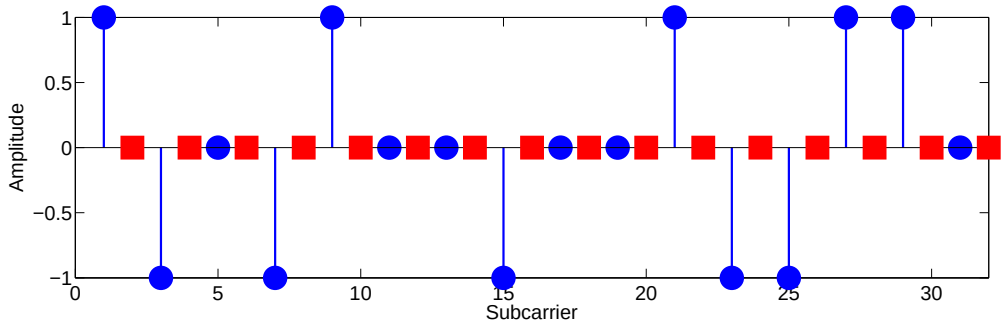

(b) With PSUN ($r = 1/2$)

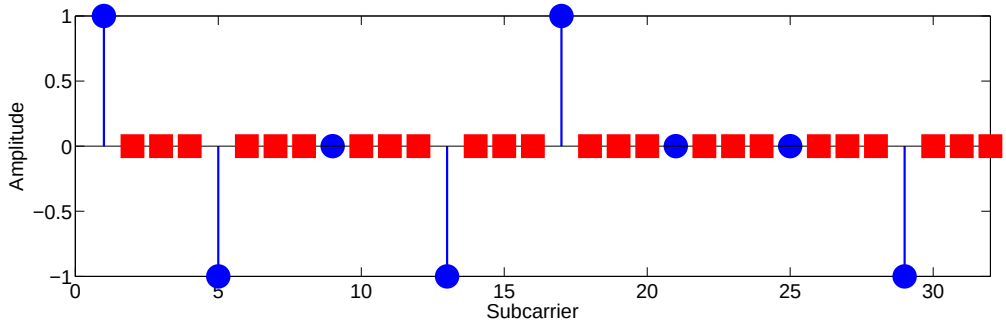

(c) With PSUN ($r = 1/4$)

Figure 4.6: An OFDM symbol applying PSUN (QPSK, 32-FFT)

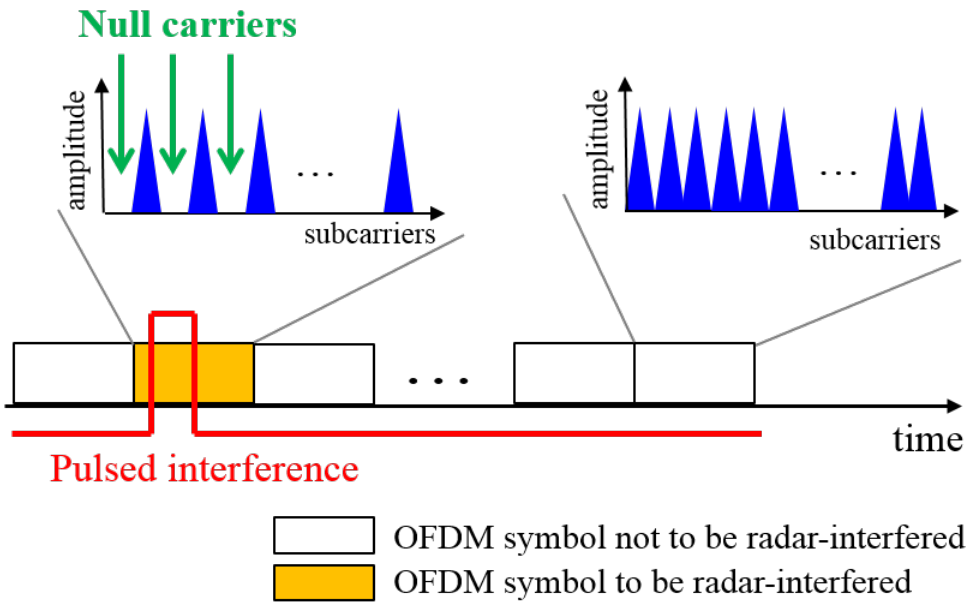

Figure 4.7: Transmission protocol of PSUN ($r = 1/2$)

PSUN.

Major causes of the above imperfect pulse prediction are twofold. Firstly, an ESC can cause sensing errors. Secondly, an ESC can lose track of radars' pulse parameters. The former affects false alarm and missed detection, while the latter impacts all of the two types of imperfect pulse prediction.

4.5.1 Sensing Error by an ESC

Typically for a protocol requiring spectrum sensing, either a matched filter or an energy detector can be used [115][116]. This chapter assumes that an ESC, a device with sensing capability, uses an energy detector. Assuming that an interference signal from a radar and noise are both modeled as white Gaussian processes, the problem of sensing a radar's pulsed interference signal by an ESC can be given by the following hypotheses test:

$$H_0 : Y \sim \mathcal{N}\left(0, \sigma_0^2\right) \tag{4.4}$$

$$H_1 : Y \sim \mathcal{N}\left(0, \sigma_0^2 + \sigma_1^2\right) \tag{4.5}$$

where

Y: an observation sample;

σ_0^2: power of noise;

σ_1^2: power of an interference signal.

Since an ESC adopts an energy detector, based on the Neyman-Pearson detection theory, the probability of false alarm, P_{fa}, and missed detection, P_m, are defined by

$$P_{fa} \triangleq Pr\left(H_1|H_0\right) = 1 - \Gamma\left(\frac{1}{2}, \frac{\eta_{se}}{2\sigma_0^2}\right) \tag{4.6}$$

$$P_m \triangleq Pr\left(H_0|H_1\right) = 1 - \Gamma\left(\frac{1}{2}, \frac{\eta_{se}}{2\left(\sigma_0^2 + \sigma_1^2\right)}\right) \tag{4.7}$$

where η_{se} denotes the sensing error threshold and the incomplete gamma function is given by

$$\Gamma\left(t, z\right) = \frac{1}{\Gamma\left(t\right)} \int_0^x t^{t-1} e^{-x} dx. \tag{4.8}$$

A receiver operating characteristic (ROC) curve is used for an analysis of interplay between P_{fa} and P_m. Figure 4.8 shows ROCs of the Eqs. (4.6) and (4.7) according to the energy per bit to noise power spectral density ratio (EbNo). An increase in the sensing threshold for given signal and noise power values moves the operating point toward the upper direction along one of the curves in the figure. At a high EbNo regime both P_m and P_{fa} can maintain low values, even if the sensing threshold changes much. This is not the case for a low EbNo.

4.5.2 Loss of Track of Radars' Operating Information

It is difficult to track a radar's pulsed signals for the following two reasons. Firstly, the pulse information might not be fully available to the SAS. There has been strong opposition from military stakeholders to providing information to the database about radars' position or other information that could make them more prone to be affected by enemy jammers. Secondly, a radar may change its pulse parameters and position for various purposes, such as higher security or avoidance of interference among radars. According to a recent extensive survey work [117], most radar systems have fixed position and operating parameters. However, airborne and shipborne radars may not have pre-planned routes and, therefore, an error region has to be defined for such cases. In this case, there occurs a time during which an ESC loses track of a radar's pulse parameters. An ESC requires some time to sense a radar's parameter changes, during which it cannot avoid providing outdated information to a SAS.

We suggest that an ESC's losing track of radars' operating information must be understood more seriously than an ESC's sensing errors. The reason is that it is more likely and can cause any of the two types of imperfect pulse prediction, but is more difficult to study since it is not a characteristic of an ESC but that of a radar which is an independent variable in

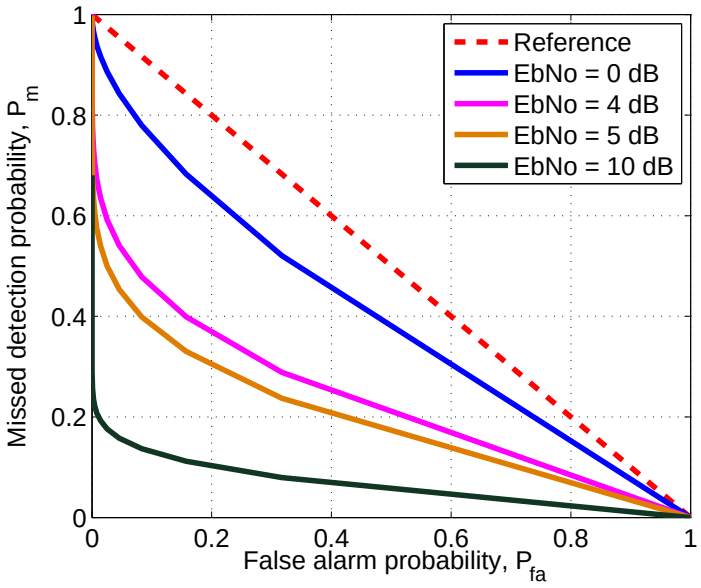

Figure 4.8: ROCs of the energy detector at an ESC

this chapter. Therefore, this chapter provides a framework for analyzing this loss of track. The false alarm and missed detection probabilities–P_{fa} and P_m–are spanned over the range of $[0, 1]$, so that the analysis can be generalized over any case in which an ESC loses track of radars' operating parameters.

4.6 Performance Evaluation

4.6.1 Simulation Setup

The discussion in [79][80] can be interpreted that the CBRS system coexisting with the pulse radar utilizes spectrum more efficiently in the downlink than in the uplink, in terms of the data rate per megahertz. Hence, spectrum sharing with radar would be more appropriate for applications that require greater capacity in the downlink than the uplink, which is a typical characteristic of many applications. Therefore, this chapter assesses the performance of the downlink of an LTE system by measuring *the number of bits per second that an LTE UE successfully receives*. The number of *transmitted* bits differs according to the modulation scheme. (In simulations of this work, 16-Quadrature Amplitude Modulation (QAM) and 64-QAM were evaluated.) We analyze the metric as functions of six variables that are chosen to represent three different aspects of a coexistence between an LTE RX and military radars as follows. (i) EbNo represents impact of AWGN; (ii) Pulse duty cycle and ρ represent

Table 4.4: Simulation parameters

Parameter	**Value**
LTE	
FFT size	1024
Subcarrier spacing	15 kHz
Sampling frequency	15.36 MHz
OFDM symbol time	66.7 us
Subframe length	1 ms
Cyclic prefix (CP) length	5.2 us (1st) / 4.69 us (the following 6)
OFDM symbols/subframe	14
Modulation	16-QAM, 64-QAM
Channel coding	(133,171) Convolutional code ($r = 1/2$)
PSUN	$r = 1/2$
Radar	
Pulse repetition time	1 ms
Rotation rate	30 rpm

characteristics of interference by a radar; (iii) P_{fa} and P_m represent impacts of imperfect pulse prediction. Each variable gauges different levels of channel impairment, i.e., AWGN or radar interference. It differentiates the bit error rates which again directly determines the number of *received* bits.

Table 4.4 summarizes the simulation parameters for LTE and radar. We leverage LTE physical-layer simulations which are 3GPP compliant [121]. The FFT size is set to 1024 but the results based on this parameter can hold for other values of FFT size. The reason is that PB is a channel impairment that occurs in time domain, and LTE is always synchronized in time regardless of FFT size. Coding rates of channel coding and PSUN are kept identical to be $r = 1/2$, for ease of demonstrating the impacts of shifting redundancy from channel coding to subcarrier nulling. The only two channel impairments that are considered in this chapter are AWGN and radar interference, as a result no typical fading effects are considered. Hence the simulations do not accurately follow the modulation and coding scheme (MCS) that are associated with channel quality indicator (CQI). *In order for LTE to operate in the 3.5 GHz Band, a new set of MCS and CQI must be matched.* Radar pulse repetition time is set identical to an LTE subframe duration (1 msec) for accuracy of computation. Each simulation is conducted through 1e6 subframes.

To elaborate the discussion about a new set of MCS and CQI, we claim that it will be necessary because the 3.5 GHz environment is a totally different one from the previous spectrum bands that LTE systems have been operating at. In addition to all the mobility and multipath impacts, design of an LTE system at the 3.5 GHz Band needs to consider

pulsed interference generated by radars. However, this exceeds the scope of this dissertation and will be discussed in our future work. In other words, the results that are discussed in this chapter do not have any impact from the new set of MCS and CQI.

4.6.2 Results

EbNo

Figure 4.9 shows the number of received bits per second versus EbNo with 16-QAM and 64-QAM. Recall that an OFDM TX employing PSUN disables channel coding but puts the redundancy saved from no channel coding to null subcarriers between data subcarriers instead. In low EbNo region, AWGN is the predominating channel impairment that outweighs radar interference, which results in lower effectiveness of PSUN. In other words, outperformance of PSUN over the case without PSUN gets increased as EbNo gets higher. In that way, radar interference becomes prevailing which leads to greater performance advantage of PSUN. Moreover, such advantage of PSUN gets greater with higher modulation order.

Pulse Parameters of the Radar

Figure 4.10 demonstrates the number of received bits per second versus the duty cycle of a radar pulse. We generalized the values of pulse duty cycle for wider generality of this work, although many of the pulsed radars deployed in practice use relatively small values of duty cycle, e.g., 0.1-10 %. It is straightforward that higher pulse duty cycle yields greater outperformance of PSUN over the case without PSUN. Also, similar to the results with EbNo above, performance advantage gets greater as the modulation order becomes higher.

Figure 4.11 illustrates the number of received bits per second versus the probability that an OFDM symbol is hit by a radar pulse, ρ. When $\rho = 0$, the performance must be the same between the cases with and without PSUN since PSUN does not allocate null subcarriers when no OFDM symbol is radar-interfered. As explained in Section 4.3.2, a greater value of ρ yields a smaller number of received bits per second. Similar to the discussion of pulse duty cycle in Figure 4.10, a greater value of ρ indicates a more severe situation of radar interference. Due to this, it still holds true that outperformance of PSUN increases as ρ becomes greater. The performance curve drops faster in 64-QAM than 16-QAM, which implies that a higher-order modulation is more sensitive to radar interference. Nevertheless, performance advantage of PSUN gets greater as the modulation order gets higher.

Pulse Prediction Errors

So far we have seen the performances assuming *perfect pulse prediction*. The results shown through Figs. 4.12 and 4.13 depict how the performance of an OFDM system is deteriorated with *imperfect pulse prediction*. Figure 4.12 shows the number of received bits per second versus the probability of false alarm, P_{fa}. It is straightforward that a higher P_{fa} decreases the number of received bits per second of an OFDM system employing PSUN, while the case without PSUN stays unrelated to the level of P_{fa}. The reason is that with a false alarm, an OFDM symbol is protected by PSUN instead of channel coding, but in fact it undergoes an AWGN channel where channel coding is a more effective protection than PSUN.

Figure 4.13 shows the number of received bits per second versus the probability of missed detection, P_m. As explained earlier in Section 4.5, at an OFDM TX applying PSUN, a missed detection is translated as a situation where an OFDM symbol is not predicted to be radar-interfered hence not precoded with PSUN, but in fact hit by a radar pulse. In other words, the particular symbol is equipped with channel coding instead of PSUN, and hence contributes to degradation of performance. The performance degradation of an OFDM RX without PSUN is shown by the gap at zero P_m. As P_m increases, the performance of PSUN gets closer to the case without PSUN. The performance advantage of PSUN increases as the modulation order gets higher.

4.7 Feasibility of 5G Applications Using 3.5 GHz LTE with PSUN

The 5th generation mobile networks (5G) will operate in a highly heterogeneous environment characterized by the existence of multiple types of access technologies over multiple chunks of spectrum bands. In other words, enabling 5G use cases and business models requires the allocation of additional spectrum for mobile broadband and needs to be supported by flexible spectrum management capabilities. Based on the analyses and results of this chapter, we suggest that the 3.5 GHz Band can be a usable additional spectrum for enabling LTE to support several functionalities of 5G technologies.

We refer to a white paper [122] issued by the Next Generation Mobile Networks (NGMN), a mobile telecommunications association of mobile operators, vendors, manufacturers and research institutes, for understanding the representative example use cases of 5G and the corresponding requirement of data rate for each use case. A consistent user experience with respect to throughput needs a minimum data rate guaranteed everywhere. *The data rate requirement of a use case is set as the minimum user experienced data rate required for the user to have a quality experience of the targeted use case.* The use cases are summarized in Table 4.5.

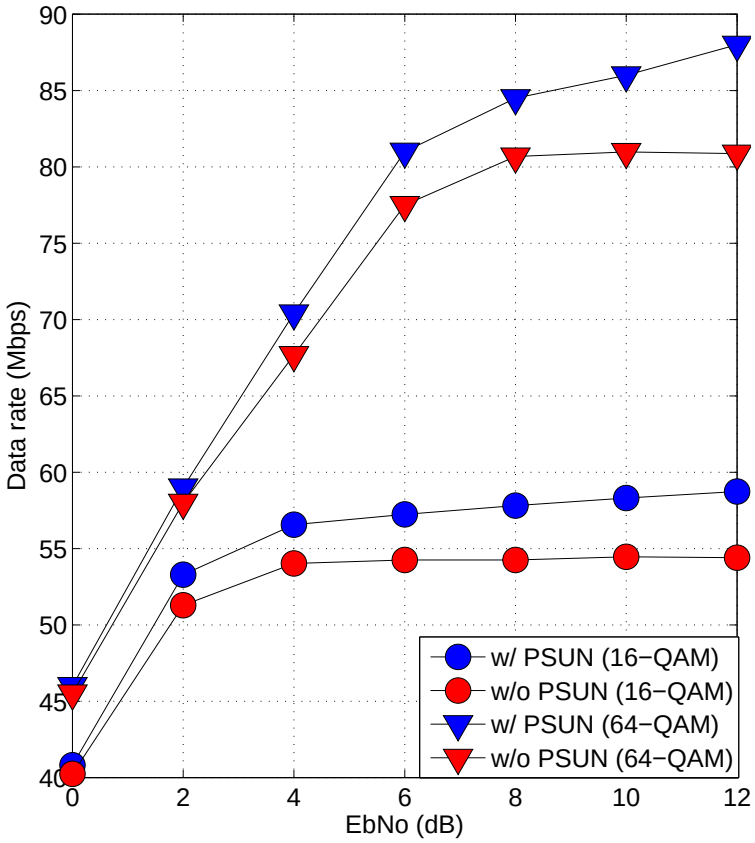

Figure 4.9: Data rate vs. EbNo ($\rho = 0.8$, Duty cycle $= 0.1$)

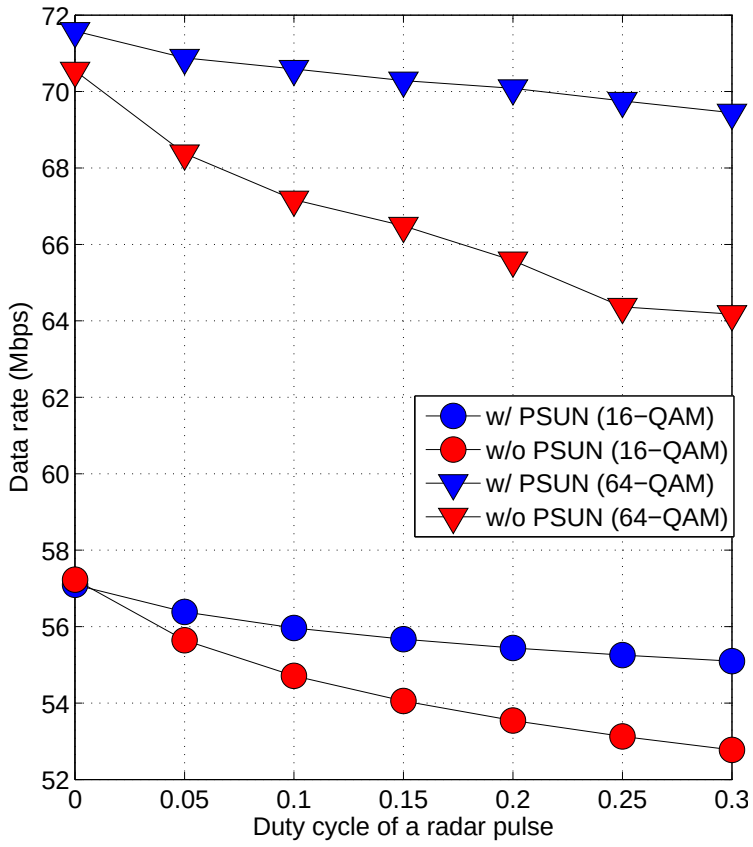

Figure 4.10: Data rate vs. Duty cycle (EbNo = 4 dB, $\rho = 0.8$)

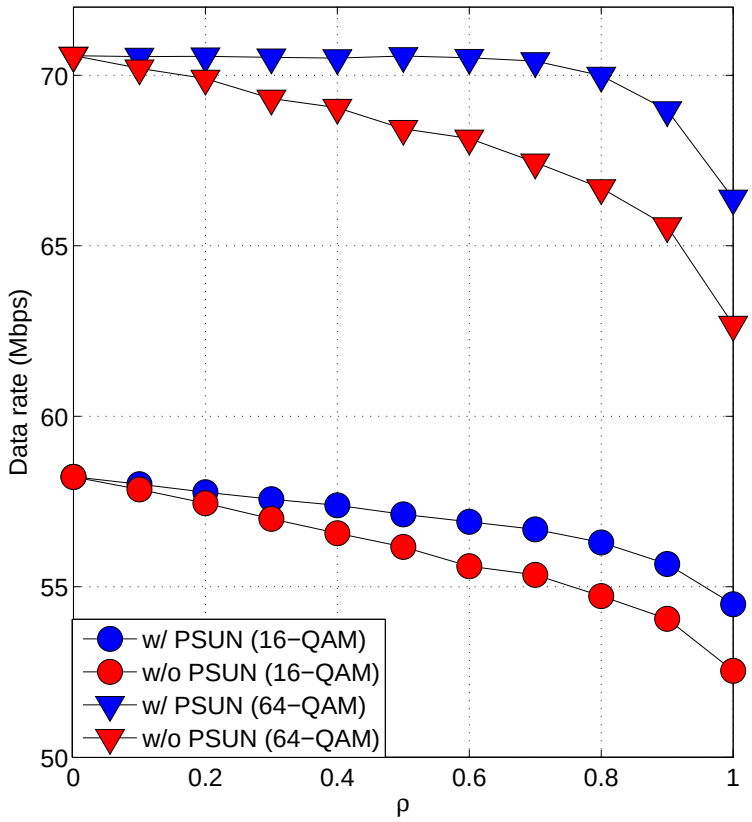

Figure 4.11: Data rate vs. ρ (EbNo = 4 dB, Duty cycle = 0.1)

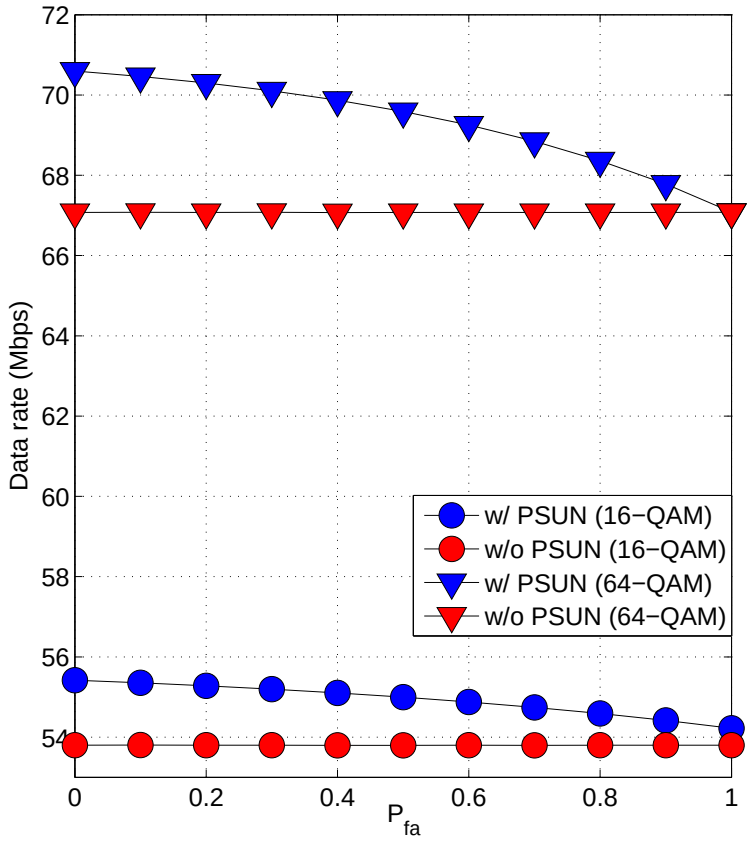

Figure 4.12: Data rate vs. P_{fa} (Duty cycle = 0.1, $\rho = 0.8$, EbNo = 4 dB)

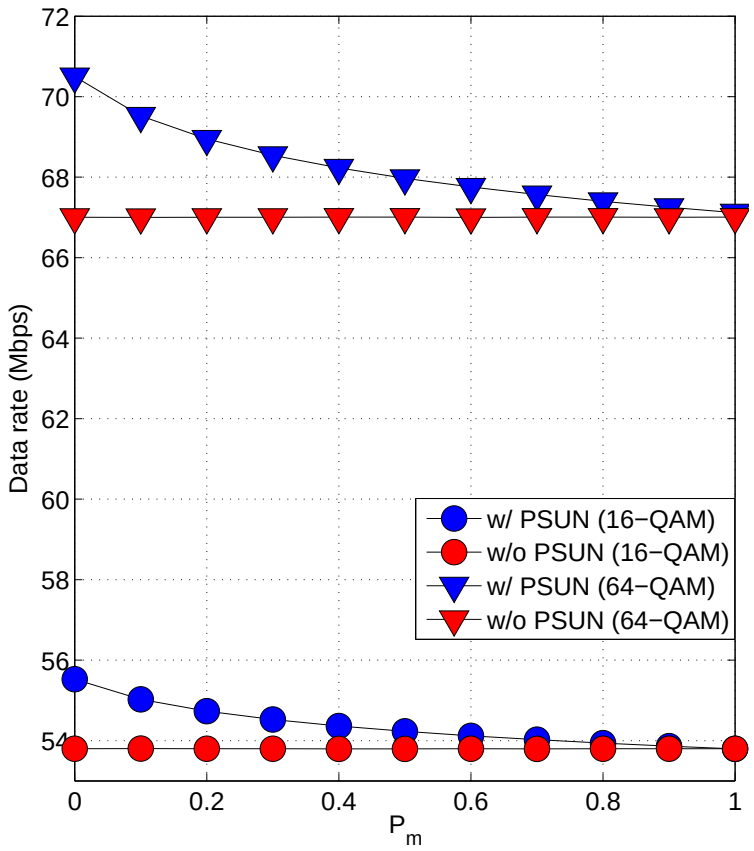

Figure 4.13: Data rate vs. P_m (Duty cycle = 0.1, $\rho = 0.8$, EbNo = 4 dB)

Table 4.5: Data rate requirements for use cases of 5G [122]

Use case	**Data rate requirement (Downlink/Uplink)**
Candidates for LTE with PSUN	
Massive low-cost/long-range/low-power M2M	1-100 kbps
Resilience and traffic surge	0.1-1 Mbps / 0.1-1 Mbps
Ultra-high reliability & Ultra-low latency	50 kbps to 10 Mbps / a few kbps to 10 Mbps
Ultra-high availability & reliability	10 Mbps / 10 Mbps
Airplanes connectivity	15 Mbps / 7.5 Mbps
Broadband access in a crowd	25 Mbps / 50 Mbps
50+ Mbps everywhere	50 Mbps / 25 Mbps
Ultra-low latency	50 Mbps / 25 Mbps
Others	
Broadband like services	Up to 200 Mbps / Modest (e..g, 500 kbps)
Ultra-low cost broadband access	300 Mbps / 50 Mbps
Mobile broadband in vehicles	300 Mbps / 50 Mbps
Broadband access in dense areas	300 Mbps / 50 Mbps
Indoor ultra-high broadband access	1 Gbps / 500 Mbps

According to our results, LTE with PSUN can fulfill the *downlink* requirements of several use cases which are listed under the category of "Candidates for LTE with PSUN" in Table 4.5. While most of the requirements of the selected use cases are set to be 50 Mbps, our results, Figs. 4.9 through 4.13, indicate that LTE with PSUN is capable of supporting data rates that are higher than 50 Mbps and 40 Mbps with 64-QAM and 16-QAM, respectively. For example, observing Figure 4.9, the required EbNo values for achieving the data rate of 50 Mbps are 0 and 1 dB for 64-QAM and 16-QAM, respectively.

It is discussed in [79][80] that although average data rate is roughly the same for all file sizes, because of interruptions as a radar rotates, average received data rate for smaller files may vary depending on when the transmission begins relative to the radar's rotation cycle. This effect does not occur during transmission of larger files that span one or more rotation periods of the radar. The authors suggested several appropriate applications that can tolerate interruptions from a pulsed radar: video on demand, peer-to-peer file sharing, and automatic meter reading, or applications that transfer large enough files so the fluctuations are not noticeable, such as song transfers. Among these applications, a white paper that analyzed the mobile traffic pattern of 2015 [123] finds a direction that LTE with PSUN can target in the 3.5 GHz Band. It says that *mobile video traffic* accounted for 55% of total mobile data traffic in 2015. Mobile video traffic now accounts for more than half of all mobile data traffic. It will be very promising if LTE with PSUN can support video traffic in the 3.5 GHz Band while coexisting with military radar.

4.8 Chapter Summary

This chapter proposes PSUN, an OFDM transmission scheme enabling an LTE system to coexist with federal military radars in the 3.5 GHz Band. The scheme is comprised of PB at an RX and precoding of null subcarriers at a TX of an OFDM system. To maximize data rate, an OFDM TX employing PSUN (i) localizes OFDM symbols to be radar-interfered a priori, and (ii) shifts redundancy from channel coding to subcarriers in the OFDM symbols. This chapter considers existence of sensing functionality in the 3.5 GHz Band coexistence architecture, and hence impacts of imperfect sensing which can occur due to a sensing error by an ESC and parameter changes by a radar. Results show that PSUN is still effective in suppressing ICI remaining after PB even with imperfect pulse prediction, and as a result enables an LTE system to support various use cases of 5G that require the data rate lower than 50 Mbps in the downlink and relatively larger file size such as video streaming.

Chapter 5

DSRC-Wi-Fi Coexistence at 5.9 GHz

This chapter discusses coexistence of DSRC and IEEE 802.11ac-based Wi-Fi at 5.9 GHz. It (i) proposes a novel method that accurately evaluates the performance of a broadcast-based vehicular network, and (ii) characterizes the coexistence between DSRC and IEEE 802.11ac in the 5.850-5.925 GHz (5.9 GHz) band, by using the proposed method.

More specifically, this work provides a higher accuracy in analysis of a broadcast-based vehicular communications system, by introducing a geometric analysis framework. The key idea is soft evaluation of a failed packet transmission. This method takes a geometric point of view, where a packet that is said to be failed by typical performance metrics–such as packet delivery rate (PDR), delay, etc.–can still be received by certain receiver vehicles. For instance, suppose that a packet sent from a transmitter vehicle is collided with a packet sent from another vehicle. It can still be received by the vehicles in the other part of transmission range of the transmitter vehicle (see Fig. 5.1). We found that this unique characteristic of a broadcast-based vehicular network leads such typical performance metrics to inaccurate performance evaluation. They make a binary decision on a packet reception, i.e., a success or a failure, which cannot display such partial possibility of packet reception. Whereas, the metric that this chapter proposes can still measure such partial possibility and take it into calculation of the performance of a broadcast-based vehicular communications network.

Moreover, this chapter applies the novel performance evaluation method to characterization of the coexistence between vehicular communications and Wi-Fi. Based on the proposed metric, our results demonstrate the impacts of external interference from IEEE 802.11ac into DSRC, with respect to inter-broadcast time (IBI) and contention window (CW). Regarding the coexistence issue, effort of the IEEE's Tiger Team has finished but the resulting channelization methods are not being taken very promising by the Wi-Fi and automotive industries. We believe that thanks to the higher accuracy in measurement of a broadcast-based vehicular network, our results higher impacts in suggestion of future channelization method for the coexistence problem.

5.1 Related Work

In August 2015, the United States Department of Transportation (DoT) released a test plan [128] that described tests to characterize the coexistence of Dedicated Short Range Communications (DSRC) and unlicensed devices in the 5.850-5.925 GHz (5.9 GHz) band. As suggested by the Congress in September 2015, the Federal Communications Commission (FCC), in its latest public notice [129], now seeks to refresh the record of its pending 5.9 GHz rulemaking to provide potential sharing solutions between Wi-Fi and DSRC at 5.9 GHz.

Wi-Fi provides short-range, high-speed unlicensed wireless connections in the 5 GHz band for applications such as Wi-Fi-enabled radio local networks by wireless internet providers. DSRC uses short-range wireless communication links to facilitate information transfer for vehicle to infrastructure (V2I) and vehicle to vehicle (V2V), based on IEEE 802.11p for its PHY and MAC layers. The current focus of the FCC's solicitation in [129] is two-fold: (i) prototype of interference-avoiding devices for testing; (ii) test plans to evaluate electromagnetic compatibility of unlicensed devices and DSRC.

Recent work discusses coexistence between DSRC system and Wi-Fi [130]-[134]. Especially in [134], results of experiments and simulations suggest a method of allocating channels for DSRC and Wi-Fi. However, despite the thorough study, the implication of the results is uncertain; there is too high discrepancy between the experimental and simulation results.

This leads to a conclusion that we need a method to accurately describe the performance of a DSRC network, to accomplish the coexistence test plans solicited in [129]. Another recent study [135] provides an extensive analysis for a DSRC network, yet it lacks consideration of DSRC-Wi-Fi coexistence. Moreover, we found that using the current metrics makes it difficult to assess precisely the performance of a DSRC network. The main objective of DSRC networking is to support safety-critical applications that utilize a functionality called basic safety message (BSM). BSMs are periodically broadcast from a vehicle, which necessitates a unique metric to compute the network-wise performance. Many of the prior studies such as [136]-[141] rely on the typical metrics that only myopically capture the broadcast nature of DSRC networks, i.e., packet delivery rate (PDR) and packet delay/latency.

An advanced metric that addresses this problem is proposed in [142], namely inter-reception time (IRT). The typical packet latency is defined as the time spent by a successful packet to travel from its source to final destination. But this is not adequate to capture the performance of broadcast-based safety applications since latency is measured only for successful packets, i.e. a latency does not capture the impact of packet losses and collisions on the latency perceived by applications that are based on periodic broadcast of packets. Defined as the time elapsed between two successive successful receptions of packets broadcast by a specific transmitter (TX) at a certain vehicle, IRT can more accurately display the performance of a BSM-based safety-critical application on a DSRC network.

However, IRT still shows shortcomings. Limitations of IRT are highlighted when taking a

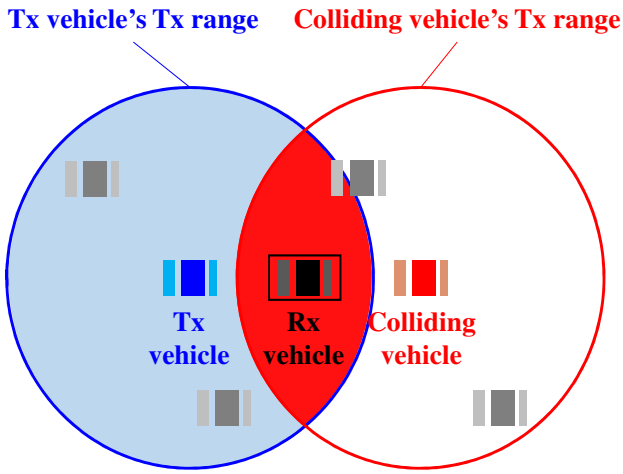

Figure 5.1: Geometric analysis of a broadcast-based vehicular network

geometric view to a broadcast-based vehicular network, as depicted in Fig. 5.1. For instance, when a packet is transmitted from a TX vehicle, all the vehicles located in the transmission range of it become potential receivers (RXs). When a packet collides with a packet from another vehicle that is at the "left" side of the TX vehicle, the vehicles that are located at the "right" side are still able to receive the packet without corruption. This geometric insight cannot be captured using the aforementioned classical metrics.

A one-dimensional geometric analysis is provided in [144]. However, we extend the framework to a two-dimensional space, and proposes a metric that can capture partial receptions when a packet is collided. More importantly, this work has a clear contribution to addressing the 5.9 GHz coexistence problem. We apply the proposed metric for suggesting proper values of MAC parameters when DSRC coexists with Wi-Fi–namely IBI and CW.

5.2 Main Contributions

In this chapter, a new metric is proposed that provides a geometric point of view to measure the performance of a broadcast-based application on a DSRC network. Based on this new method, we characterize DSRC-Wi-Fi coexistence. The contributions of this chapter can be articulated as:

1. This chapter proposes a novel metric that evaluates the performance of a broadcast-based DSRC network. The main advantage of our new method is that it can illustrate a wider perspective while the typical metrics provide only myopic observation at a RX. Considering the broadcast nature, some RXs are still able to receive a packet from a

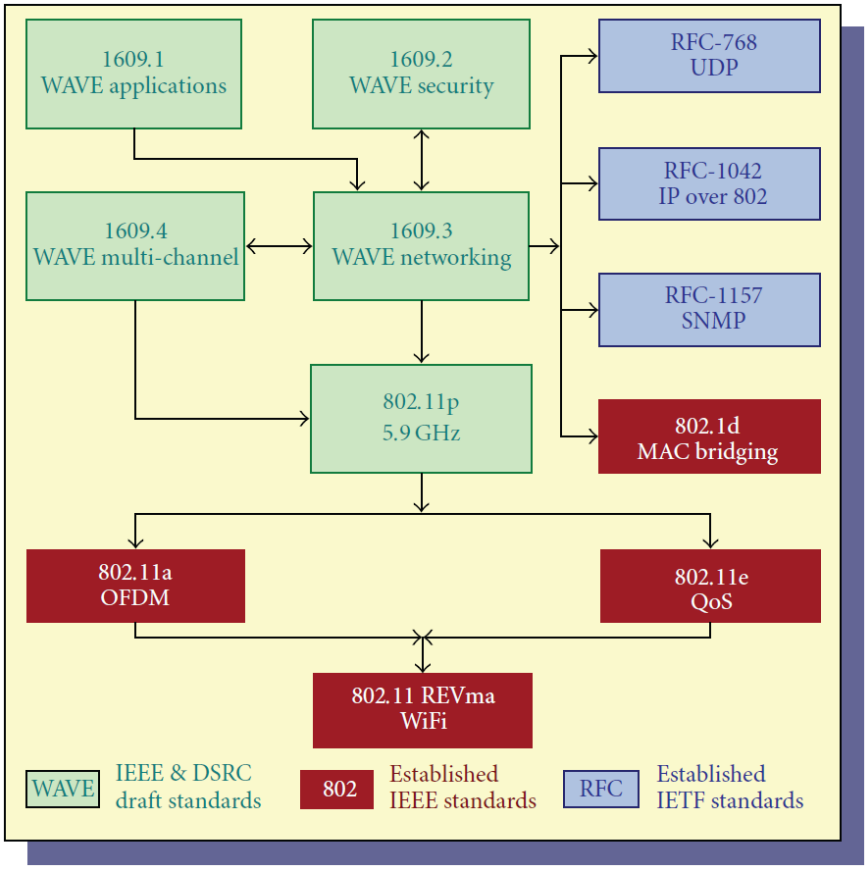

Figure 5.2: Architecture of the WAVE standard [124]

TX even if other RXs are not. The new metric can count such partial possibility of packet reception, which leads to a more rigorous analysis

2. Considering that a significant challenge that DSRC faces is co-channel coexistence with Wi-Fi, we apply the novel performance metric to characterization of DSRC-Wi-Fi coexistence. The results suggest adequate selection of IBI and CW values to improve the performance of a broadcast-based safety-critical application.

5.3 Technical Background on DSRC

From a layered perspective, wireless communication between DSRC devices uses IEEE 802.11 and 802.11p standards as a lower layer close to the physical layer. The DSRC MAC layer uses IEEE WAVE standards which follows IEEE 1609.x standards. Then the higher layers employ IPv6 and other common protocol stacks such as Transfer Control Protocol (TCP) and User Datagram Protocol (UDP) for instance. This structure is illustrated in Figure 5.2.

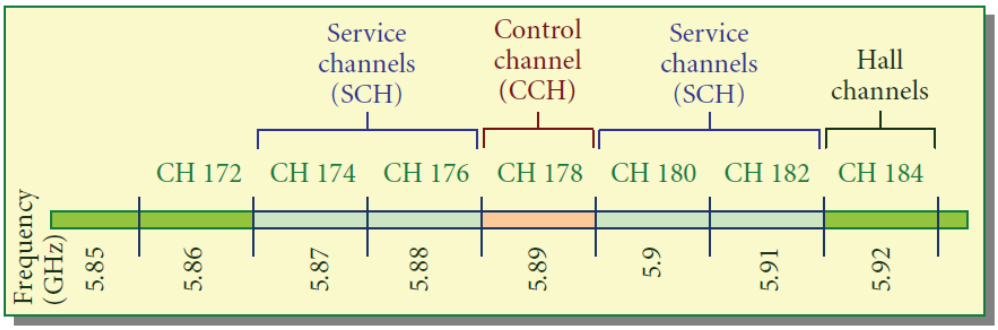

Figure 5.3: Channel map of the 5.9 GHz Band [124]

One of the biggest challenges when dealing with a suite of standards is the understanding of the functionalities of each standard and how multiple standards fit together to perform a homogeneous task. The term DSRC is typically used as an umbrella term that refers to the suite of standards shown in Figure 5.2. One important thing is that since 802.11p depends ultimately on 802.11, DSRC also relies on CSMA/CA for its MAC. In other words, DSRC standards suite relies on the CSMA/CA mechanism to mitigate the hidden/exposed node problems.

DSRC is a wireless communications technology that operates at the 5.9 GHz Band (5.850-5.925 GHz) and supports communications among OBUs and RSUs. The 5.9-GHz DSRC spectrum consists of seven 10-MHz channels. As illustrated in Figure 5.3, channel 178 is the control channel (CCH) while the other six channels are assumed to be service channels (SCHs).

As a general rule, CCH (178) is exclusively used to communicate safety and control information while SCH is typically used to communicate IP-based services. Consequently, each communication zone must utilize channel 178 (CCH) as a CCH used for safety messages, then, it may utilize one or more SCH of the available four service channels. Devices initiating WAVE Basic Service Set (WBSS) are encouraged to avoid using the same SCHs selected by immediate neighbors.

The WAVE relies on the IEEE 802.11a Orthogonal Frequency Division Multiplexing (OFDM) mechanism to provide data transmission rates of 9, 12, 18, 24, and 27Mbps for 0-60Km/hour vehicle speed and 3, 4.5, 6, 9, and 12Mbps for 60-120 Km/hour vehicle speed. The system comprises 52 subcarriers, modulated using BPSK, QPSK, 16-QAM, or 64-QAM. Convolution coding is used with a coding rate of 1/2, 2/3, or 3/4. The data rates are determined by coding rate and modulation type [126]-[127].

The DSRC divides channels into 10 MHz rather than the 22 MHz as designed in the IEEE 802.11. DSRC squeezes each channel bandwidth as indicated in the IEEE 802.11p [125], and then imposes a higher level management scheme. The scheme insures that the operating SCH in any vicinity is different from the operating SCH in any of the adjacent vicinities.

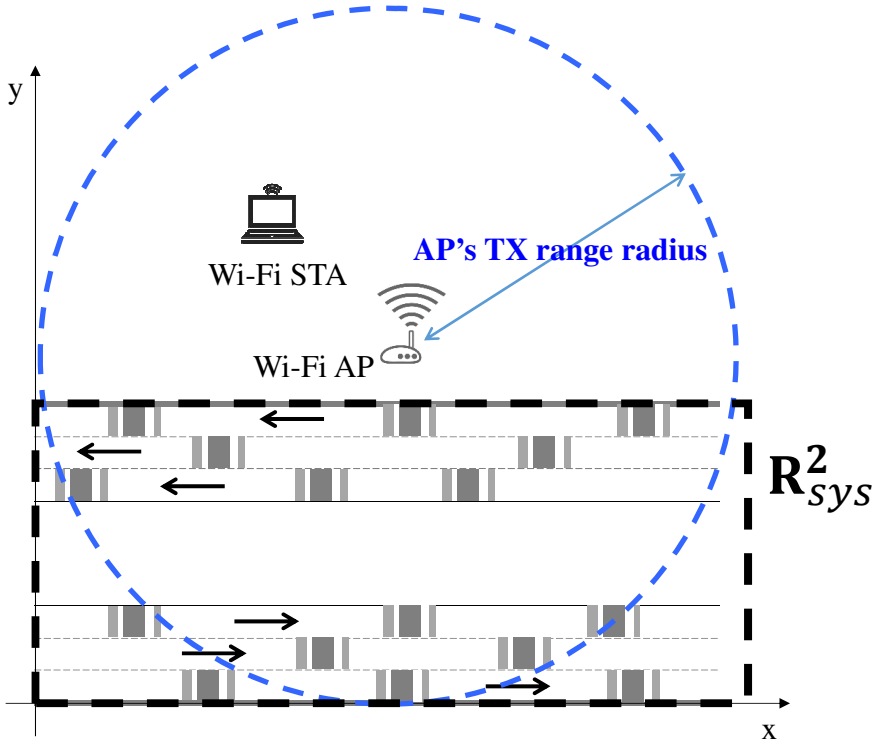

Figure 5.4: Geometry of the simulation environment

This management scheme mitigates the potential for interference between channels.

5.4 System Model

Fig. 5.4 illustrates the environment that comprises a 6-lane, 1000-meter (m) road with a dividing strip of 5 m between the two sides (the upper side for right-to-left and the lower side for left-to-right direction). There is one Wi-Fi pair of an access point (AP) and a station (STA), above the upper side of the road. The AP acts as the transmitter, and is 300 m apart from the road upper end; the main idea is to set the transmission range to reach the lower end of the road. The distance between the Wi-Fi TX and RX is 100 m.

A snapshot of DSRC-Wi-Fi coexistence geometry is illustrated in Fig. 5.4 in a Cartesian coordinate system. Position of the ith vehicle is formally written as $\mathtt{x}_i = (x_i, y_i) \in \mathbf{R}^2_{sys}$. Since the region $\mathbf{R}^2_{sys}$ is composed of 6 lanes, there are 6 values of y_i. For each lane, X axis ranges $x_i = [0, 1000]$, in which vehicles are distributed according to an independent and homogeneous one-dimensional Poisson Point Process (PPP) of intensity λ vehicles per 1000 m per lane. Note that for ease of analysis, we assume a homogeneous traffic in which each

lane has the same intensity of traffic. Thus, the numbers of vehicles distributed in $\mathbf{R}_{sys}^2$ that are provided in our results in Section 5.6 are given by 6λ. According to the uniformity property of a homogeneous point process [143], we can assume that the DSRC vehicles are uniformly randomly scattered in each lane with different values of λ and the corresponding velocities, the detailed values of which will be provided in Section 5.6.

There are four possible results of a packet transmission including *successful delivery (DLVY)*; *expiration (EXP)*; *synchronized transmission (SYNC)*; and *hidden node problem (HN)* [144]. A DLVY does not undergo either contention nor collision. Also, with a DLVY, we assume that every RX vehicle in a TX vehicle's transmission range successfully receives the packet. On the other hand, an EXP defines a situation where a packet is not even transmitted due to contention with other vehicles or a Wi-Fi TX.

There are two main types in a packet collision. A SYNC refers to a situation where more than one TXs start transmission at the same time due to the same value of backoff in CSMA/CA. On the other hand, a HN occurs in relation to carrier-sense threshold.

5.5 New Performance Evaluation Method

The three types of packet failure–EXP, SYNC, and HN–do not necessarily incur a lost message for all the RX vehicles in a TX vehicle's transmission range, r_{tx}. Based on that main idea, this section introduces a geometric method that precisely evaluates the performance of broadcast-based DSRC network.

We focus on the geometric analysis that can reflect a wider perspective on a network, than typical metrics' scopes that only gauge the performance of a certain TX-RX pair. We propose a new metric that more accurately displays reception of the broadcast packets and thus represents the performance of a vehicular network more accurately. The new metric, *Reception Geometry for Broadcast* (**RGB**) indicator, is defined at an arbitrary TX vehicle as

$$\begin{aligned}\mathsf{RGB} &= \frac{\text{Area where a packet can be received}}{\text{Area of the transmission range}} \\ &= \frac{\mathsf{A}_{rx}}{\pi r_{tx}^2}. \end{aligned} \tag{5.1}$$

As implied in (5.1), an **RGB** is a normalized quantity that is ranged [0,1]. For discussing computation of the value of a **RGB**, we start from DLVY and EXP since they are straightforward. As a DLVY does not undergo either contention nor collision, **RGB** is given by

$$\mathsf{A}_{rx} = \pi r_{tx}^2 \Rightarrow \mathsf{RGB}_{dlvy} = 1. \tag{5.2}$$

On the other hand, **RGB** for an EXP is given by

$$\mathsf{A}_{rx} = 0 \Rightarrow \mathsf{RGB}_{exp} = 0. \tag{5.3}$$

The reason is, a TX vehicle cannot even start transmission once it gets backed off by a contention with other TXs in the carrier-sensing range. As of no transmission, there is no RX vehicle in the network that can receive the packet.

Interestingly, an **RGB** is evaluated differently between SYNC and HN. Explanation of the rationale refers to the stochastic geometry that was discussed in Section 5.4. The geometry is illustrated in Fig. 5.5. A SYNC occurs when a colliding TX is in the carrier-sense range of a TX but they are assigned the same value of backoff. More specifically, as in Fig. 5.5, A_{rx} of an r_{tx} is determined as the "rest" of the intersection of two circles of transmission ranges of the TX and colliding TXs, which is given by

$$\begin{aligned}
&\mathsf{A}_{rx}\left(\mathsf{d}\left(\mathtt{x}_T,\mathtt{x}_C\right)\right)\\
&=\mathsf{A}_{tx}-\mathsf{A}_{col}\left(\mathsf{d}\left(\mathtt{x}_T,\mathtt{x}_C\right)\right)\\
&=\pi r_{tx}^2-\left(2r_{tx}^2\cos^{-1}\left(\frac{\mathsf{d}\left(\mathtt{x}_T,\mathtt{x}_C\right)}{2r_{tx}}\right)\right.\\
&\qquad\left.-\frac{\mathsf{d}\left(\mathtt{x}_T,\mathtt{x}_C\right)}{2}\sqrt{4r_{tx}^2-\mathsf{d}^2\left(\mathtt{x}_T,\mathtt{x}_C\right)}\right)
\end{aligned}\tag{5.4}$$

where A_{col} denotes the collision area and is given by $\mathsf{A}_{col}=\mathsf{A}_{tx}-\mathsf{A}_{rx}$; $\mathtt{x}_T$ and $\mathtt{x}_C$ are the positions of the TX and colliding TXs, respectively; r_{tx} is the transmission range of a vehicle. The distance between the TX vehicle and the colliding TX is defined as a function of positions $\mathtt{x}_T$ and $\mathtt{x}_C$ as

$$d_{avg}\le\mathsf{d}\left(\mathtt{x}_T,\mathtt{x}_C\right)\le r_{cs}.\tag{5.5}$$

As Fig. 5.5a shows, a $\min\mathsf{A}_{rx}$ occurs with $\max\mathsf{d}\left(\mathtt{x}_T,\mathtt{x}_C\right)$; a colliding TX is placed at the border of the TX vehicle's carrier-sense range. In contrast, as in Fig. 5.5b, a $\max\mathsf{A}_{rx}$ occurs with $\min\mathsf{d}\left(\mathtt{x}_T,\mathtt{x}_C\right)$. Since infinitely many cases are possible for $\min d$, we consider d_{avg}, the average value of inter-vehicle distance, to be the minimum separation between two arbitrary vehicles. This yields the **RGB** for a SYNC in $\mathbf{R}_{sys}^2$ as

$$\frac{\mathsf{A}_{rx}\left(d_{avg}\right)}{\pi r_{tx}^2}\le\mathbf{RGB}_{sync}\left(\mathtt{x}_T,\mathtt{x}_C\right)\le\frac{\mathsf{A}_{rx}\left(r_{cs}\right)}{\pi r_{tx}^2}.\tag{5.6}$$

Now, the **RGB** for a HN can be formulated in a similar logic to (5.4)-(5.6). While the way to obtain A_{rx} refers to (5.4), $\mathsf{d}\left(\mathtt{x}_T,\mathtt{x}_C\right)$ is computed in a different way as

$$r_{cs}<\mathsf{d}\left(\mathtt{x}_T,\mathtt{x}_C\right)<2r_{cs}.\tag{5.7}$$

A $\max\mathsf{d}\left(\mathtt{x}_T,\mathtt{x}_C\right)$ causing $\min\mathsf{A}_{rx}$ occurs when the r_{tx}'s of the TX and the colliding TX contact at the border. A $\min\mathsf{d}\left(\mathtt{x}_T,\mathtt{x}_C\right)$ yielding $\max\mathsf{A}_{rx}$ occurs when the colliding TX is right outside of r_{tx} of the TX vehicle. This yields the **RGB** for a HN defined in $\mathbf{R}_{sys}^2$ as

$$\frac{\mathsf{A}_{rx}\left(r_{cs}\right)}{\pi r_{tx}^2}\le\mathbf{RGB}_{hn}\left(\mathtt{x}_T,\mathtt{x}_C\right)\le\frac{\mathsf{A}_{rx}\left(2r_{cs}\right)}{\pi r_{tx}^2}.\tag{5.8}$$

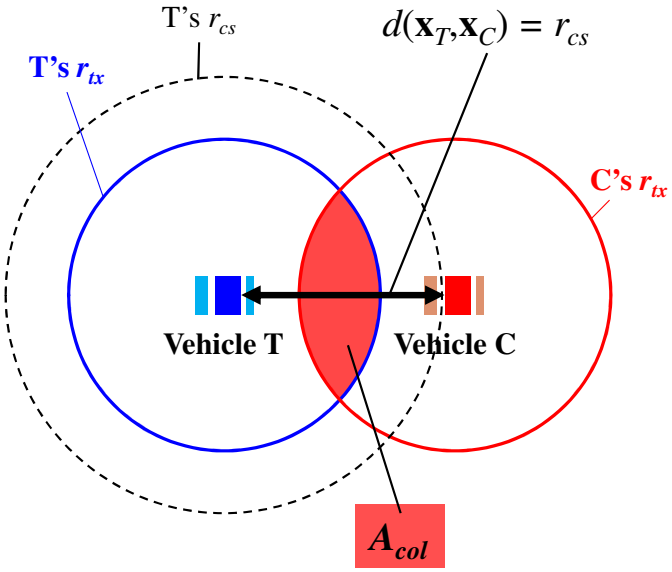

(a) Minimum A_{rx}

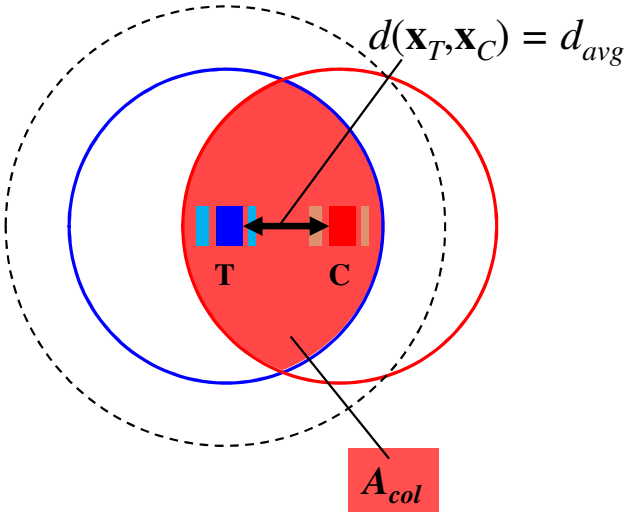

(b) Maximum A_{rx}

Figure 5.5: Geometry of intersection for SYNC

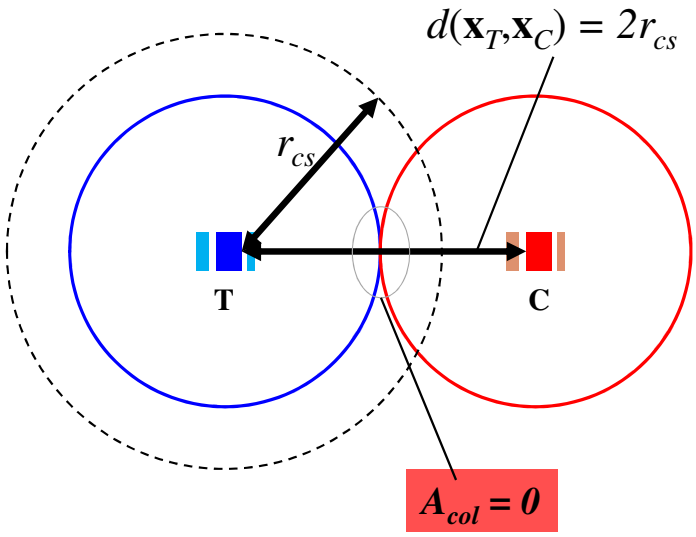

(a) Minimum A_{rx}

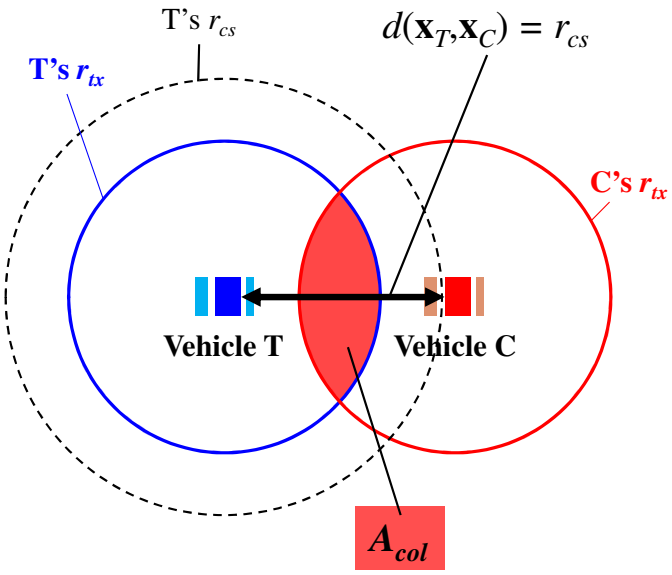

(b) Maximum A_{rx}

Figure 5.6: Geometry of intersection for HN

Table 5.1: Parameters

Parameter	**Value**
Road	
Length of the road	1000 m
Number of lanes	6
Lane width	4 m
Dividing strip width	5 m
DSRC	
Number of vehicles in $\mathbf{R}^2_{sys}$ $(= 6\lambda)$	{30,120,210,270}
Inter-vehicle distance	{200, 50, 28.57, 22.22} m
Velocity	{42.07, 17.49, 11.93, 9.72} m/sec
Receiver sensitivity	-91 dBm
Transmission antenna gain	0 dBm
Packet length	500 bytes
Data rate	6 Mbps
Slot time	13 μs
Wi-Fi	
Receiver sensitivity	-82 dBm
Transmission power	30 dBm
CW Size	[15,1023]
Packet length	10,800 bytes
Data rate	54 Mbps
Slot time	9 μs

Finally, one can obtain a *mean* $\mathbf{RGB}$ that is averaged over (i) all the packets transmitted by a TX vehicle within a unit time, (ii) all the possible positions of the TX vehicle, and (iii) all the possible positions of the RX vehicles, which is given by

$$\overline{\mathbf{RGB}} = \frac{1}{\left|\mathbf{R}^2_{sys}\right|^2} \int_{\mathtt{x}_T \in \mathbf{R}^2_{sys}} \int_{\mathtt{x}_C \in \mathbf{R}^2_{sys}} \sum_{k=1}^{N_{pkt}} \sum_{j \in \mathcal{S}_{pb}} \mathbf{RGB}_{k,j}\left(\mathtt{x}_T, \mathtt{x}_C\right) \mathsf{P}_{k,j} d\mathtt{x}_T d\mathtt{x}_C \tag{5.9}$$

where N_{pkt} is the number of packets that are generated in a unit time; $\mathcal{S}_{pb}$ denotes the set of the four possible results of a packet transmission, $\mathcal{S}_{pb} = \{\text{DLVY, EXP, SYNC, HN}\}$; $\mathbf{RGB}_{k,j}$ denotes each of (5.2), (5.3), (5.6), and (5.8) for the kth packet; $\mathsf{P}_{k,j}$ denotes the probability that each of $\mathcal{S}_{pb}$ occurs.

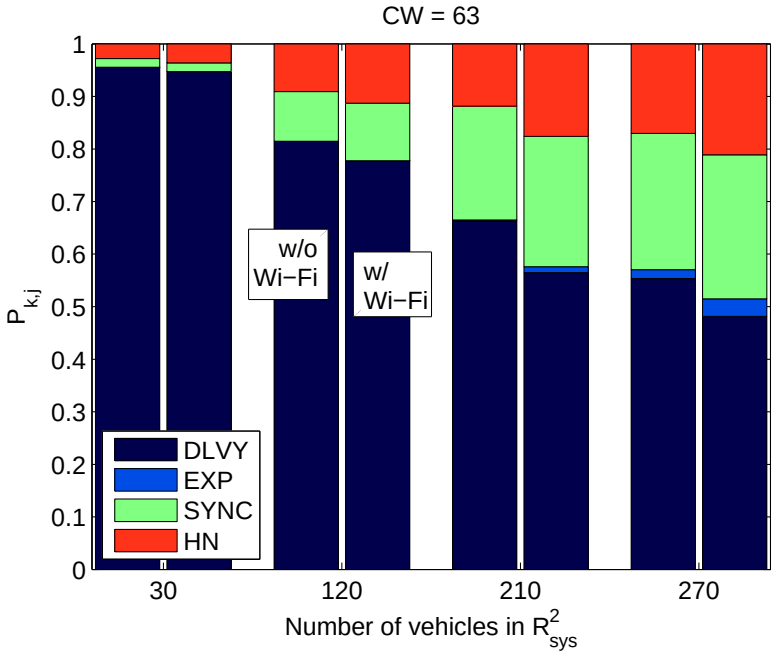

(a) With CW = 63

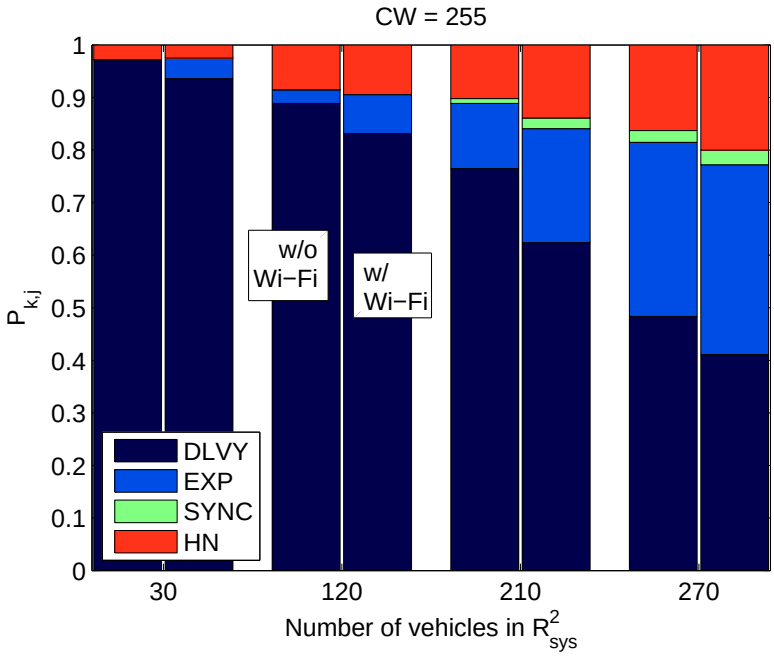

(b) With CW = 255

Figure 5.7: $P_{j,k}$ according to vehicle density

5.6 Performance Evaluation

We evaluate the performance of a DSRC-based vehicular network through the *network simulator 2 (ns-2)*. The simulation topology refers to Fig. 5.4. Each result is an average from 180 runs of 20-second experiments on *ns-2*, based on the settings described in Table 5.1. The 180 runs are composed of 30 runs for each of the 6 lanes, in order to remove bias that could occur if not all lanes were considered.

5.6.1 Setting

As mentioned in Section 5.4, the DSRC vehicles are uniformly randomly distributed on the road. Their mobility setting is also summarized in Table 5.1. The total number of vehicles situated in an entire region $\mathbf{R}_{sys}^2$ is the number of lanes multiplied by the number of vehicles per lane, 6λ. Inter-vehicle distance is obtained by $\lambda/(\text{Road length}) = \lambda/1000$. The inter-vehicle distance accordingly determines the vehicle velocity. A set of empirical data [145] matches the velocity with the minimum inter-vehicle distance required for avoiding a collision. Since the data set was a discrete matrix that omitted some values that we needed, we fitted the data using MATLAB based on a fitting technique called *shape-preserving fitter*. The resulting values of velocities were used in the *ns-2* experiments.

To display the three types of packet failure–EXP, SYNC, and HN, we modified the C++ stack of the *ns-2*. More specifically, we modified the packet trace function inside the stack in such a way that a colliding packet is declared to be HN/SYNC if the TX of the colliding packet is outside/within the TX range of a vehicle, respectively.

5.6.2 Results

The results provide the values of $\mathsf{P}_{j,k}$ and $\mathbf{RGB}_{j,k}$ that are given in (5.9).

Computation of $\mathsf{P}_{j,k}$

Fig. 5.7 demonstrates $\mathsf{P}_{j,k}$ for each of DLVY, EXP, SYNC, and HN, according to CW and presence of Wi-Fi TX. There are two bars at each value of the X-axis. The left and right bars indicate the results with and without interference from Wi-Fi. Note that comparison of Fig. 5.7 to Figs. 3 through 5 in [144] validates our results. However, this chapter provides a novel perspective of measuring the performance of a DSRC broadcast network because our metric, **RGB**, accurately reflects impact of the delicate geometry of a packet delivery on a generic two-dimensional space.

Note that two representative values of CW are selected: 63 and 255. First, CW = 63 is chosen

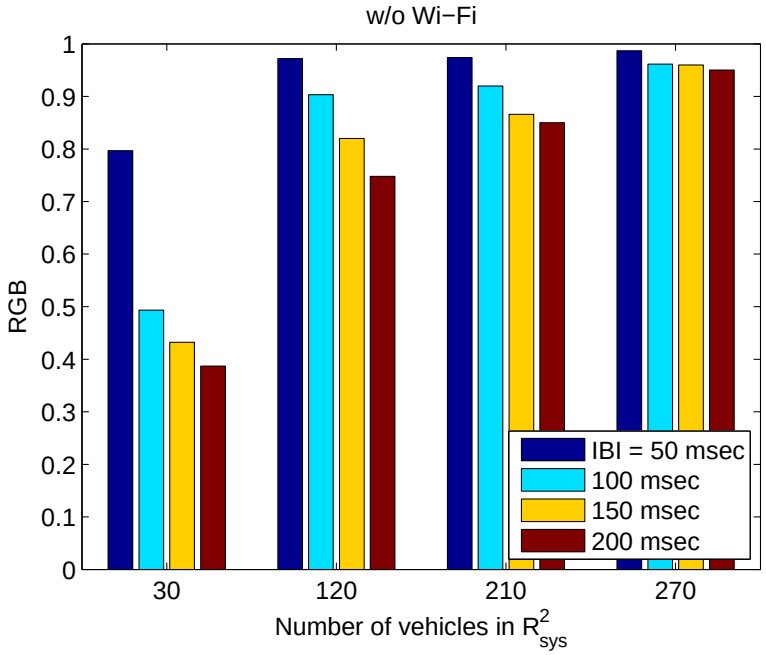

(a) Without interference from Wi-Fi

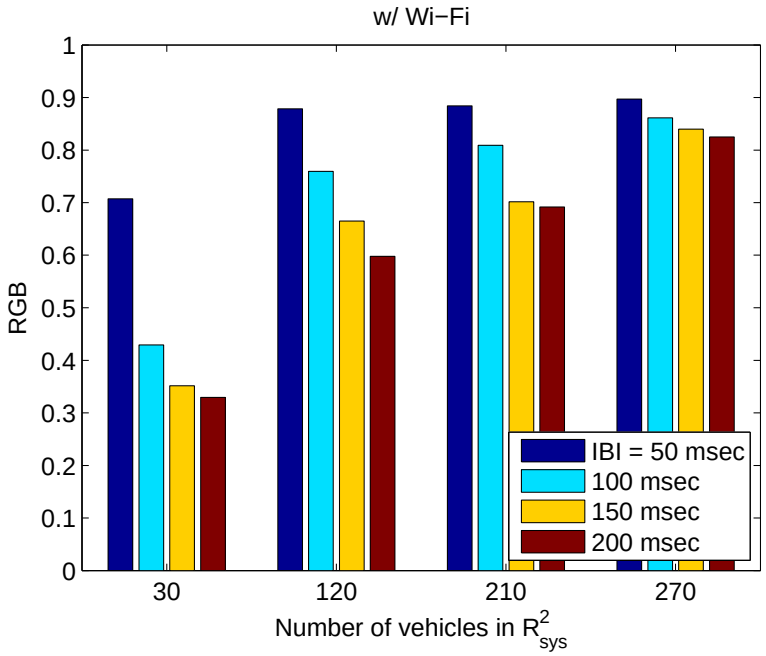

(b) With interference from Wi-Fi

Figure 5.8: **RGB** according to IBI

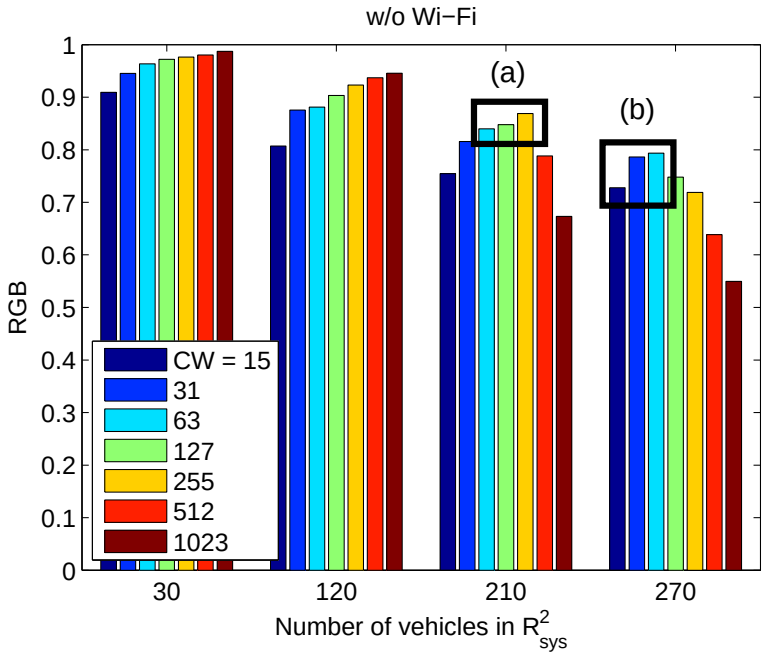

(a) Without interference from Wi-Fi

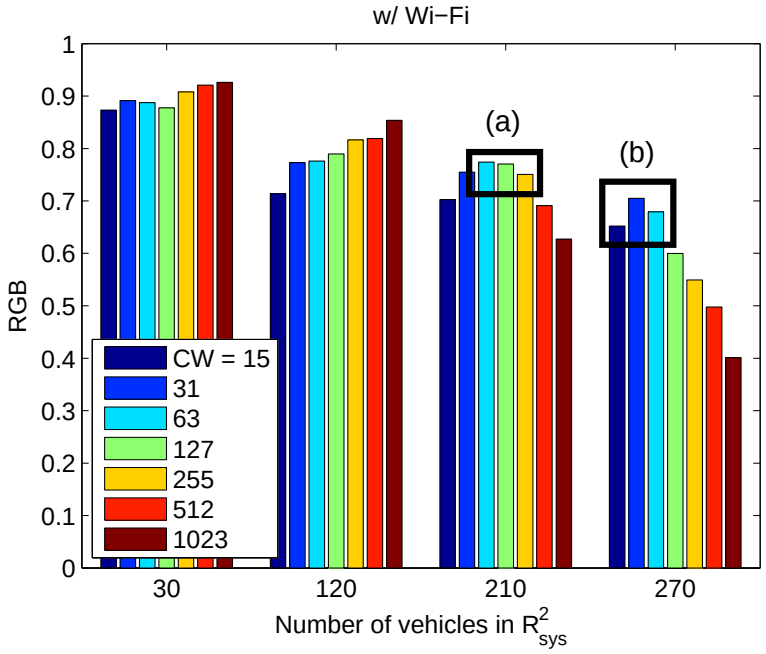

(b) With interference from Wi-Fi

Figure 5.9: **RGB** according to CW

since it is a proper value to highlight impact of presence of Wi-Fi interference in a balanced manner among SYNC and HN. We found that smaller values of CW did not highlight impact on HN due to too many SYNCs. Also, selection of CW = 255 is to compare impact of a larger CW. In fact, Fig. 5.7b shows dramatic increase in EXP and decrease in SYNC.

Two important observations need to be made. First, EXP increases with a larger value of CW, higher traffic density, and presence of Wi-Fi TX. Second, SYNC increases with higher traffic density and presence of Wi-Fi TX, but decreases as CW increases. The reason is that now there are wider choice of CW values for DSRC TXs and as a result P_{sync} gets smaller. Third, HN does not show a clear pattern according to CW, but increases as traffic density increases and as Wi-Fi TX is introduced. It implies that a nearby Wi-Fi TX acts as a hidden-node collider.

When it comes to safety-critical applications, very low latency is a significant factor that must be guaranteed in addition to the successful delivery of a BSM.

From Figs. 5.7a and 5.7b, we can infer the latency from the EXPs. The reason is that an EXP is defined to happen when a broadcast packet is forced to back off due to a larger backoff value that the TX vehicle is allocated. Since the IBI is set to 100 msec for the results that are given in Figs. 5.7a and 5.7b, counting the number of EXPs leads to an inferrence on the latency that this DSRC network experiences.

However, a latency longer than 100 msec might not occur in reality. In the case of DSRC, we often see the "latency" specified as 100 msec. This comes not from the basic technology, but from a convention that V2V safety messages are sent at 100 msec intervals by default. However, if one is interested in the latency between the start of a certain event and the time when a neighboring vehicle can hear about it, this latency could be much less than 100 msec. The main components would be sensor latency in the sending car, message composition time in the sending car, channel access latency in the sending car, and processing latency in the receiving car. Of these, the channel access latency is the only one over which the cars have no control. It is dictated by the 802.11 CSMA/CA MAC protocol. Operating on a 10 MHz channel with "normal" EDCA parameters (i.e. AIFSN in the range of 2 to 4 and $\mathrm{CW}_{\max}$ = 15), and if the channel is heavily loaded, and assuming the average channel busy time is about 0.5 msec (the time it takes to send 3000 bits at 6 Mbps), the sender might have to wait up to 16 busy times, or about 8 msec, to access the channel. The other contributors to event-to-communication latency could be significant, but when considering the DSRC latency it is best to focus on what DSRC requires. This is on the order of 8 to 10 msec. This is more or less worst case (hidden terminals can stretch the busy periods out to make it longer). Most often it will be much less than 10 msec, either because the sender chooses a backoff value less than 15, or because the channel is lightly loaded, or because the event-indicating message is given a lower AIFSN to reduce channel access latency.

Computation of RGB

Fig. 5.8 illustrates the mean **RGB** that is given in (5.9), according to traffic density and IBI, compared between presence and absence of interfering Wi-Fi TX.

There are two noteworthy interpretations. First, the **RGB** increases as IBI increases. This implies that traffic congestion is a predominating factor that determines the performance of a DSRC network. When each vehicle increases IBI, the total amount of packets over the air decreases. This invokes another category of research interest such as edge filtering and data aggregation for vehicular networks. Second, under interference from Wi-Fi, the **RGB** is decreased for all traffic density cases.

Fig. 5.9 also illustrates the mean **RGB** provided in (5.9), according to traffic density and CW, also compared between presence and absence of Wi-Fi interference.

Note the following two implications. First, a smaller value of CW is recommended as traffic density increases. It is obsserved with higher vehicle densities–210 and 270 vehicles in $\mathbf{R}^2_{sys}$. Comparison of boxes (a) and (b) in Figs. 5.9a and 5.9b highlights the tendency. The reason is that the **RGB** is most dependent on P_{dlvy}, since the **RGB** value for a DLVY is the largest (to recall, $\mathbf{RGB}_{dlvy} = 1 > \mathbf{RGB}_{sync}, \mathbf{RGB}_{hn}, \mathbf{RGB}_{exp}$). Because P_{dlvy} depends on both expired and collided messages, a balance needs to be found between the two quantities. After a certain point, the number of expired packets begins to prevail and the reception rate starts a slower, but steady, decrease. When P_{exp} goes beyond its peak (and the number of collisions starts increasing again), P_{dlvy} goes through another phase, where its value remains almost constant. Finally, when P_{exp} becomes low enough, the effect of collisions becomes predominant again and the number of total receptions starts decreasing once more. Second, Wi-Fi interference can be interpreted as additional traffic. This can be seen from the fact that the peak moved to the left between Figs. 5.9a and 5.9b.

An intuitive interpretation of **RGB** is here. The new metric can be translated as a more accurate version of packet delivery rate, capturing the areas that the typical metric could not evaluate. It still carries out similar meaning to a packet delivery rate since still DLVY = 1 and EXP = 0 affect significantly, depending on the instantaneous geometry that is formed by the vehicle positions. The superiority of **RGB** is that this metric provides a "wider" perspective in evaluation of the performance of a broadcast network, by taking into account an entire transmission range of a TX vehicle. A typical performance metric such as packet delivery rate must be used by specifying a tagged pair of transmitter vehicle and receiver vehicle only, which has a certain limit to represent an entire broadcast-based DSRC network. In this way, **RGB** provides a wider perspective in evaluation of the broadcast performance of a DSRC network.

5.7 Chapter Summary

This chapter proposes a new metric that accurately measures the performance of a DSRC-based vehicular network that broadcasts BSMs for safety-critical applications. Compared to traditional metrics, it more finely evaluates reception of a broadcast packet that is collided, by taking into account the RX vehicles that still are able to receive the packet. Based on the metric, it analyzes impacts of the external interference from IEEE 802.11ac-based Wi-Fi. The results suggest on the coexistence that (i) higher IBI and (ii) smaller CW are recommended in cases of higher vehicle density.

Chapter 6

Conclusions

In this dissertation, we have considered coexistence schemes of multiple wireless systems at a spectrum band to fundamentally save bandwidth and increase efficiency of wireless network operation. To this end, three different coexistence scenarios at 3.5, 5.9, and 28 and 70 GHz were studied. The main goal of the work was to examine the feasibility of coexistence of multiple wireless systems in a way that all the systems can achieve operable performances and determine viable solutions for handling inter-system interference if it deteriorates the other system's performance to an unacceptable extent. Therefore, this work aims at suggestion of a viable solution for the exponential increase wireless data traffic envisioned for the next generation 5G wireless networks.

As aforementioned, to address the general usefulness of spectrum sharing, this dissertation concentrated on three major thrust areas namely–(i) coexistence of 5G and FSS at 28 GHz and FS at 70 GHz; (ii) coexistence of communications and pulsed radar at 3.5 GHz; (iii) coexistence of DSRC and Wi-Fi at 5.9 GHz. In each thrust area, we ventured to take a specific approach which aids us in providing a more holistic answer to the question on the advantages of spectrum sharing. Therefore, conclusions from the thrust areas are different from each other, and are posed as below.

1. ***5G-FSS and FS Coexistence at 28 and 70 GHz*:** This study, presented in Chapter 2, presented a detailed analysis of coexistence scenarios for 5G in mmW bands, namely coexistence of 5G with FSS uplink at 28 GHz and with FS WB at 70 GHz. The first part of our 28 GHz study discussed the AP-to-SS interference. We showed that 5G can satisfy interference protection criteria of the FSS while allowing simultaneous transmissions from at least several thousands of sectors under various LoS and NLoS channel conditions and with various sets of parameters for the FSS. In the analysis of ES-to-AP interference, we characterized the separation distances in order to guarantee that higher than 95% of uplink transmissions in the nearest cell are protected. The required separation distances are not overly restrictive for deployment of 5G systems,

and our results further validate that the 28 GHz band is viable for future 5G system deployments. In the 70 GHz study, we demonstrated that the 5G-to-FS interference is more significant than the FS-to-5G interference, due to aggregation of interference among all of the sectors. Motivated by this observation, we proposed the mechanisms that mitigate the interference from APs and UEs into the FS system. Our results showed that the proposed techniques can effectively suppress the interference at the FS receiver while maintaining operable performance of the 5G system.

2. ***Communications-Radar Coexistence at 3.5 GHz*:** This work was divided into two main parts and discussed in Chapters 3 and 4. While Chapter 3 exhibited a geometric analysis to characterize coexistence of outdoor Wi-Fi and pulsed radar, Chapter 4 suggested a signal processing technique that makes wireless communications adopting OFDM robust against pulsed interference from radar. In both parts of study, methods for suppressing inter-system interference were proposed and examined the effectiveness.

   The main contribution of Chapter 3 was proposition of a technique that mitigates WtR interference while maintaining Wi-Fi system operation. It suggested a novel method that addresses the interference from the outdoor Wi-Fi to the radar at 3.5 GHz. While most of prior work is only interested in reduction of such interference by restricting Wi-Fi's operation, we proposed a technique that mitigates such interference while maintaining the performance of Wi-Fi. We provided a framework for analyzing the coexistence between the two systems based on the stochastic geometry. In addition, we presented an accurate characterization of the Wi-Fi systems' behavior, by taking into account the two popular types of multiple access schemes: normal CSMA and EDCA.

   Chapter 4 proposed PSUN, an OFDM transmission scheme enabling an LTE system to coexist with federal military radars in the 3.5 GHz Band. The scheme is comprised of PB at an RX and precoding of null subcarriers at a TX of an OFDM system. To maximize data rate, an OFDM TX employing PSUN (i) localizes OFDM symbols to be radar-interfered a priori, and (ii) shifts redundancy from channel coding to subcarriers in the OFDM symbols. This chapter considerd existence of sensing functionality in the 3.5 GHz Band coexistence architecture, and hence impacts of imperfect sensing which can occur due to a sensing error by an ESC and parameter changes by a radar. Results showed that PSUN is still effective in suppressing ICI remaining after PB even with imperfect pulse prediction, and as a result enables an LTE system to support various use cases of 5G that require the data rate lower than 50 Mbps in the downlink and relatively larger file size such as video streaming.

3. ***DSRC-Wi-Fi Coexistence at 5.9 GHz*:** Chapter 5 proposed a new metric that more accurately evaluates the performance of a DSRC-based vehicular network that broadcasts BSMs for safety-critical applications, by capturing packet reception by a subset of transmission range of a TX vehicle. Based on the metric, it assessed impacts of the external interference from IEEE 802.11ac-based Wi-Fi. The results suggested

that (i) higher IBI and (ii) smaller CW were recommended in cases of higher vehicle density.

Through the course of this dissertation, we contributed by providing different analysis frameworks for different coexistence scenarios in three spectrum bands that have been invoking great research interest. The technical exposition highlights the richness of problems considered in this work and also points to the vast array of research avenues still remaining unexplored in the paradigm of shared usage of spectrum for various wireless systems. However, the results of this dissertation also show unequivocally that the suggested approaches can achieve coexistence in the three spectrum sharing scenarios. As a result, the proposed coexistence methods can be viable and scalable solutions to deal with the exponentially increasing capacity demands of the ever evolving wireless communications landscape.

Bibliography

[1] https://spectrumfutures.org/what-is-spectrum-sharing-and-why-does-it-matter/

[2] Federal Communications Commission, *In the Matter of Use of Spectrum Bands Above 24 GHz For Mobile Radio Services; Establishing a More Flexible Framework to Facilitate Satellite Operations in the 27.5-28.35 GHz and 37.5-40 GHz Bands; Petition for Rulemaking of the Fixed Wireless Communications Coalition to Create Service Rules for the 42-43.5 GHz Band; Amendment of Parts 1, 22, 24, 27, 74, 80, 90, 95, and 101 To Establish Uniform License Renewal, Discontinuance of Operation, and Geographic Partitioning and Spectrum Disaggregation Rules and Policies for Certain Wireless Radio Services; Allocation and Designation of Spectrum for Fixed-Satellite Services in the 37.5-38.5 GHz, 40.5-41.5 GHz and 48.2-50.2 GHz Frequency Bands; Allocation of Spectrum to Upgrade Fixed and Mobile Allocations in the 40.5-42.5 GHz Frequency Band; Allocation of Spectrum in the 46.9-47.0 GHz Frequency Band for Wireless Services; and Allocation of Spectrum in the 37.0-38.0 GHz and 40.0-40.5 GHz for Government Operations*, FCC 16-89A1.

[3] G. Locke and L. Strickling, "Plan and timetable to make available 500 megahertz of spectrum for wireless broadband, U.S. Department of Commerce, Washington, D.C., USA, Oct. 2010.

[4] A. Ghosh, T. Thomas, M. Cudak, R. Ratasuk, P. Moorut, F. Vook, T. Rappaport, G. MacCartney, Jr., S. Sun, and S. Nie, "Millimeter-wave enhanced local area systems: a high-data-rate approach for future wireless networks," *IEEE J. Sel. Areas Commun.*, vol. 32, no. 6, Jun. 2014.

[5] J. Reed and N. Tripathi, ",The 600 MHz spectrum auction: an analysis of the band plan framework and response to certain proposals," Available at: https://ecfsapi.fcc.gov/file/7022130223.pdf.

[6] Federal Communications Commission, *Expanding the Economic and Innovation Opportunities of Spectrum Through Incentive Auctions*, FCC 12-357.

[7] NTIA, "An Assessment of the Near-Term Viability of Accommodating Wireless Broadband Systems in the 1675-1710 MHz, 1755-1780 MHz, 3500-3650 MHz, 4200-4220 MHz and 4380-4400 MHz Bands," 2010.

[8] U.S. Government Accountability Office (GAO), *Intelligent Transportation Systems: Vehicle-to-Vehicle Technologies Expected to Offer Safety Benefits, but A Variety of Deployment Challenges Exist*, Technical Report, Nov. 2013.

[9] Federal Communications Commission, *In the Matter of Amendment of the Commissions Rules Regarding Dedicated Short-Range Communications Services in the 5.850-5.925 GHz Band (5.9 GHz Band)*, FCC 03-324.

[10] Qualcomm, *NPRM13-22, Comments of Qualcomm Incorporated*, May 2013.

[11] Z. Pi and F. Khan, "An introduction to millimeter-wave mobile broadband systems," *IEEE Commun. Mag.*, Jun. 2011.

[12] C. T. Neil *et al.*, "On the impact of antenna topologies for massive MIMO systems," in *Proc. IEEE ICC*, 2015.

[13] C. T. Neil *et al.*, "Deployment issues for massive MIMO systems," in *Proc. IEEE ICC*, 2015.

[14] *Report and Order and Second Further Notice of Proposed Rulemaking*, FCC GN Docket No. 12-354, Washington, DC, USA, Apr. 2015.

[15] *Report and Order and Second Further Notice of Proposed Rulemaking*, FCC GN Docket No. 14-177, Washington, DC, USA, Jul. 2016.

[16] *World Radiocommunication Conference 2015 (WRC-15)*, ITU, Geneva Switzerland, Nov. 2015.

[17] 3GPP, *Further advancements for E-UTRA physical layer aspects*, Sophia-Antipolis, France, TR 36.814 (Release 9), 2010.

[18] M. Akdeniz *et al.*, "Millimeter wave channel modeling and cellular capacity evaluation," *IEEE J. Sel. Areas Commun.*, vol. 32, no. 6, 2014.

[19] A. Khawar *et al.*, "A mathematical analysis of cellular interference on the performance of S-band military radar systems," in *Proc. IEEE Wireless Telecommun. Symp. (WTS)*, 2014.

[20] Y. Noam and A. J. Goldsmith, "Blind null-space learning for MIMO underlay cognitive radio with primary user interference adaptation," *IEEE Trans. Wireless Commun.*, vol. 12, no. 4, Apr. 2013.

[21] K. Sung *et al.*, "Aggregate interference in secondary access with interference protection," *IEEE Commun. Lett.*, vol. 15, no. 6, Jun. 2011.

[22] P. A. Dmochowski *et al.*, "Interference models for heterogeneous sources," in *Proc. IEEE ICC*, 2012.

[23] M. Ghorbanzadeh *et al.*, "Radar inband and out-of-band interference into LTE macro and small cell uplinks in the 3.5 GHz band," in *Proc. IEEE WCNC*, 2015.

[24] J. H. Reed *et al.*, "On the co-existence of TD-LTE and radar over 3.5 GHz band: an experimental study," *IEEE Wireless Commun. Lett.*, vol. 5, no. 4, Aug. 2016.

[25] M. Tercero *et al.*, "Impact of aggregate interference on meteorological radar from secondary users," in *Proc. IEEE WCNC*, 2011.

[26] F. Hessar and S. Roy, "Spectrum sharing between a surveillance radar and secondary Wi-Fi networks," *IEEE Trans. Aerosp. Electron. Syst.*, vol. 52, iss. 3, 2016.

[27] Y. Niu, Y. Li, D. Jin, L. Su, and A. Vasilakos, "A survey of millimeter wave communications (mmWave) for 5G: opportunities and challenges," *Springer Wireless Netw.*, vol. 21, Apr. 2015.

[28] S. Rangan *et al.*, "Millimeter-wave cellular wireless networks: potentials and challenges," in *Proc. IEEE*, vol. 102, iss. 3, Feb. 2014.

[29] K. Zheng *et al.*, "10 Gbs hetsnets with millimeter-wave communications: access and networking - challenges and protocols," *IEEE Commun. Mag.*, vol. 53, iss. 1, Jan. 2015.

[30] H. Zhao *et al.*, "28 GHz millimeter wave cellular communication measurements for reflection and penetration loss in and around buildings in New York city," in *Proc. IEEE ICC*, 2013.

[31] A. Damnjanovic *et al.*, "A survey on 3GPP heterogeneous networks," *IEEE Wireless Commun.*, vol. 18, iss. 3, Jun. 2011.

[32] Qualcomm, LTE Advanced: Heterogeneous networks, White Paper, Jan. 2011. [Online]. http://www.qualcomm.com/media/documents.

[33] J. Andrews *et al.*, " Femtocells: past, present, and future,", *IEEE J. Sel. Areas Commun.*, vol. 30, iss. 3, Mar. 2012.

[34] V. Chandrasekhar *et al.*, "Femtocell networks: a survey," *IEEE Commun. Mag.*, vol. 46, iss. 9, Sep. 2008.

[35] H. Mehrpouyan *et al.*, "Hybrid millimeter-wave systems: a novel paradigm for HetNets," *IEEE Commun. Mag.*, vol. 53, iss. 1, Jan. 2015.

[36] K. Lee *et al.*, "Mobile data offloading: how much can WiFi deliver?," *IEEE/ACM Trans. Netw.*, vol. 21, iss. 2, Apr. 2013.

[37] J. Qiao *et al.*, "Enabling device-to-device communications in millimeter-wave 5G cellular networks," *IEEE Commun. Mag.*, vol. 53, iss. 1, Jan. 2015.

[38] Z. Pi and F. Khan, "An introduction to millimeter-wave mobile broadband systems," *IEEE Commun. Mag.*, vol. 49, iss. 6, Jun. 2011.

[39] R. Hu and Y. Qian, *Heterogeneous cellular networks*, London, Wiley, 2013.

[40] M. Bansal *et al.*, "Open-radio: a programmable wireless dataplane," in *Proc. ACM HotSDN*, 2012.

[41] E. Obregon *et al.*, "On the sharing opportunities for ultra-dense networks in the radar bands," in *Proc. IEEE DYSPAN*, 2014.

[42] M. Tercero *et al.*, "Exploiting temporal secondary access opportunities in radar spectrum," *Springer Wireless Personal Commun.*, Mar. 2013.

[43] S. Kim *et al.*, "PSUN: an OFDM-pulsed radar coexistence technique with application to 3.5GHz LTE," *Hindawi Mobile Information Systems*, 2016.

[44] S. Raymond *et al.*, "Coexistence of power-controlled cellular networks with rotating radar," *IEEE J. Sel. Areas Commun.*, vol. PP., iss. 99, 2016.

[45] F. Guidolin and M. Nekovee, "Investigating spectrum sharing between 5G millimeter wave networks and fixed satellite systems," in *Proc. IEEE Globecom*, 2015.

[46] G. R. MacCartney Jr. and T. S. Rappaport, "73 GHz millimeter wave propagation measurements for outdoor urban mobile and backhaul communications in New York City," in *Proc. IEEE ICC*, 2014.

[47] O. Holland and M. Dohler, "Geolocation-based architecture for heterogeneous spectrum usage in 5G," in *Proc. IEEE Globecom*, 2015.

[48] D. A. Wassie *et al.*, "Experimental verification of interference mitigation techniques for 5G small cells," in *Proc. IEEE VTC Spring*, 2015.

[49] T. K. Vu *et al.*, "Joint in-band backhauling and interference mitigation in 5G heterogeneous networks," in *Proc. IEEE European Wireless*, 2016.

[50] G. Li *et al.*, "Coordination context-based spectrum sharing for 5G millimeter-wave networks," in *Proc. IEEE CROWNCOM*, 2014.

[51] D. Stoyan *et al.*, *Stochastic geometry and its applications*, volume 2. Wiley Chichester, 1995.

[52] *Calculation of free-space attenuation*, ITU-R P.525.

[53] H. Anderson, *Fixed broadband wireless system design*, John Wiley & Sons, 2003.

[54] Letter from Verizon, AT&T, Nokia, Ericsson, Samsung and T-Mobile to Federal Communications Commission, "Use of Spectrum Bands Above 24 GHz For Mobile Radio Services, GN Docket No. 14-177, Establishing a More Flexible Framework to Facilitate Satellite Operations in the 27.5-28.35 GHz and 37.5-40 GHz Bands, IB Docket No. 15-256," May 2016.

[55] International Telecommunications Union, *ITU-R S.1432*, Apr. 2016.

[56] International Telecommunications Union, *ITU-R M.2030*, 2003.

[57] Available: http://www.vcomm-eng.com/wp-content/uploads/2014/01/12-35704-18-2013Verizon7022285928.pdf

[58] *Antenna performance standards*, FCC 47 CFR 25.209.

[59] P. Sahoo, "Probability and mathematical statistics," *University of Louisville*, Louisville, KY, USA, 2013.

[60] J. Riihijarvi and Petri Mahonen, "A model based approach for estimating aggregate interference in wireless networks," in *Proc. IEEE Crowncom*, 2012.

[61] A. Rabbachin *et al.*, "Cognitive network interference," *IEEE J. Sel. Areas Commun.*, vol. 29, iss. 2, Feb. 2011.

[62] *Channel model for frequency spectrum above 6 GHz (Release 14)*, 3GPP TR 38.900, v1.0.0, Jun. 2016.

[63] *Reference radiation patterns for fixed wireless system antennas for use in coordination studies and interference assessment in the frequency range from 100 MHz to about 70 GHz*, ITU-R F.699-7.

[64] International Telecommunications Union, *ITU-R F.758-6*, Sep. 2015.

[65] Nokia Solutions and Networks, "Deployment strategies for heterogeneous networks," *Nokia White Paper*, 2015.

[66] D. Daley and D. Vere-Jones, *An introduction to the theory of point processes: Volume I: Elementary Theory and Methods*, Springer Probability and its Applications, Second edition, 2003.

[67] E. Drocella *et al.*, "Description of a model to compute the aggregate interference from radio local area networks employing dynamic frequency selection to radars operating in the 5 GHz frequency range," *NTIA 09-461*, May 2009.

[68] W. Stutzman and G. Thiele. *Antenna theory and design*. John Wiley & Sons, 2012.

[69] *Evolved universal terrestrial radio access (E-UTRA); further advancements for E-UTRA physical layer aspects (Release 9)*, 3GPP TR 36.814.

[70] J. Wang *et al.*, "WOLoc: WiFi-only outdoor localization using crowdsensed hotspot labels," in *Proc. IEEE Infocom*, 2017.

[71] S. Kim, J. Choi, and C. Dietrich, "Coexistence between OFDM and pulsed radars in the 3.5 GHz band with imperfect sensing," in *Proc. IEEE WCNC*, 2016.

[72] Memorandum for the Heads of Executive Departments and Agencies, "Unleashing the wireless broadband revolution," Jul. 2010.

[73] FCC 12-148, "Amendment of the Commision's rules with regard to commercial operations in the 3550-3650 MHz band," Notice of Proposed Rulemaking in GN Docket 12-354, Dec. 2012.

[74] FCC 14-49, "Amendment of the Commision's rules with regard to commercial operations in the 3550-3650 MHz band," Further Notice of Proposed Rulemaking in GN Docket 12-354, Apr. 2015.

[75] FCC 15-47, "Amendment of the Commission's rules with regard to commercial operations in the 3550-3650 MHz band," Report and Order and Second Further Notice of Proposed Rulemaking in GN Docket No. 12-354, Apr. 2015.

[76] NTIA, *Response to commercial operations in the 3550-3650 MHz band (GN Docket No. 12-354)*, Mar. 2015.

[77] S. Sodagari, A. Khawar, T. C. Clancy, and R. McGwier, "A projection based approach for radar and telecommunication systems coexistence," *Proc. IEEE Globecom*, 2012.

[78] A. Khawar, A. Abdel-Hadi, and T. C. Clancy, "Spectrum sharing between S-band radar and LTE cellular system: a spatial approach," to appear in *Proc. IEEE DySPAN*, 2014.

[79] R. Saruthirathanaworakun, J. Peha, and L. Correia, "Opportunistic sharing between rotating radar and cellular," *IEEE J. Sel. Areas Commun.*, Vol. 30, No. 10, Nov. 2012.

[80] R. Saruthirathanaworakun, J. Peha, and L. Correia, "Gray-space spectrum sharing between multiple rotating radars and cellular network hotspots," *Proc. IEEE VTC*, 2013.

[81] F. Paisana, J. Miranda, N. Marchetti, and L. DaSilva, "Database-aided sensing for radar bands," *Proc. IEEE DySPAN*, 2014.

[82] M. Ghorbanzadeh, E. Visotsky, P. Moorut, W. Yang, and C. Clancy, "Radar in-band interference effects on macrocell LTE uplink deployments in the U.S. 3.5 GHz band," in *Proc. IEEE ICNC* 2015.

[83] H. Safavi-Naeini, C. Ghosh, E. Visotsky, R. Ratasuk, and S. Roy, "Impact and mitigation of narrow-band radar interference in down-link LTE," in *Proc. IEEE ICC* 2015.

[84] *Operations and signal security*, Army Regulation 530-1, Sep. 2005.

[85] U. Epple and M. Schnell, "Adaptive threshold optimization for a blanking nonlinearity in OFDM receivers," in *Proc. IEEE Globecom*, 2012.

[86] S. Zhidkov, "Analysis and comparison of several simple impulsive noise mitigation schemes for OFDM receivers," *IEEE Trans. Commun.*, vol. 56, Jan. 2008.

[87] M. Ghosh, "Analysis of the effect of impulse noise on multicarrier and single carrier QAM systems," *IEEE Trans. Commun.*, vol. 44, no. 2, Feb. 1996.

[88] P. Lewis, "A tutorial on impulsive noise in COFDM systems," *Digital Television Group (DTG) Monograph*, Twickenham, London, UK, no. 5, 2001. [Online]. Available: http://www.dtg.org.uk

[89] O. P. Haffenden *et al.*, "Detection and removal of clipping in multicarrier receivers," Eur. Patent Application EP1043874, Bulletin 2000/41, Oct. 2000.

[90] N. P. Cowley *et al.*, "COFDM tuner with impulse noise reduction," Eur. Patent Application EP1180851, Bulletin 2002/08, Feb. 2002.

[91] S. S. Rappaport and L. Kurz, "An optimal nonlinear detector for digital data transmission through non-Gaussian channels," *IEEE Trans. Commun. Technol.*, vol. COM-14, Jun. 1966.

[92] O. Antonov, "Optimal detection of signals in non-Gaussian noise," *Radio Eng. Electron. Phys. (USSR)*, vol. 12, pp. 541-548, 1967.

[93] K. S. Vastola, "Threshold detection in narrow-band non-Gaussian noise," *IEEE Trans. Commun.*, vol. COM-32, no. 2, Feb. 1984.

[94] R. Ingram, "Performance of the locally optimum threshold receiver and several suboptimal nonlinear receivers for ELF noise," *IEEE J. Ocean. Eng.*, vol. OE-9, no. 3, Jul. 1984.

[95] M. Cotton and R. Dalke, "Spectrum occupancy measurements of the 3550-3650 megahertz maritime radar band near San Diego, California," NTIA Report TR-14-500, Jan. 2014.

[96] S. Brandes, "Suppression of mutual interference in OFDM based overlay systems," Universitat Fridericiana Karlsruhe, May 2009.

[97] R. Fantacci *et al.*, "Multiuser interference cancellation receivers for OFDMA uplink communications with carrier frequency offset" in *Proc. IEEE Globecom*, 2004.

[98] S. Brandes, U. Epple, and M. Schnell, "Compensation of the impact of interference mitigation by pulse blanking in OFDM systems," *Proc. IEEE Globecom*, 2010.

[99] U. Epple, D. Shutin, and M. Schnell, "Mitigation of impulsive frequency-selective interference in OFDM based systems," *IEEE Wireless Commun. Lett.*, Vol. 1, No. 5, October 2012.

[100] A. Goldsmith, *Wireless communications*, Cambridge University, 2005.

[101] Y. Zhao and S. Haggman, "Sensitivity to Doppler shift and carrier frequency errors in OFDM systems-the consequences and solutions," *Proc. IEEE VTC*, 1996.

[102] Y. Zhao and S. Haggman, "Intercarrier interference self-cancellation scheme for OFDM mobile communication systems," *IEEE Trans. Commun.*, vol. 49, no. 7, Jul. 2001.

[103] J. van de Beek *et al.*, "ML estimation of time and frequency offset in OFDM systems," *IEEE Trans. Signal Process.*, vol. 45, no. 7, Jul. 1997.

[104] U. Tureli *et al.*, "Experimental and analytical studies on a high-resolution OFDM carrier frequency offset estimator," *IEEE Trans. Veh. Technol.*, vol. 50, no. 2, Mar. 2001.

[105] M. Garcia *et al.*, "Frequency offset correction for coherent OFDM in wireless systems," *IEEE Trans. Consum. Electron.*, vol. 47, no. 1, Feb. 2001.

[106] M. Luise *et al.*, "Low-complexity blind carrier frequency recovery for OFDM signals over frequency-selective radio channels," *IEEE Trans. Commun.*, vol. 50, no. 7, Jul. 2002.

[107] J. Armstrong, "Analysis of new and existing methods of reducing intercarrier interference due to carrier frequency offset in OFDM," *IEEE Trans. Commun.*, vol. 47, no. 3, Mar. 1999.

[108] M. Gudmundson and P. O. Anderson, "Adjacent channel interference in an OFDM system," in *Proc. IEEE VTC*, 1996.

[109] C. Muschallik, "Improving an OFDM reception using an adaptive Nyquist windowing," *IEEE Trans. Consum. Electron.*, vol. 42, no. 3, Aug. 1996.

[110] Y. Zhao and S. Haggman, "Intercarrier interference compression in OFDM communication systems by using correlative coding," *IEEE Commun. Lett.*, vol. 2, no. 8, Aug. 1998.

[111] K. Sathananthan and C. Tellambura, "Forward error correction codes to reduce intercarrier interference in OFDM," in *Proc. IEEE ISSC*, 2001.

[112] Y. Fu and C. Ko, "A new ICI self-cancellation scheme for OFDM systems based on a generalized signal mapper," *Proc. IEEE Internat. Sympos. Pers., Indoor, Mobile Radio Commun.*, 2002.

[113] Y. Peng, Y. Kuo, G. Lee, and J. Wen, "Performance analysis of a new ICI-self-cancellation-scheme in OFDM systems," *IEEE Trans. Consumer Electron.*, Vol. 53, No. 4, 2007.

[114] Q. Shi, Y. Fang, and M. Wang, "A novel ICI self-cancellation scheme for OFDM systems," *Proc. IEEE Wicom*, 2009.

[115] H. V. Poor, *An Introduction to Signal Detection and Estimation*, 2nd ed. New York: Springer-Verlag, 1994.

[116] J. Chong, D. Sung, and Y. Sung, "Cross-Layer Performance Analysis for CSMA/CA Protocols: Impact of Imperfect Sensing," *IEEE Trans. Veh. Tech.*, Vol. 59, No. 3, Mar. 2010.

[117] F. Paisana, N. Marchetti, and L. DaSilva, "Radar, TV and Cellular Bands: Which Spectrum Access Techniques for Which Bands?," *IEEE Commun. Surveys & Tutorials*, Vol. 16, No. 3, Third Quarter 2014.

[118] S. Ahmed and M. Kawai, "Dynamic null-data subcarrier switching for OFDM PAPR reduction with low computational overhead," *IEEE Electron. Lett.*, Vol. 48, No. 9, 2012.

[119] M. Ghogho, A. Swami, and G. Giannakis, "Optimized null-subcarrier selection for CFO estimation in OFDM over frequency-selective fading channels," *Proc. IEEE Globecom*, 2001.

[120] B. Wang, P. Ho, and C. Lin, "OFDM PAPR reduction by shifting null subcarriers among data subcarriers," *IEEE Commun. Lett.*, Vol. 16, No. 9, 2012.

[121] 3GPP TR 36.814 V9.0.0 (2010-03), *Further advancements for EUTRA physical layer aspects*, Release 9, 2010.

[122] The Next Generation Mobile Networks Ltd., *NGMN 5G White Paper*, Feb. 2015.

[123] Cisco, *Cisco visual networking index: global mobile data traffic forecast update, 2015-2020 white paper*, Feb. 2016.

[124] Y. Morgan, "Managing DSRC and WAVE standards operations in a V2V scenario," *Hindawi Journal of Vehicular Technology*, 2010.

[125] IEEE 802.11p SWG, *et al.*, "Draft Amendment to Standard for Information Technology–Telecommunications and information exchange between systemsLocal and Metropolitan networksspecific requirements–part 11: Wireless LAN Medium Access Control (MAC) and Physical Layer (PHY) specifications: Ammendment: Wireless Access in Vehicular Environments," *IEEE 802.11p D6.0*, Jun. 2009.

[126] J. Mar, *et al.*, "A pilot sub-carrier-aided frequency equalizer for the dedicated short-range communications system over time-varying fading channels, in *Proc. The Management and Technology Forum, China Communications*, pp. 33-41, Dec. 2006.

[127] J. Liu and J. Li, "Packet design and signal processing for OFDM-based mobile broadband wireless communication systems," *IEEE Trans. Mobile Computing*, vol. 5, no. 9, 2006.

[128] The Department of Transportation, *DSRC-Unlicensed Device Test plan*, Aug. 2015.

[129] Federal Communications Commission, *The commission seeks to update and refresh the record in the "unlicensed national information infrastructure (U-NII) devices in the 5 GHz band" Proceeding*, FCC 16-68A1.

[130] J. Lansford *et al.*, "Coexistence of unlicensed devices with DSRC systems in the 5.9 GHz band," in *Proc. IEEE VNC 2013.*

[131] K.-H. Chang, "Wireless communications for vehicular safety," *IEEE Wireless Commun.*, vol. 22, no. 1, 2015.

[132] National Telecommunications and Information Administration (NTIA), *Evaluation of the 5350-5470 MHz and 5850-5925 MHz bands*, Jan. 2013.

[133] Y. Park and H. Kim, "On the coexistence of IEEE 802.11ac and WAVE in the 5.9 GHz band," *IEEE Commun. Mag.*, vol. 52, no. 6, 2014.

[134] G. Naik *et al.*, "Coexistence of dedicated short range communication (DSRC) and Wi-Fi: implications to Wi-Fi performance," in *Proc. IEEE Infocom*, 2017.

[135] M. Farooq *et al.*, "A stochastic geometry model for multi-hop highway vehicular communication," *IEEE Trans. Wireless Commun.*, vol. 15, no. 3, Mar. 2016.

[136] X. Ma and X. Chen, "Delay and broadcast reception rates of highway safety applications in vehicular ad hoc networks," in *Proc. IEEE Mobile Networking for Vehicular Environments*, 2007.

[137] X. Ma *et al.*, "Performance and reliability of DSRC vehicular safety communication: a formal analysis," *EURASIP Journal on Wireless Communications and Networking*, 2009.

[138] X. Ma *et al.*, "Reliability analysis of one-hop safety critical broadcast services in VANETs," *IEEE Trans. Veh. Technol.*, vol. 60, no. 8, 2011.

[139] X. Yin *et al.*, "Performance and reliability evaluation of BSM broadcasting in DSRC with multi-channel schemes," *IEEE Trans. Computers*, vol. 63, no. 12, 2014.

[140] C. Campolo *et al.*, "Modeling broadcasting in IEEE 802.11p/WAVE vehicular networks," *IEEE Commun. Lett.*, vol. 15, no. 2, 2011.

[141] Z. Tong *et al.*, "A stochastic geometry approach to the modeling of DSRC for vehicular safety communication," *IEEE Trans. Intell. Transp. Syst.*, vol. 17, no. 5, May 2016.

[142] T. ElBatt *et al.*, "Cooperative collision warning using dedicated short range wireless communications," in *Proc. ACM VANET*, 2006.

[143] D. Daley and D. Vere-Jones, *An introduction to the theory of point processes: Volume I: Elementary Theory and Methods*, Springer Probability and its Applications, Second edition, 2003.

[144] R. Stanica *et al.*, "Reverse back-off mechanism for safety vehicular ad hoc networks," *Elsevier Ad Hoc Networks*, vol. 16, 2014.

[145] http://www.arachnoid.com/lutusp/auto.html